UNIVERSITY OF GHANA

CHARACTERIZATION OF GHANA RESEARCH REACTOR-1 LOW ENRICHED URANIUM CORE IRRADIATION SITES USING A THEORETICAL METHOD

BY

BERNARD OSEI: 10312805
BSc (Legon), 2013

THIS THESIS IS SUBMITTED TO THE GRADUATE
SCHOOL OF NUCLEAR AND ALLIED SCIENCES UNIVERSITY
OF GHANA, LEGON IN PARTIAL FULFILLMENT OF THE
REQUIREMENT FOR THE AWARD OF MPHIL
APPLIED NUCLEAR PHYSICS DEGREE

July, 2017

DECLARATION

I hereby declare that, with exception of references to other peoples work which have duly been acknowledged, this work is the result of my own original research undertaken under supervision, and either in whole or in part has not been presented for any other degree at another university elsewhere.

....

Bernard Osei Date
(Student)

Supervisors declaration:

We hereby declare that the preparation and presentation of the thesis were supervised in accordance with guidelines on supervision of thesis laid down by the University of Ghana.

....

Prof. B. J. B. Nyarko Dr. H. C. Odoi
(Principal Supervisor) (Co-supervisor)

Date:... Date:...

ABSTRACT

The GHARR-1 is in the final stages of converting its HEU (90.2 %) fuel to LEU (13 %) fuel. Due to the differences if the LEU core design as compared to that of the HEU; fuel density, dummy arrnagement, number of fuel elements, this study was carried out characterize the neutron spectrum at the irradiation sites of GHARR-1 to ascertain the impact of the conversion on the neutron spectrum. This was done theoretically using the MCNP5 code. The neutron spectrum parameters (α and f), neutron fluxes and their axial variation were determined. Average results of α for the LEU (inner sites, -0.096; outer sites, -0.031) as compared to the HEU (inner sites, -0.103; outer sites, -0.034) indicate a further deviation from the ideal 1/E epithermal spectrum distribution for the HEU as compared to the LEU. Results of f for the HEU (inner sites, 18.76; outer sites, 48.75) and LEU (inner sites, 17.77; outer sites, 45.08) indicate some levels of neutron flux trade off in the LEU as compared to the HEU. This is attributed to the increased inventory of ^{238}U in the LEU as compared to the HEU. The neutron flux distribution showed high levels of uniformity at the irradiation sites (2 % to 10 % variation), with the thermal neutron flux showing the highest level of uniformity. The flux distribution for GHARR-1 with HEU and LEU both followed similar patterns.

DEDICATION

This work is dedicated to my parents and siblings for their infinite love and care.

ACKNOWLEDGEMENT

My sincerest gratitude goes to the Almighty God for His unending mercies and support throughout my life and in the execution of this research. I am especially indebted to my thesis supervisors, Prof. B. J. B. Nyarko and Dr. H. C. Odoi whose direction, criticisms and advice nurtured this work into fruition. I also want to express my appreciation to the Head of Department and all Lecturers of the Department of Nuclear and Applied Sciences for their support, advice and guidance throughout my stay in this University. My sincere appreciation also goes to Mr. Isaac Kwesi Baidoo, Mr. William Osei Mensah, Mr. Kwame Gyamfi, Mr. Felix Ameyaw and Mr. Robert Ekow Quagraine and all staff of GHARR - 1 centre for their individual contributions towards the completion of this work. Finally to all who contributed in diverse ways, I say a big thank you and may the Almighty God bless you.

TABLE OF CONTENTS

DECLARATION **i**

ABSTRACT **ii**

DEDICATION **iii**

ACKNOWLEDGEMENT **iv**

LIST OF TABLES **viii**

LIST OF FIGURES **ix**

ABBREVIATIONS **xiv**

SYMBOLS **xv**

CHAPTER 1

INTRODUCTION **1**

1.1 Background 1

1.2 Problem Statement 4

1.3 Objectives 4

1.4 Relevance and Justification 4

1.5 Scope 5

1.6 Overview of Study 5

CHAPTER 2

LITERATURE REVIEW **7**

2.1 Theory 7

  2.1.1 Neutron Interactions 7

  2.1.2 Neutron Energy Spectrum 8

    2.1.2.1 Fast Neutron 9

    2.1.2.2 Epithermal Neutrons 10

    2.1.2.3 Thermal Neutrons 10

  2.1.3 (n,γ) Reactions 11

    2.1.3.1 Hogdahl Convention 11

2.1.4 Neutron transport theory 15
2.1.5 Monte Carlo methods 16
2.1.6 MCNP calculations 18
2.1.6.1 Criticality calculations in MCNP 20
2.1.6.2 Nuclear reaction data libraries 21
2.1.6.3 Tally specification in MCNP 22
2.2 Description of GHARR-1 23
2.2.1 GHARR-1 HEU core 25
2.2.2 GHARR-1 LEU core 25
2.3 Monte Carlo Model of GHARR-1 26
2.4 Characterization at GHARR-1 Irradiation Sites 32
2.5 Conversion of HEU to LEU 36
CHAPTER 3
METHODOLOGY **39**
3.1 MCNP Model 39
3.2 MCNP Calculations 47
3.2.1 Neutron flux and flux distribution 47
3.2.2 Neutron spectrum parameters 50
3.2.2.1 Cd-ratio method 51
3.2.2.2 Cd-ratio for multi-monitor method 52
CHAPTER 4
RESULTS AND DISCUSSION **53**
4.1 Criticality results 53
4.2 Neutron spectrum parameters 54
4.3 Neutron flux 62
4.4 Neutron flux distributions 66

CHAPTER 5

CONCLUSIONS AND RECOMMENDATIONS **79**

5.1 Conclusion 79

5.2 Recommendations 80

APPENDICES **80**

Appendix A MCNP Tally Cards 81

A.0.1 F4 Tally Card 81

A.0.2 FM Tally Card 82

Appendix B Input deck for remodeled components 83

Appendix C Uncertainty Analysis 85

Appendix D Comparism of HEU and LEU Neutron Fluxes 88

Appendix E Neutron flux distribution 90

REFERENCES **97**

LIST OF TABLES

2.1 Comparison of GHARR-1 HEU and LEU Core 25

2.2 Comparison of specifications of core configurations 31

3.1 Neutron spectrum energy ranges 49

3.2 Neutron spectrum energy ranges 50

4.1 K_{eff} and Reactivity of GHARR-1 HEU and LEU models 53

4.2 Cadmium ratios and non-ideal resonance integral to thermal neutron cross section for flux monitors at inner irradiation sites of HEU core 55

4.3 Neutron spectrum parameters at inner irradiation sites for HEU core 56

4.4 Cadmium ratios and non-ideal resonance integral to thermal neutron cross section for flux monitors at inner irradiation sites of HEU core 57

4.5 Neutron spectrum parameters at inner irradiation sites for HEU core 58

4.6 Cadmium ratios and non-ideal resonance integral to thermal neutron cross section for flux monitors at inner irradiation sites of LEU core 59

4.7 Neutron spectrum parameters at inner irradiation sites for LEU core 59

4.8 Cadmium ratios and non-ideal resonance integral to thermal neutron cross section for flux monitors at inner irradiation sites of LEU core 60

4.9 Neutron spectrum parameters at inner irradiation sites for LEU core 60

4.10 Average neutron flux ranges for inner irradiation sites of LEU core at 17 KW and 34 KW 72

4.11 Average neutron flux ranges for outer irradiation sites of LEU core at 17 KW and 34 KW 78

5.1 Neutron flux at inner irradiation sites for LEU at 17 KW and HEU at 15 KW 88

5.2 Neutron flux at inner irradiation sites for LEU at 34 KW and HEU at 30 KW 88

5.3 Neutron flux at outer irradiation sites for LEU at 17 KW and HEU at 15 KW 89
5.4 Neutron flux at outer irradiation sites for LEU at 34 KW and HEU at 30 KW 89
5.5 Neutron flux at LEU core inner irradiation sites at 17 KW 90
5.6 Neutron flux at LEU core outer irradiation sites at 17 KW 91
5.7 Neutron flux at LEU core inner irradiation sites at 34 KW 92
5.8 Neutron flux at LEU core outer irradiation sites at 34 KW 93
5.9 Neutron flux at HEU core inner irradiation sites at 15 KW 94
5.10 Neutron flux at HEU core outer irradiation sites at 15 KW 95
5.11 Neutron flux at HEU core inner irradiation sites at 30 KW 96
5.12 Neutron flux at HEU core outer irradiation sites at 30 KW 97

LIST OF FIGURES

1.1 Fuel loading for the Zero Power Test at CIAE 3

2.1 Neutron energy spectrum 9
2.2 Cross section curve of cadmium 12
2.3 Non ideality of epithermal neutron flux distribution 14
2.4 Random history of neutrons 17
2.5 Flow chart of the MCNP code 20
2.6 Vertical cross section of GHARR-1 24
2.7 Horizontal cross section of GHARR-1 24
2.8 x-y view of the MCNP plot of MNSR model 27
2.9 Vertical cross sectional of MNSR model 27
2.10 MCNP5 plot of the core configuration of the improved MNSR model 29
2.11 MCNP5 plot of vertical cross section of the improved MNSR model(Anim-Sampong et al., n.d.) 30

3.1 MCNP model of GHARR-1 LEU fuel pin 40
3.2 Cross sectional view of inner irradiation sites 41
3.3 Cross sectional view of outer irradiation sites 41
3.4 Reactivity regulator MCNP model 42
3.5 GHARR-1 LEU core control rod 43
3.6 2D view of the GHARR-1 LEU core 44
3.7 3D view of the GHARR-1 MCNP core 45
3.8 Horizontal cross sectional view of the GHARR-1 MCNP model 46
3.9 Horizontal cross sectional view of the GHARR-1 MCNP model 46
3.10 Segmentation of rabbit capsule for neutron flux distribution 48

4.1 Thermal neutron flux at inner irradiation sites for GHARR-1 LEU and HEU cores at Half and Full Power 62
4.2 Epithermal neutron flux at inner irradiation sites for GHARR-1 LEU and HEU cores at Half and Full Power 63
4.3 Fast neutron flux at inner irradiation sites for GHARR-1 LEU and HEU cores at Half and Full Power 63
4.4 Thermal neutron flux at outer irradiation sites for GHARR-1 LEU and HEU cores at Half and Full Power 64
4.5 Epithermal neutron flux at outer irradiation sites for GHARR-1 LEU and HEU cores at Half and Full Power 65
4.6 Fast neutron flux at outer irradiation sites for GHARR-1 LEU and HEU cores at Half and Full Power 65
4.7 Comparison of LEU and HEU neutron flux distribution at Inner site 1 at Half Power 66
4.8 Comparison of LEU and HEU neutron flux distribution at Inner site 1 at Full Power 67
4.9 Comparison of LEU and HEU neutron flux distribution at Inner site 2 at Half Power 67
4.10 Comparison of LEU and HEU neutron flux distribution at Inner site 2 at Full Power 68
4.11 Comparison of LEU and HEU neutron flux distribution at Inner site 3 at Half Power 68
4.12 Comparison of LEU and HEU neutron flux distribution at Inner site 3 at Full Power 69
4.13 Comparison of LEU and HEU neutron flux distribution at Inner site 4 at Half Power 69

4.14 Comparison of LEU and HEU neutron flux distribution at Inner site 4 at Full Power 70

4.15 Comparison of LEU and HEU neutron flux distribution at Inner site 5 at Half Power 70

4.16 Comparison of LEU and HEU neutron flux distribution at Inner site 5 at Full Power 71

4.17 Comparison of LEU and HEU neutron flux distribution at Outer site 1 at Half Power 73

4.18 Comparison of LEU and HEU neutron flux distribution at Outer site 1 at Full Power 73

4.19 Comparison of LEU and HEU neutron flux distribution at Outer site 2 at Half Power 74

4.20 Comparison of LEU and HEU neutron flux distribution at Outer site 2 at Full Power 74

4.21 Comparison of LEU and HEU neutron flux distribution at Outer site 3 at Half Power 75

4.22 Comparison of LEU and HEU neutron flux distribution at Outer site 3 at Full Power 75

4.23 Comparison of LEU and HEU neutron flux distribution at Outer site 4 at Half Power 76

4.24 Comparison of LEU and HEU neutron flux distribution at Outer site 4 at Full Power 76

4.25 Comparison of LEU and HEU neutron flux distribution at Outer site 5 at Half Power 77

4.26 Comparison of LEU and HEU neutron flux distribution at Outer site 5 at Full Power 77

5.1 Neutron track lengths in a cell 82

5.2 Cell cards 83
5.3 Surface cards 84
5.4 Material cards 85

ABBREVIATIONS

ACE	A Compact ENDF
ANL	Argonne National Laboratory
CIAE	China Institute of Atomic Energy
CRP	Coordinated Research Project
CSEWG	Cross Section Working Group
DNRR	Dalat Nuclear Research Reactor
DoE	Department of Energy
ENDF/B	Evaluated Neutron Data File / B
GHARR-1	Ghana Research Reactor -1
GTRI	Global Threat Reduction Initiative
HEU	High Enriched Uranium
IAEA	International Atomic Energy Agency
LEU	Low Enriched Uranium
M^3	Material Management and Minimization
MCNP	Monte Carlo N-Particle Simulation
MNSR	Miniature Neutron Source Reactor
NAA	Neutron Activation Analysis
NEA	Nuclear Energy Agency
RERTR	Reduced Enrichment for Research and Test Reactors
RPI	Portugese Research Reactor
SAR	Safety Analysis Report
US	United States
ZIrc-4	Zircaloy-4
ZPT	Zero Power Test
2D	Two Dimensional
3D	Three Dimensional

SYMBOLS

E_{Cd}	Cadmium cut off energy	eV
I_o	Ideal resonance integral	barns
$I_o(\alpha)$	Non-ideal resonance integral	barns
k	Boltzmann constant	JK^{-1}
K_{eff}	Multiplication factor	–
$n'(v)$	Number of neutrons with velocity, v	–
n_{th}	Number of neutrons in thermal energy range	–
Q_o	Ideal resonance integral to thermal neutron cross section ratio	–
$Q_o(\alpha)$	Non-ideal resonace integral to thermal neutron cross section ratio	–
R	Reaction rate	s^{-1}
R_{Cd}	Cadmium Ratio	–
T	Temperature in Kelvin	K
UAl_4	Uranium Aluminium alloy	–
U_3Si_2	Uranium Silicide	–
U-9Mo	Uranium Molybdenum alloy	–
v	Velocity	ms^{-1}
$Z_f(E_r)$	Error in f as a result of $\bar{E}_r$	–
$Z_f(R_{Cd}, r)$	Error in f as a result of R_{Cd}	–
$Z_f(\alpha)$	Error in f as a result of α	–
$Z_{Q_o(\alpha)}$	Error in $Q_o(\alpha)$	–
$Z_{Q_o(\alpha)}(\alpha)$	Error in $Q_o(\alpha)$ as a result of α	–
$Z_\alpha(A_n)$	Error in α as a result of Activity	–
$Z_\alpha(\bar{E}_{r,n})$	Error in α as a result of $\bar{E}_r$	–
$Z_\alpha(Q_{o,n})$	Error in α as a result of Q_o	–

α	Epithermal neutron shape factor	–
σ_a	Neutron absorption cross section	barns
σ_e	Elastic neutron scattering cross section	barns
σ_i	Inelastic neutron scattering cross section	barns
σ_o	Thermal neutron cross section	barns
σ_s	Neutron scattering cross section	barns
σ_T	Total neutron cross section	barns
$\sigma(E)$	Energy dependent neutron cross section	barns
$\sigma(v)$	Velocity dependent neutron cross section	barns
ϕ_{epi}	Conventional epithermal neutron flux	$ncm^{-2}s^{-1}$
ϕ_f	Conventional fast neutron flux	$ncm^{-2}s^{-1}$
ϕ_{th}	Conventional thermal neutron flux	$ncm^{-2}s^{-1}$
$\varphi(E)$	Energy dependent neutron flux	$ncm^{-2}s^{-1}$
$\varphi(v)$	Velocity dependent neutron flux	$ncm^{-2}s^{-1}$
$\chi(E)$	Fast or Fission neutron spectrum	–

CHAPTER 1

INTRODUCTION

1.1 Background

Several national and international bodies have taken measures since 1978 to address the issue of nuclear proliferation of civil research and test reactors. The United States (US) Department of Energy (DoE) via its Reduced Enrichment for Research and Test Reactors (RERTR) programme has for almost 40 years worked to develop the technology needed to facilitate the conversion of civilian facilities using high enriched uranium (HEU) fuel to low enriched uranium (LEU) fuel (Adelfang & Atger, 2006). Preference is given to LEU fuels because it is less prone to proliferation as compared to HEU fuels. In 2004, the US secretary of Energy established the Global Threat Reduction Initiative (GTRI) to complement the RERTR. The main aim of the GTRI was to minimize the availablilty of nuclear weapon grade materials by securing, removing, relocating and disposing of relevant material and equipments (Adelfang & Atger, 2006). The International Atomic Energy Agency (IAEA) has setup several projects to support the RERTR and GTRI programmes. These projects focus on LEU fuel technology development, repatriation of fresh and irradiated HEU fuel and HEU to LEU conversion. Countries operating Miniature Neutron Source Reactors (MNSRs) known as the MNSR community in May 2005 expressed their desire to convert from HEU to LEU fuels. With regards to this consensus, an IAEA Coordinated Research Project (CRP) and subsequently an MNSR working group was establised to coordinate the activities to help convert MNSRs from HEU to LEU fuels ("CRP on conversion of Miniature Neutron Source Research Reactors (MNSR) to Low Enriched Uranium (LEU)", 2014). The US Argonne National Laboratory (ANL) took part in the CRP and offered support to the generic analysis of the conversion of MNSRs. As part of efforts to aid the conversion of MNSRs an agreement was reached between the ANL and China Institute of Atomic Energy (CIAE) in september 2010 for the establishment of a zero power test facility in Beijing, China ("Argonne, China sign agreement to develop Zero Power Test Facility", 2010). The facility is to help determine the final loading of LEU fuel cores for the various MNSR facilities. In relation to the conversion of MNSRs, the Ghana MNSR, Ghana Research Reactor-1 (GHARR-1) has gone through several satges of its core conversion programme and is near completion. This programme was championed by the United States (US) Department of Energy, through its office of Material Management and Minimization (M^3). The M^3 was set up in the year 2015 to replace the Global Threat Reduction Initiative (GTRI) programme (Phillips et al., 2016). Several preliminary studies were carried out to ensure minimal change in the lifetime and performance of GHARR-1 as well as its safety features after the HEU core is replaced with the LEU core (Odoi et al., 2012). In order to determine the critical mass, control rod worth, top beryllium reflector worth, the neutron flux distribution and final loading of fuel elements, several experiments were carried out in the Zero Power Test (ZPT) facility for the Ghana MNSR at the Chinese facility. From the results of the experiment it was established that the Ghana MNSR is to contain 334 fuel elements with 16 dummy elements. The fuel elements comprise UO_2 fuel meat and zircaloy as cladding.

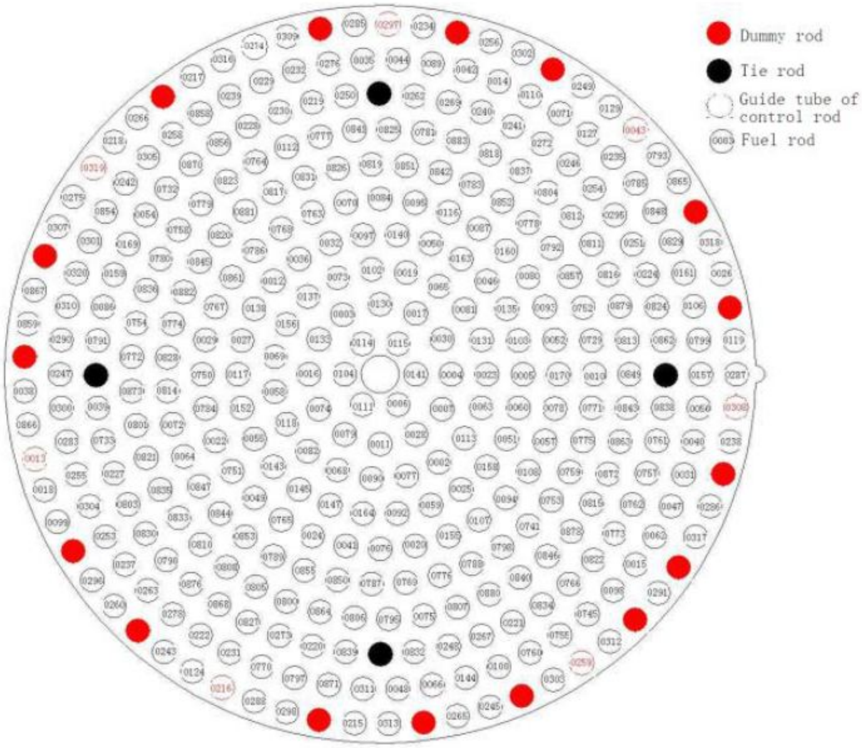

Figure 1.1: Fuel loading for the Zero Power Test at CIAE
("Report on Zero Power Test", 2016)

Figure 1.1 shows the core loading of the Ghana MNSR per the Zero Power Test experiment. The enrichment of the new GHARR-1 fuel has been reduced from 90.2 % to approximately 13 %.

The safe and effective utilization of a research reactor such as GHARR-1 is dependent on the knowledge of the behaviour of neutrons within the reactor. Acquiring information about the behaviour of neutrons within a specific volume is termed as characterization of the neutron spectra within that volume. When it comes to the utilization of the Ghana MNSR, the volumes of interest are the ten irradiation channels or sites it is equipped with. These irradiation channels are used for neutron activation analysis (NAA) experiments. It is expected as in many other research reactors, that the characteristics of the neutron spectrum at various irradiation sites differ from one another.

1.2 Problem Statement

Several studies have been conducted on the GHARR-1 HEU core to characterize the irradiation sites. Even though these studies were very useful, they are no longer valid due to the change in the reactor's core configuration and fuel type. Thus, there is a need for a study to be carried out to characterize the neutron spectra at the various irradiation sites of the new LEU core so as to acquire data which is a true representation of the current state of GHARR-1.

1.3 Objectives

The main objective of this study is to theoretically characterize the neutron spectra at the various irradiation sites of the current LEU core of GHARR-1 using the Monte Carlo method. In order achieve this objective, the following tasks will be carried out:

- Simulate and determine the neutron spectrum parameters (thermal, epithermal and fast neutron fluxes, thermal to epithermal flux ratio and epithermal neutron spectrum shaping factor) using Monte Carlo N-Particle (MCNP) code.
- Determine the neutron flux distribution within the volume of the irradiation site.
- Determine how theoretical results of the LEU comapre to that of the HEU (from previous studies, both theoretical and experimental).

1.4 Relevance and Justification

Studies carried out prior to the conversion of the GHARR-1 from an HEU fuel to LEU fuel reactor indicated that the LEU core will have similar neutronics, safety and thermal hydraulics characteristics as compared to the HEU core. There are however some physical differences, namely, fuel meat density, dummy pin arrangement and number of fuel pins in the LEU core design as compare to the HEU core. These changes may have a effect on the neutron spectrum characteristics. Knowledge of these characteristics from the on set (fresh fuel characteristics) helps establish baseline data to be used as reference for future characterization works. Also some of these parameters (thermal-to-epithermal neutron flux ratio, epithermal neutron spectrum shaping factor and flux distribution) are important in applying the K_o method for neutron activation analysis.

1.5 Scope

The GHARR-1 MCNP model used for this study was modified based on the results of the zero power experiment carried out in Beijing by the CIAE as well as on site measurements of some components. Data for the determination of the neutron spectrum parameters as well as the reaction rate and cadmium ratio of foils were gathered within the volume of the rabbit capsules at the various irradiation sites.

1.6 Overview of Study

Chapter 1: Introduction - Highlights on the background, motivation, relevance and scope of the work.

Chapter 2: Literature Review - This chapter highlights the theories behind neutron interaction and cross sections. The Chapter again focuses on the neutron energy spectrum and neutron spectrum parameter characterization. Monte Carlo methods and the theory for the MCNP code are described in this chapter. It also provides a description of GHARR-1 and its irradiation facility. The chapter reviews the development of MNCP models of the GHARR-1 and irradiation facility characterization studies carried out in previous years. Finally, the effect of HEU to LEU core conversion on irradiation sites of other research reactors have been elaborated in this chapter.

Chapter 3: Materials and Methods - A description of the materials, tools and methodology used for the characterization of the neutron spectra at the various irradiation sites.

Chapter 4: Results and Discussion - A discussion of the results obtained from the study, with a comparison of neutron fluxes, flux distribution and neutron spectrum parameters between the LEU and HEU cores.

Chapter 5: Conclusions and Recommendations - Concluding remarks about the study and recommendations for improvements.

CHAPTER 2

LITERATURE REVIEW

In this chapter neutron interactions and neutron energy spectrum are discussed. The theory behind Monte Carlo methods as employed in the MCNP code and that of neutron spectrum parameter characterization are also discussed. This chapter also gives a description of GHARR-1 together with its history and the development of the GHARR-1 MCNP model. It provides a summary of literature available on neutron spectrum characterization using both Monte Carlo and experimental methods at GHARR-1. Additionally, the effect on neutron spectrum parameters as a result of HEU to LEU conversion of some research reactors is discussed.

2.1 Theory

2.1.1 Neutron Interactions

Throughout the lifetime of a neutron in a nuclear reactor, it undergoes several interactions with its surrounding material (target nuclei) . The neutron's lifetime comes to an end after it has been either absorbed by a target nucleus. The probability that a particular interaction will take place is termed as the cross section of that interaction. In neutron transport, there are two main types of interactions, absorption and scattering. Both of these interactions have their respective absorption and scattering cross sections. The sum of these two cross sections is termed as the total cross section as shown in equation (2.1).

$$\sigma_T = \sigma_a + \sigma_s \tag{2.1}$$

σ_T is the total cross section, σ_a is the absorption cross section and σ_s is the scattering cross section. Scattering cross section can be further categorized into elastic and inelastic scattering cross section. In elastic scattering interactions, both the momentum and energy of the neutron are conserved. With inelastic interactions however, both energy and momentum are not conserved. The neutron upon scattering with a target nucleus loses energy to it leaving the nucleus in an excited state. The excess energy absorbed by the excited target nucleus is emitted as radiation (alpha, beta or gamma) in a bid to return to its ground state. Mathematically, scattering cross section is illustrated in equation (2.2).

$$\sigma_s = \sigma_e + \sigma_i \tag{2.2}$$

σ_e is the elastic scattering cross section and σ_i is the inelastic scattering cross section. Similarly, absorption cross section is categorized into fission and capture cross sections with respect to the fission and neutron capture processes. When a neutron is absorbed by a nucleus a compound nucleus is formed. This compound nucleus may undergo fission, splitting into two parts and releasing alongside energy two or more neutrons. In the case of neutron capture, the compound nucleus de-excites to its ground state emitting prompt gamma rays. The de-excited nucleus may be radioactive at its ground state and decays emitting delayed gamma energy. The emission of prompt and delayed gamma energy by a compound nucleus (n,γ) reactions forms the basis of neutron activation analysis (NAA). The cross section for an (n,γ) reaction primarily depends on the energy (velocity) of incident neutron. Generally cross section is inversely proportional to neutron energy.

2.1.2 Neutron Energy Spectrum

In research reactors, neutrons have an energy distribution (neutron energy spectrum) as shown in Figure 2.1.

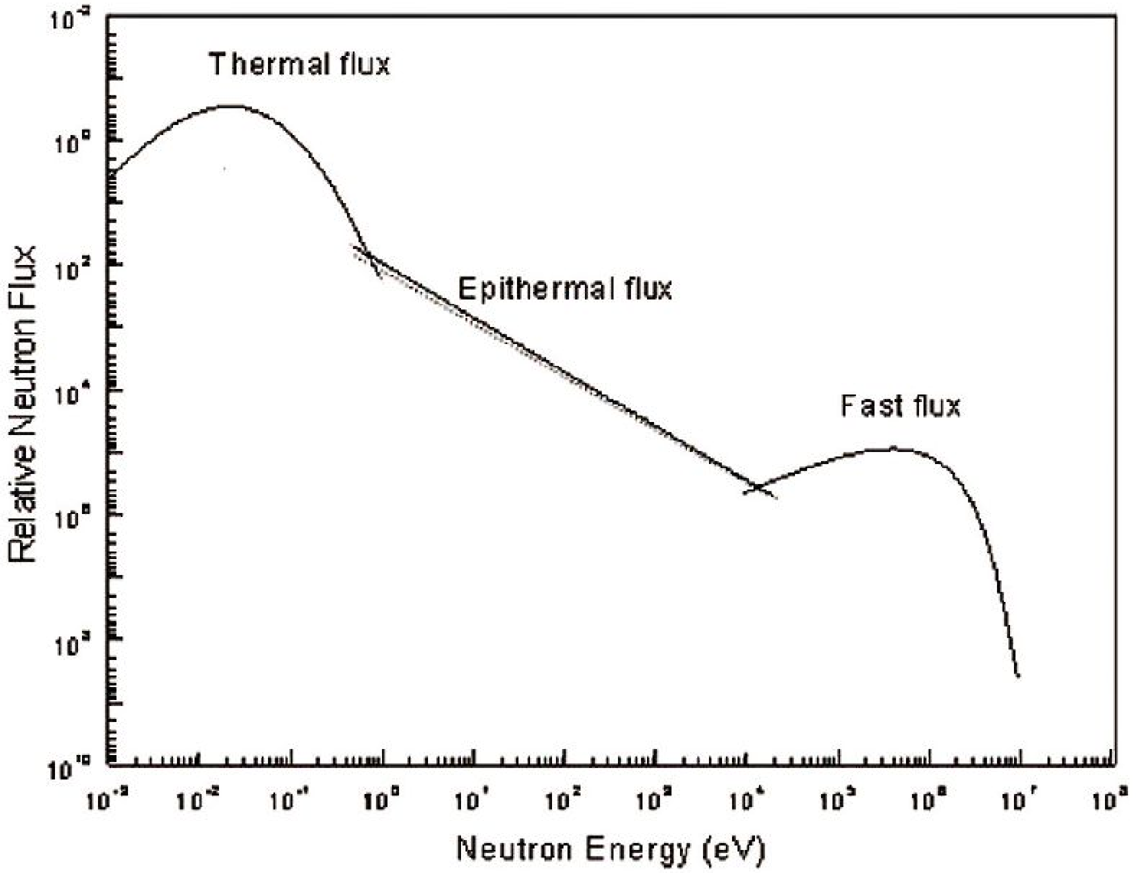

Figure 2.1: Neutron energy spectrum
(Hamidatou, Slamene, Akhal, & Zouranen, 2013)

As seen in Figure 2.1, the energy distribution consists of three regions, thermal, epithermal and fast energy regions. Neutrons are generally born in the fast energy region after a fission process. As they interact with surrounding materials (moderator, fuel clad, coolant and so on) they rapidly lose energy transitioning into the epithermal energy region then finally the thermal region or directly to the thermal region.

2.1.2.1 Fast Neutron

Fast neutrons have energies ranging between 0.1 MeV and 20 MeV with 0.75 MeV being their most probable energy. Generally these fast neutrons form about five percent (5 %) of the total neutron population at irradiation sites (Glascock, 2015). Due to their high energies they hardly contribute to (n,γ) reactions. The fast energy spectrum as illustrated in Figure 2.1 is approximated by the Watt fission spectrum equation displayed in equation (2.3), where E is the neutron energy.

$$\chi(E) = 0.453e^{-(1.036)}\sinh(2.29E)^{1/2} \tag{2.3}$$

2.1.2.2 Epithermal Neutrons

The epithermal neutron energy range (0.55 eV to 0.1 MeV) is directly beneath that of the fast neutrons. Depending on the material they interact with, they are either absorbed or further lose energy via scattering processes. Epithermal neutrons account approximately two percent (2 %) of the total neutron population at irradiation sites. Ideally, the epithermal neutron energy distribution is inversely proportional to the neutron energy as illustrated in Figure 2.1.

2.1.2.3 Thermal Neutrons

Right below the lower limit of the epithermal energy range is the thermal neutron energy range (< 0.55 eV). Thermal neutrons are neutrons which are in thermal equilibrium with its surroundings (moderator). The energy distribution of thermal neutrons is best described by the Maxwellian distribution. Equation (2.4) below describes the Maxwellian distribution.

$$f(E) = \frac{2\pi\sqrt{E}e^{-(E/kT)}}{(\pi kT)^{3/2}} \tag{2.4}$$

k is Boltzmanns constant and T is the temperature of the medium in Kelvin. GHARR-1 operates at room temperature (20 ^{o}C). At this temperature, the most probable energy of neutrons in the thermal energy range is 0.0253 eV (Moteff et al., 1970).

2.1.3 (n,γ) Reactions

When a nuclide is bombarded with neutrons, the (n,γ) reaction rate, R (measured in per second, s^{-1}) per nuclide is given by equation (2.5).

$$R = \int_0^\infty \sigma(v)\varphi'(v)dv = \int_0^\infty \sigma(E)\varphi'(E)dE \tag{2.5}$$

E is the energy of the neutron and v is its velocity. E and v can be used interchangeably since E is directly proportional to v ($E = {}^1\!/\!{}_2 m_n v^2$, m_n is the mass of a neutron). $\sigma(v)$ and $\sigma(E)$ are the neutron cross sections with respect to velocity, v and energy, E. $\varphi'(v)$ and $\varphi'(E)$ are neutron flux per unit velocity interval at velocity, v and per unit energy at energy, E respectively. A number of formalisms or conventions based on some neutron characteristics (neutron cross section and energy distribution) have been adopted in determining R in equation (2.5) instead of solving the integral (Frans De Corte, 1987). For this study the Hogdahl convention will be used.

2.1.3.1 Hogdahl Convention

The rate of (n,γ) reactions of a nuclide reduces enormously when irradiated under a cadmium (Cd) cover. This is due to cadmium's high cross section for neutrons in the thermal energy region. As shown in Figure 2.2, this is largely due to the resonance at 0.178 eV of ^{113}Cd (Frans De Corte, 1987).

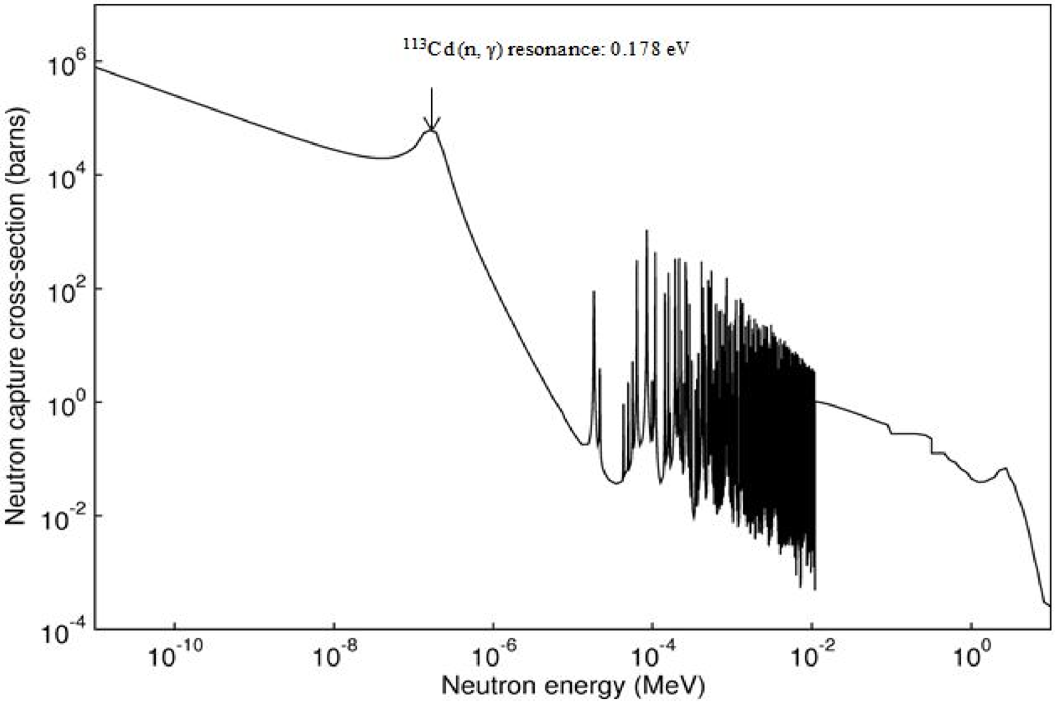

Figure 2.2: Cross section curve of cadmium
(Frans De Corte, 1987)

For a nuclide irradiated in a stable neutron flux under cadmium cover, all neutrons with energies below the cadmium cut off energy ($E_{Cd} = 0.55$ eV) are absorbed. This value of E_{Cd} is only valid on the conditions that, nuclide of flux monitor is place approximately at the centre of a 1 mm thick cylindrical cadmium cover with a height to diameter ratio of 2 and its neutron cross section is inversely proportional to the neutron velocity up to neutron energy of approximately 1.5 eV ($\sigma(v) \sim 1.5$ eV) (Frans De Corte, 1987).

The Hogdahl convention makes use of the E_{Cd} concept. Applying this to equation (2.5), the right hand side (R.H.S) can be split into two parts as shown in equation (2.6).

$$R = \int_{0}^{v_{Cd}} \sigma(v)\varphi'(v)dv + \int_{E_{Cd}}^{\infty} \sigma(E)\varphi'(E)dE \tag{2.6}$$

Considering the first term on the R.H.S of equation (2.6),

$$\sigma(v) = \frac{\sigma_0 v_0}{v} \tag{2.7}$$

Equation (2.7) is true for nuclides with $\sigma(v) \sim {}^1\!/_v$ up to v_{Cd} (Frans De Corte, 1987). σ_0 is termed as the cross section at thermal neutron velocity ($v_0 = 2200\,\mathrm{ms}^{-1}$). Also,

$$\varphi'(v)dv = n'(v)dv \tag{2.8}$$

$n'(v)$ is the number of neutrons with velocity v.

$$\int_0^{v_{Cd}} n'(v)dv = n_{th} \tag{2.9}$$

Putting equations (2.7), (2.8) and (2.9) into equation (2.6),

$$R = \sigma_0 v_0 n_{th} + \int_{E_{Cd}}^{\infty} \sigma(E)\varphi'(E)dE \tag{2.10}$$

In a typical thermal reactor such as GHARR-1, the epithermal neutron flux distribution does not follow the ideal ${}^1\!/_E$ distribution. This non ideality is accounted for by the introduction of the term epithermal neutron spectrum shaping factor (α). Thus, the epithermal neutron flux distribution is approximated by the ${}^1\!/_{E^{1+\alpha}}$ distribution ($\varphi'(E) = {}^1\!/_{E^{1+\alpha}}$) (Jovanovic et al., 1988). The value of α can be either positive or negative. When α is positive it indicates a softened epithermal neutron spectrum, while a negative value indicates hardened epithermal neutron spectrum. Figure 2.3 illustrates the concept of $\varphi'(E) = {}^1\!/_{E^{1+\alpha}}$ distribution.

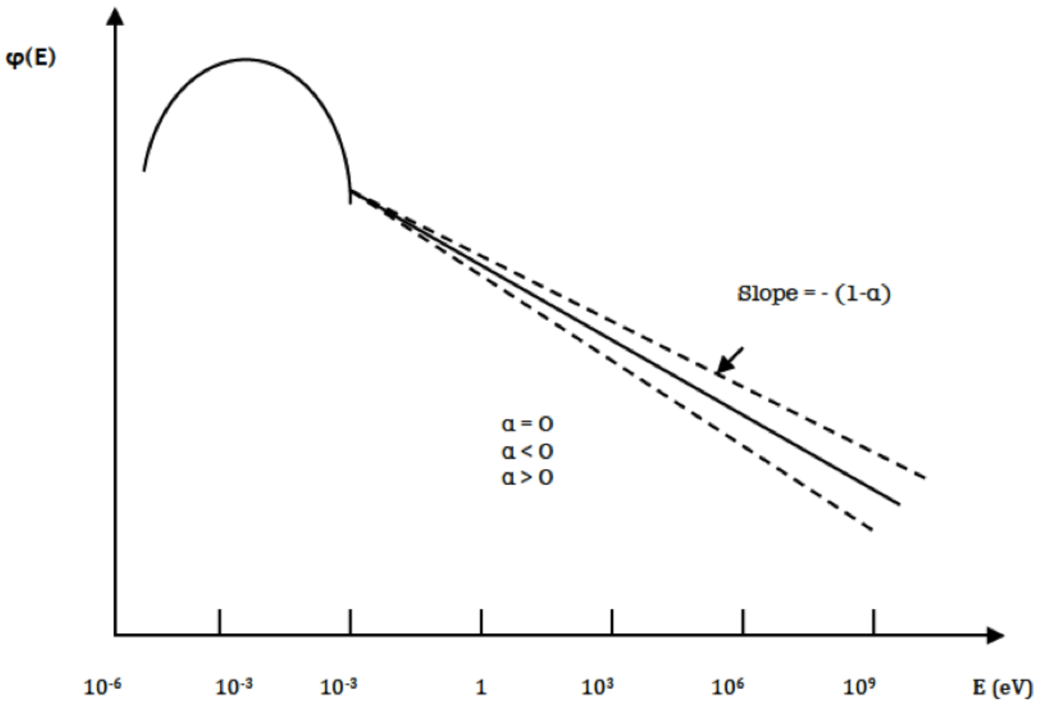

Figure 2.3: Non ideality of epithermal neutron flux distribution
(Jovanovic et al., 1988)

Considering the non-ideal epithermal neutron flux distribution and a reference energy of 1 eV,

$$\varphi'(E) = \frac{\phi_{epi} 1\mathrm{eV}^{\alpha}}{E^{1+\alpha}} \tag{2.11}$$

ϕ_{epi} is the conventional epithermal neutron flux measured in $\mathrm{cm}^{-2}\mathrm{s}^{-1}$. Putting (2.11) into equation (2.10),

$$R = \sigma_0 v_0 n_{th} + \phi_{epi} 1\mathrm{eV}^{\alpha} \int_{E_{Cd}}^{\infty} \frac{\sigma(E)dE}{E^{1+\alpha}} \tag{2.12}$$

$$I_0(\alpha) = 1\mathrm{eV}^{\alpha} \int_{E_{Cd}}^{\infty} \frac{\sigma(E)dE}{E^{1+\alpha}}$$

$$R = \sigma_0 v_0 n_{th} + \phi_{epi} I_0(\alpha) \tag{2.13}$$

The conventional thermal neutron flux,$\phi_{th} = n_{th}v_0$. Putting this into equation (2.13),

$$R = \phi_{th}\sigma_0 + \phi_{epi}I_0(\alpha) \tag{2.14}$$

The first term on the R.H.S of equation (2.14) is the rate of reaction as a result of thermal neutrons and the second term is as a result of epithermal neutrons. Taking into account both thermal and epithermal neutron self-shielding by the flux monitors, the thermal and epithermal self-shielding factors are introduced into equation (2.14). Thus, equation (2.14) becomes (2.15).

$$R = G_{th}\phi_{th}\sigma_0 + G_{epi}\phi_{epi}I_0(\alpha) \tag{2.15}$$

G_{th} and G_{epi} are the thermal and epithermal self-shielding factors respectively.

2.1.4 Neutron transport theory

To theoretically predict the behaviour of neutrons in a system or assembly such as a nuclear reactor requires solving the neutron transport equation. This neutron transport equation (as shown in equation (2.17)) except in simple cases is difficult to solve analytically. Thus solutions to the neutron transport equation are usually based on numerical methods. The neutron transport equation is derived by simple balancing of the various processes by which neutrons are added or removed from a system as shown below.

$$\begin{bmatrix} \text{Time rate of change} \\ \text{of neutron density} \end{bmatrix} = \begin{bmatrix} \text{Change due to} \\ \text{physical leakages} \end{bmatrix} + \begin{bmatrix} \text{Change due} \\ \text{to collision} \end{bmatrix} + [Sources] \tag{2.16}$$

Equation (2.16) is expressed mathematically in equation (2.17)

$$\frac{1}{v}\frac{\partial}{\partial t}\phi(r,\Omega,E,t) + \Omega.\Delta\phi(r,\Omega,E,t) + \Sigma_t(r,E,t)\phi(r,\Omega,E,t) = q(r,\Omega,E,t) \tag{2.17}$$

$\frac{1}{v}\frac{\partial}{\partial t}\phi(r,\Omega,E,t)$ represents the rate of change of neutron density with respect to time, $\Omega.\Delta\phi(r,\Omega,E,t)$ is the neutron leakage term, $\Sigma_t(r,E,t)\phi(r,\Omega,E,t)$ is the total neutron reaction cross section term and $q(r,\Omega,E,t)$ is the source term. r, E, t and Ω are the position vector, energy, time and direction vector terms respectively.

Generally there are two main methods employed in solving the neutron transport equation, namely, the deterministic and stochastic (monte carlo) methods. The deterministic methods solve the neutron transport equation in a numerically approximated manner throughout the modeled system. Thus, for deterministic methods simple geometries are required for solving the neutron transport equation. In deterministic methods, multigroup approximation of cross section data is employed (Schwerer, 2001). In the case of monte carlo methods, the problem geometry is almost exactly if not exactly modeled. Thus monte carlo methods are able to deal with complex systems such as a nuclear reactor. Monte carlo methods make use of continuous energy cross section data as well as multigroup cross section data (Schwerer, 2001). The monte carlo method is a statistical method and thus results of calculations using this method are presented as estimates with their associate uncertainties. It is thus generally said that deterministic methods provide an exact solution to an approximated problem or model while monte carlo methods solves the exact problem and provides estimates as solution to the problem.

2.1.5 Monte Carlo methods

In simulating a physical process (such as neutron particle transport) using monte carlo methods, each and every neutron is actually followed from its source (at birth) throughout its lifetime (scattering processes) till death via absorption or leakage from the system of interest. This represents what is termed as the random history of a particle (Booth et al., 2003). Based on some equations of physics and probabilities (cross section data), random numbers between 0 and 1 are selected to ascertain the type of interaction that takes place at various points in the volume of interest as well as where the interaction occurred (Booth et al., 2003). Figure 2.4 illustrates the random history of a neutron incident on a slab of fissionable material and the fission neutrons that emerge.

The numbers in Figure 2.4 represent the various events that make up the history of the neutrons.

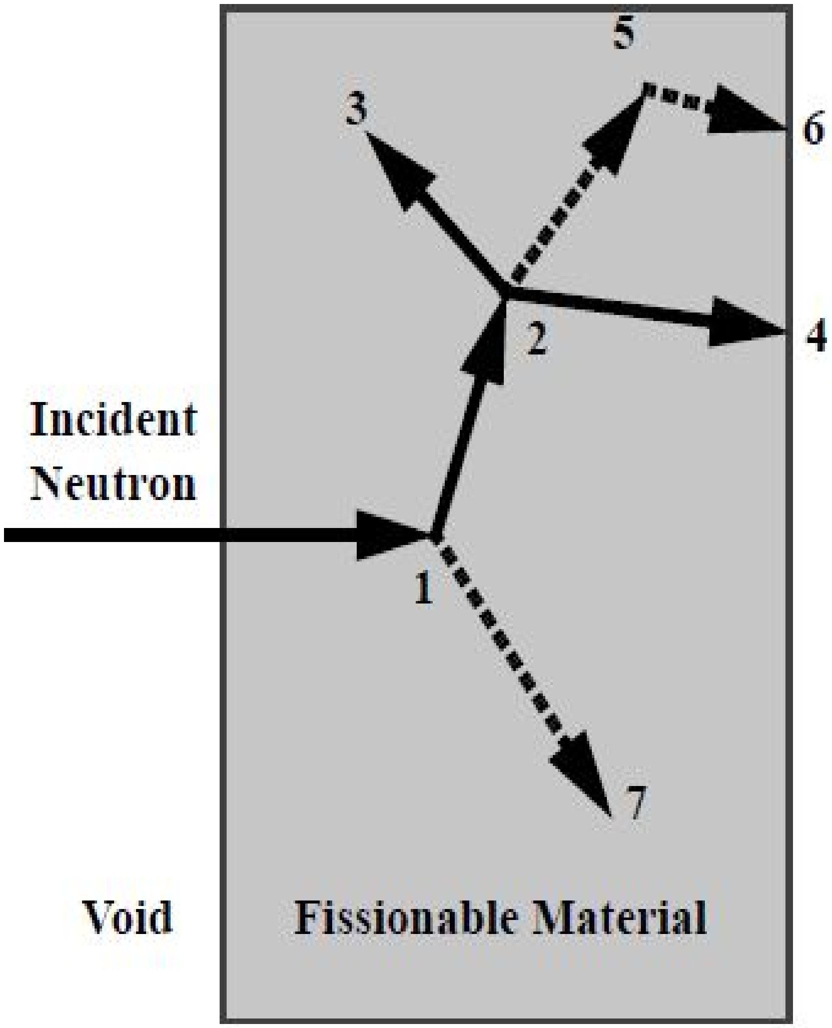

Figure 2.4: Random history of neutrons
(Booth et al., 2003)

At 1, the incident neutron is scattered producing a photon which is banked or stored to be analysed later. At 2, the scattered neutron is absorbed (death of incident neutron) by the slab resulting in the birth of two neutrons (fission neutrons) and a photon. One of the fission neutrons and the photon are banked. The other fission neutron is captured at 3 bringing its lifetime to an end. The other fission neutron is retrieved and leaks (death) out of the slab at 4. The fission photon is then retrieved, scatters at 5 and leaks out at 6. Finally, the photon produced as a result of the scattering of the incident neutron is retrieved and its captured at 7. In monte carlo simulations the retrieval of banked particles or photons follows the last in first out principle (Booth et al., 2003).

In a typical monte carlo simulation millions of events (particle or photon histories) are followed, thus giving a better known particle or photon distribution at various regions of interest. At these regions, estimates of quantities such as the number of collisions, particle track length and so an are made. Since the monte carlo method is statistical in nature any quantity (neutron flux in this study) desired by the user is presented with their associated uncertainties.

2.1.6 MCNP calculations

MCNP is a computational tool that calculates various quantities pertaining to nuclear reactions in a particular region of interest. Its calculations are based on monte carlo methods. To do a calculation using MCNP, the user has to first create an input file (deck). The input deck describes the problem geometry or structure (for this study a nuclear reactor) and its material specifications using surface, cell and data cards. The surface cards can be referred to as the basic element of the problem geometry. It specifies the various surfaces (such as planes, cylinders, cones and so on), their dimensions and orientation in the x,y,z coordinate system. Each surface card is identified by is a positive integer (surface number). Using the intersection, union and complement operators surfaces are combined to form volumes called cells. These cells are defined using the cell card which specifies the material composition (via material number), density and particle or photon importance of the cell (importance of 0 means particle history is not tracked in the cell while importance of 1 is the vice versa). A material number is used to distinguish between the various material cards. Material cards form part of the data cards which also specifites the source(s) of particles or photons and their position in the problem geometry. Thus all neutron sources in this study must be specified so as to statistically simulate neutron reactions in the reactor core. For critical systems such nuclear reactors, the kcode card must be defined. This card specifies the number of neutrons per cycle, the initial guess of the multiplication factor (k-effective, k_{eff}), the number of cycles to be skipped before accumulating data and the total number of cycles to run (Brewer, 2009). Finally, the desired data output is defined using the tally card. The kcode and tally cards also form part of the data card. The tally card specifies the cells whose calculation data should be presented. There are several tally card types. For this study the F4 tally is employed. Figure (2.5) shows a flow chart illustrating how MCNP calculations are carried out.

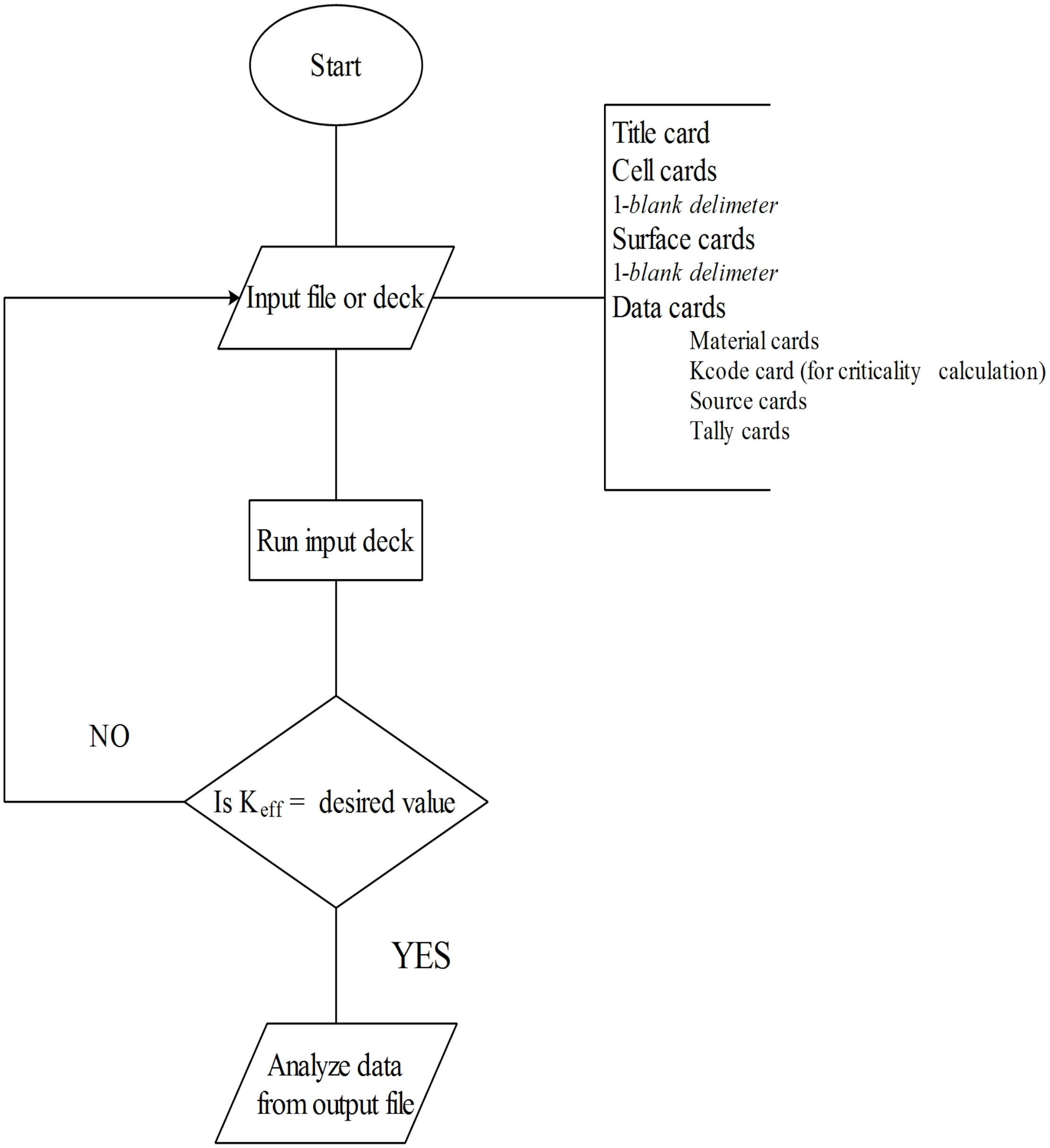

Figure 2.5: Flow chart of the MCNP code

2.1.6.1 Criticality calculations in MCNP

For critical systems, the parameter of prime interest is the multiplication factor (k-effective, k_{eff}). It is defined as the ratio of the neutron population of a generation to the neutron population in the preceding generation. In MCNP criticality calculations are controlled by the kcode card. With the kcode card a generation is referred to as a k_{eff} cycle. At the end of a MCNP simulation the final estimate of the k_{eff} is given as the average over all the simulated k_{eff} cycles. As with every monte carlo calculation, the final estimate of the k_{eff} comes with its associated uncertainty. The uncertainty decreases as the number of k_{eff} cycles increase. Thus for a good estimate of the final k_{eff} of a critical system, it is important that a substantial number of k_{eff} cycles are simulated. The kcode card in MCNP requires three input parameters, namely, the total number of k_{eff} cycles, initial guess of k_{eff} and the number of initial cycles to be skipped. It is necessary for some cycles to be skipped since monte carlo spatial neutron distribution, which is dependent on the eigenvalue and geometry of the system of interest takes some time to converge (Brewer, 2009). These skipped cycles are ignored when the final k_{eff} is calculated.

Consider a criticality problem where C number of cycles are to be simulated and S number of initial cycles to be skipped. The final estimate of k_{eff}, $\bar{k}$ is given by equation (2.18).

$$\bar{k} = \frac{1}{(C-S)} \sum_{i=S+1}^{C} k_i \tag{2.18}$$

k_i is the multiplication factor of the ith cycle. The uncertainty in $\bar{k}$ is estimated as the standard deviation, σ, of the distribution of k_{eff} values. Equation (2.19) how σ is calculated.

$$\sigma = \sqrt{\frac{1}{(C-S-1)} \sum_{i=S+1}^{C} (k_i - \bar{k})^2} \tag{2.19}$$

2.1.6.2 Nuclear reaction data libraries

Nuclear reaction data describes the interaction of particles such as neutrons and photons with their target nuclei. It basically consists of cross section as well as angular and energy distribution of particles emitted as a result of nuclear interactions (Schwerer, 2001). Information for nuclear reaction tables are obtained from experiments as well as evaluated data. For computational tools such as MCNP, evaluated data is employed. Evaluated data is arrived at after critical analysis of experimental and/or theoretical data and their uncertainties as well as interpolated and extrapolated data and nuclear model calculations (Schwerer, 2001). Nuclear reaction data is summarized and organized into libraries with specific data formats. The international format for nuclear reaction data is the Evaluated Nuclear Data Files (ENDF) format (Booth et al., 2003). In the case of MCNP, which will be used for this study, several ENDF formatted data libraries complied by laboratories and data centres exist. These include ENDF/B by the Cross Section Working Group (CSEWG), USA, JENDL by the Japanese Atomic Energy Research Institute, the European JEFF library by Nuclear Energy Agency (NEA) and CENDL by Chinese Nuclear Data Centre (CNDC). To utilize any of these libraries when running a MCNP simulation, the ENDF format data is processed into a so called A Compact ENDF (ACE) format (Schwerer, 2001). The processing of the data library is done by the NJOY code making sure that nuclear data libraries retain as much detail from the original evaluations as possible.

For target nuclei with low mass numbers embedded in a molecule or lattice interacting with a low energy or thermal neutron, the scattering properties or cross section are different. They do not just depend on the target nuclei and the energy of incident particle, but also on the binding effects of the host material and the possibility of vibrational modes being exparencited (Brewer, 2009). MCNP uses $S(\alpha, \beta)$thermal neutron laws to account for this effect. Since the binding effect depends on the host material, MCNP has for example, different $S(\alpha, \beta)$ scattering data for hydrogen in water and in polyethylene.

2.1.6.3 Tally specification in MCNP

Tallying in MCNP allows the user to define the output or information desired from the calculation and how this information is presented in the output file. Tally cards are employed in the MCNP code to accomplish this task. The Fn card is required for all tally specifications in MCNP. Other tally cards are available to provide additional features and these are all optional. There a number of Fn cards. For this study, the F4 card (used to determine neutron flux in a cell) is employed. The auxiliary tally cards used in this study include the tally segment (FSn), tally multiplier (FMn) and tally energy (En) cards. The En card is used to specify the energy ranges for which results or fluxes should be outputted. For each energy range, the user states its upper limit in MeV. Energy ranges are to be listed in ascending order. The FS card based on surfaces described in the surface card section of the input file divides a particular volume into various segments. These segments however do not appear in the geometry of the system being modeled. The F4 and FM card tally cards are described in appendix A.

2.2 Description of GHARR-1

The Ghana Research Reactor-1 is a low power tank-in-pool type research reactor. It is a commercial version of the MNSR designed and manufactured by the China Institute of Atomic Energy (CIAE), China (Gbadago et al., 2011). The GHARR-1 was designed basically for Neutron Activation Analysis (NAA), production of short-live radioisotopes and human resource development in nuclear engineering and physics. The core of GHARR-1 resides at the bottom of an aluminium vessel (reactor vessel) and suspended in a stainless steel-lined light water concrete pool. The reactor core consists of fuel and dummy elements, tie rods, two grid plates and a central guide tube forming a cage (element cage). It has 354 lattice positions which form 10 concentric rings about the central guide tube which houses the reactor's only control rod. Screws connecting the grid plates and the four tie rods together occupy four of the lattice positions. The remaining 350 lattice positions are occupied by the fuel and dummy elements. Around the core is an annular beryllium reflector and beneath it as well is a beryllium reflector. Above the core is an aluminium shim tray which makes provision for beryllium reflectors to be added above the core. These reflectors enhance neutron economy since the small size of the core results in neutron leakage (Ahmed et al., 2006). There are five irradiation channels inside and five irradiation channels outside the annular beryllium reflector. Inside the annular reflector are two miniature fission chambers used for the detection of thermal neutron flux at the inner irradiation sites. Light water is used as moderator and coolant for GHARR-1. Figures 2.6 and 2.7 show the vertical and horizontal cross sections of GHARR-1.

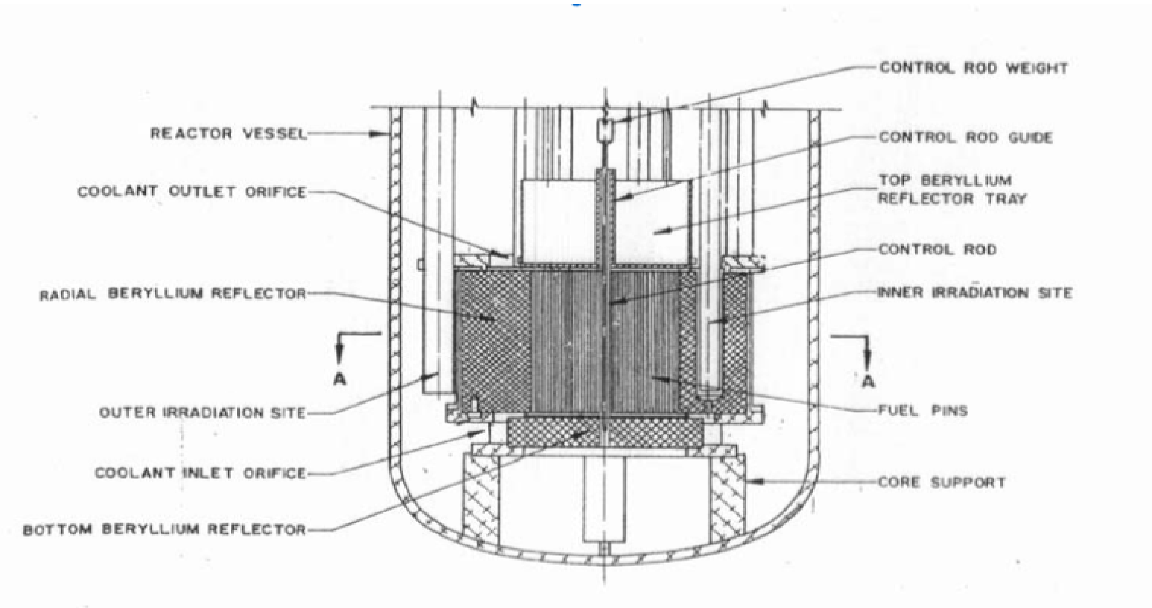

Figure 2.6: Vertical cross section of GHARR-1
(Gbadago et al., 2011)

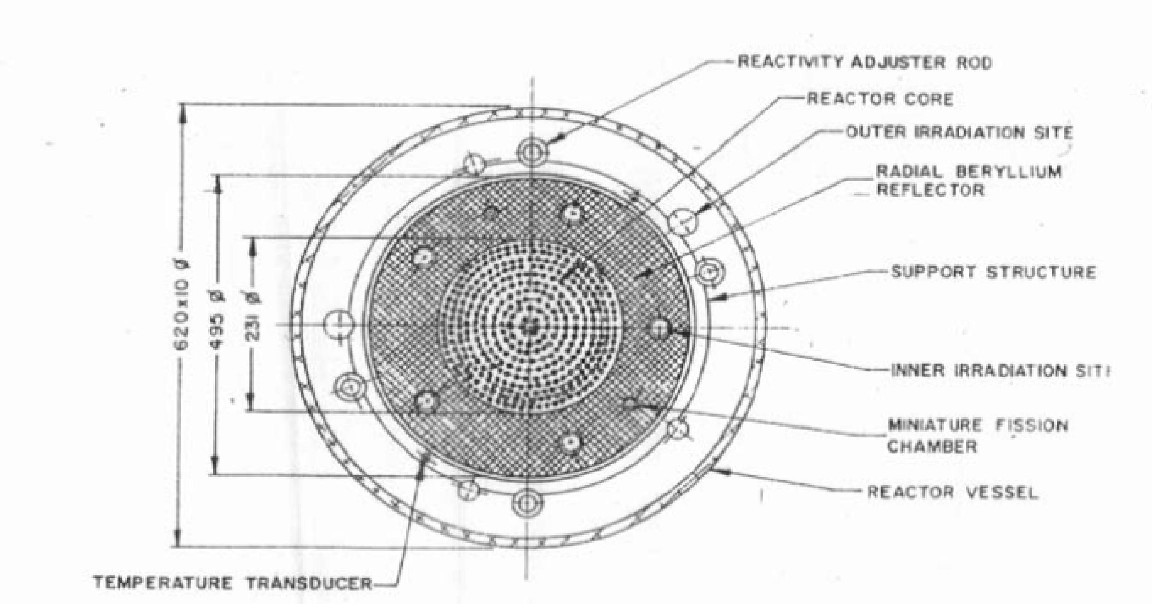

Figure 2.7: Horizontal cross section of GHARR-1
(Gbadago et al., 2011)

2.2.1 GHARR-1 HEU core

The GHARR-1 HEU core consists of 344 fuel elements and 6 dummy elements. The fuel meat is made up of uranium dispersed in aluminium matrix (UAl_4) with aluminium as material for fuel meat clad as well as dummy elements (Gbadago et al., 2011). The enrichment level for the fuel meat is 90.2 %. The upper and lower grid plates and the control rod guide tube are also made of aluminium. The control rod consists of cadmium with stainless steel cladding.

2.2.2 GHARR-1 LEU core

The GHARR-1 LEU core consists of 334 fuel elements and 16 dummy elements. The fuel meat is made up of uranium oxide (UO_2) with enrichment levels of 13.0 % ("Report on Zero Power Test", 2016). The fuel meat clad, dummy elements, upper and lower grid plates and control rod guide tube are made up of zircaloy-4 (ZIrc-4). The control rod consists an aluminium (Al) rod clad with cadmium (Cd) which is also clad in stainless steel (SS)("Report on Zero Power Test", 2016). Table 2.1 compares the key features of the GHARR-1 HEU and LEU cores.

Table 2.1: Comparison of GHARR-1 HEU and LEU Core

(Gbadago et al., 2011; Odoi et al., 2012)

Parameter	HEU
Fuel Meat	U-Al
U-235 Total Core Loading	998
U-235 Enrichment, wt %	90.2
Density of Meat, g/cm^3	3.456
Meat Diameter, mm	4.3
Cladding Material	Al-303-1
Number of Fuel Rods	344
Power, KW	30
Material for Grid Plates	LT-21
Control Rod Material	Cd, SS

2.3 Monte Carlo Model of GHARR-1

The development of the Monte Carlo model of MNSRs began in the year 2001 at the Italian National Agency for New Technologies, Energy and Sustainable Economic Development (ENEA) Research Centre, Casaccia in Italy using the Monte Carlo N-Particle 4 (MCNP4) code (Anim-Sampong, Maakuu, & Akaho, 2007). The model was developed using available design data of structural components and materials of the Ghana MNSR (GHARR-1). Various geometries including planes, cones, spheres and cylinders were used to model the zones, materials and sections (such as fuel assembly, control system, reflectors, irradiation channels, shim tray, reactor vessel and reactor pool) of the MNSR. Approaches used in three dimensional (3D) combinatorial, generalized geometry and continuous energy methods as applied in MCNP were applied in developing the MNSR Monte Carlo model (Anim-Sampong et al., 2007). The centre of the reactor core was chosen as the geometrical centre of the MNSR model. Aside the cadmium cross section data which was chosen from the Evaluated Neutron Data File/B five (ENDF/B-V) data library, all other nuclear data for both fissile and non-fissile materials were chosen from the Evaluated Neutron Data File/B six (ENDF/B-VI) nuclear data library (Anim-Sampong et al., 2007). Thermal scattering in the reflector material (beryllium) and the hydrogen in the light water were treated using the special (α, β) scattering feature of the MNCP code. Figures 2.8 and 2.9 show the MCNP plot of the MNSR model in the x-y plane and the vertical cross sectional view respectively.

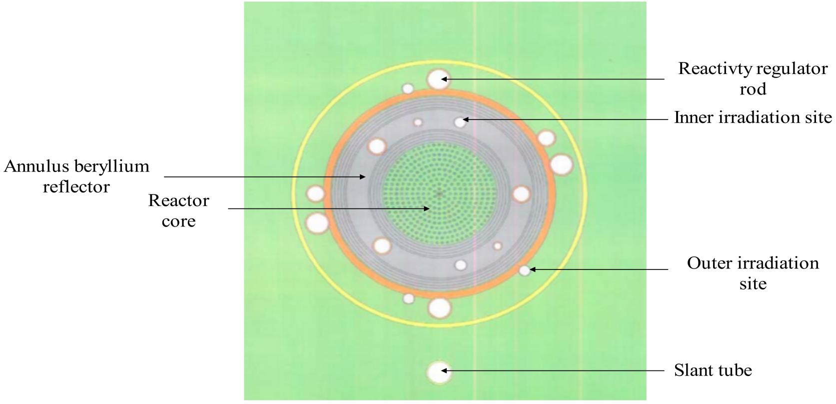

Figure 2.8: x-y view of the MCNP plot of MNSR model

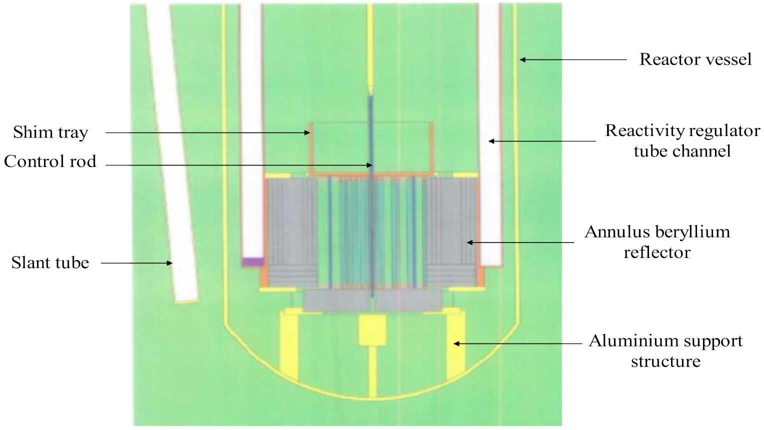

Figure 2.9: Vertical cross sectional of MNSR model

In the same vain, the computed control rod worth (-7 mk) and shutdown margin (-3 mk) differed by 10 % and 9 % respectively from the experimental results. These differences between the results from the Monte Carlo simulation and the experimental results was attributed to some approximations made to some parameters such as mass, dimensions and composition of some materials and structures in the development of the MNSR Monte Carlo model (Anim-Sampong et al., 2007). The trends of the axial and radial neutron flux distribution in the core, annular beryllium reflector and outer irradiation channel obtained from the Monte Carlo simulation compared very well with results obtained from the zero power and on-site criticality experiments. Due to the good agreement between the Monte Carlo results and the experimental results, it was concluded that Monte Carlo methods could be used to accurately model complicated geometries (such as MNSRs) and simulate physics and engineering design parameters as well (Anim-Sampong et al., 2007).

In the year 2007, the MNSR Monte Carlo model (developed in 2001/2002) was fine-tuned (by Sampong et al) to account for geometrical and material composition of some structural components. These structures included the honey combed grid plate, insertion of reactivity regulators and update of fuel element material composition (Anim-Sampong et al., n.d.). Figures 2.10 and 2.11 illustrate the cross sectional views of the fine tuned MNSR Monte Carlo Model. This study was carried out as a feasibility study for the proposed HEU-LEU core conversion of GHARR-1. Simulations were carried out for a reference HEU (90.2 %) fuel core and five candidate LEU fuel cores. The candidate LEU cores included 344 (12.6% enriched) fuel elements, 201 fuel elements (19.75 % enriched and 149 water dummies) and 238 (19.75 % enriched) fuel elements with 112 aluminium dummies. All the aforementioned candidate fuels had UO_2 as fuel meat. The remaining candidates were U-9Mo and U_3Si_2 dispersed in aluminium matrix with enrichment levels at 19.5 %. The parameters determined in the study included multiplication factor, core reactivity, thermal, epithermal and fast neutron flux variations at the irradiation channels. In addition to these, the axial thermal neutron flux distributions at the ten fuel lattice zones were determined. The final K_{eff} value estimated for the reference HEU fuel core was 1.00454 corresponding to a core reactivity of 4.519 mk (Anim-Sampong et al., n.d.). The K_{eff} values for the dispersant U-9Mo and U_3Si_2 candidate LEU fuel cores were up to 0.0023 % lower than the reference HEU core (Anim-Sampong et al., n.d.). The 12.6 % enriched UO_2 fuel core with the same configuration as the reference HEU core simulated the same K_{eff} value as the reference HEU model. The remaining UO_2 fuel cores reported K_{eff} values higher than the reference HEU core. The trend of the axial thermal neutron flux distribution (increasing from the bottom of the core, peaking at the centre then begins to decrease approaching the top of the core) along the fuel lattice zones obtained from the Monte Carlo simulation of the reference HEU core compares very well zero power and on-site experimental results.

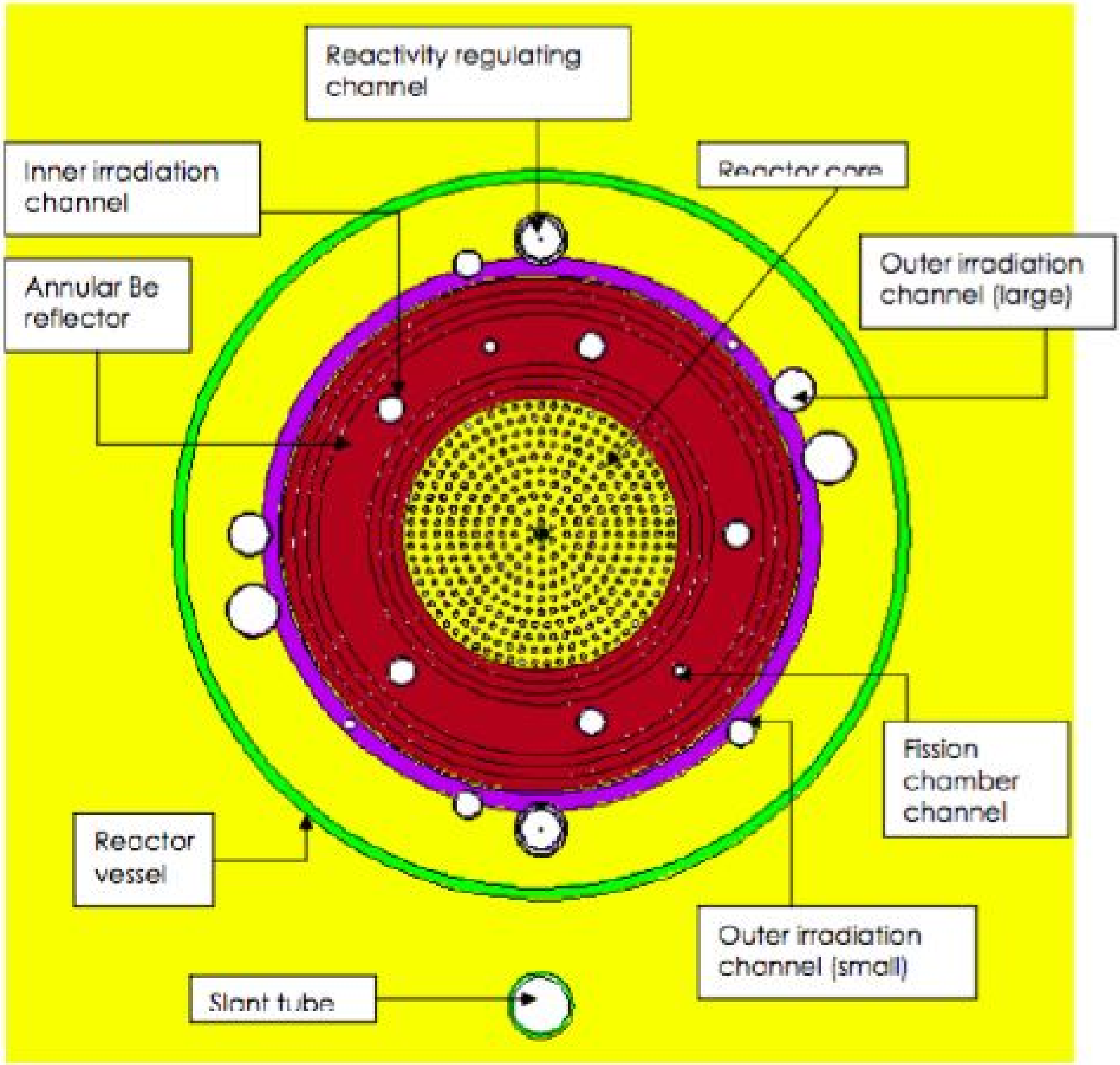

Figure 2.10: MCNP5 plot of the core configuration of the improved MNSR model (Anim-Sampong et al., n.d.)

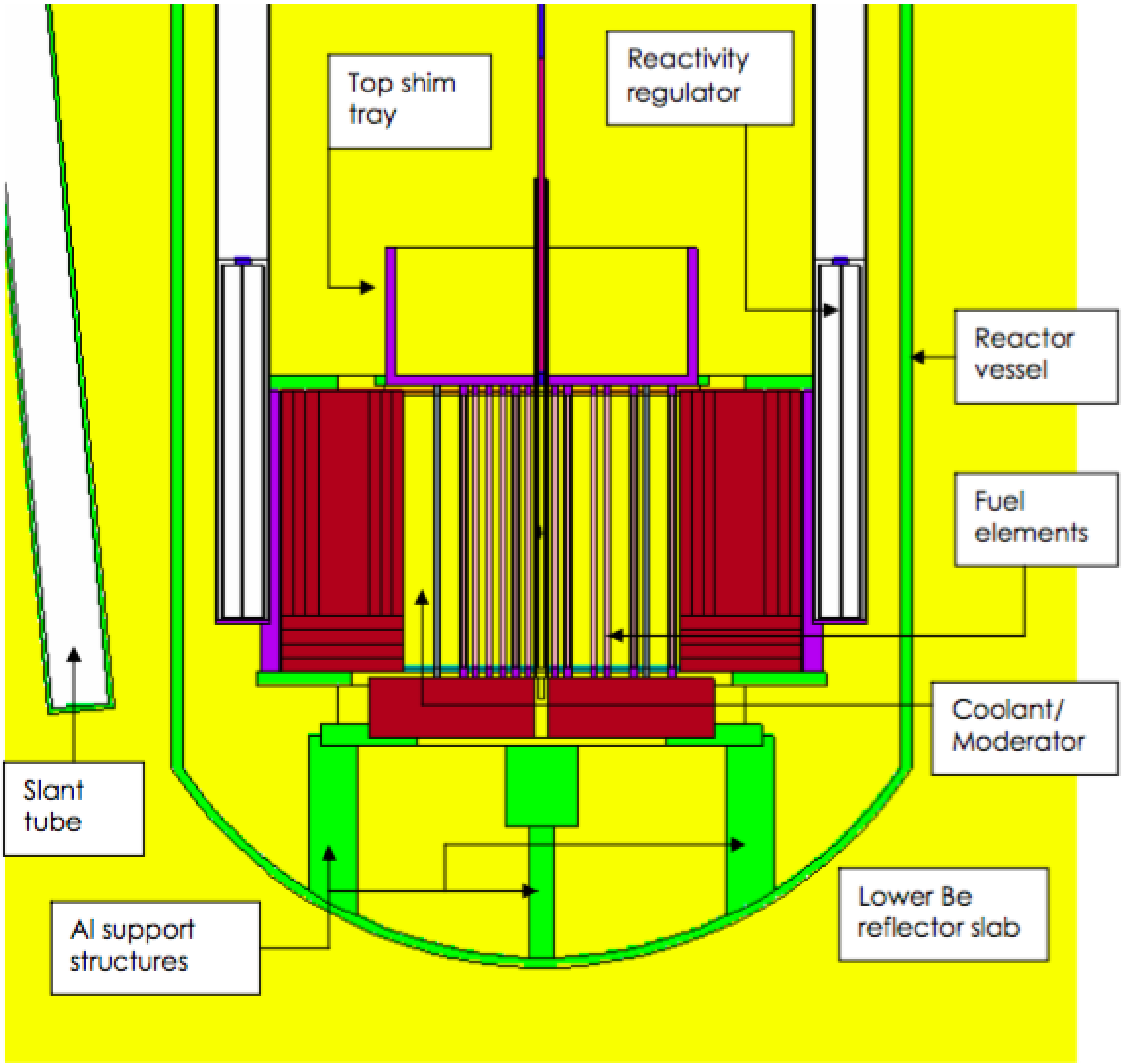

Figure 2.11: MCNP5 plot of vertical cross section of the improved MNSR model(Anim-Sampong et al., n.d.)

A similar trend was observed for all candidate LEU fuel cores. The simulation reported a reduced thermal neutron flux at the inner irradiation channels for the candidate LEU fuel cores. Despite this reduction, it was said that since the GHARR-1 operated at half flux most often it would not affect routine operation (Anim-Sampong et al., n.d.). Due to the good agreement between the reference HEU and the candidate LEU fuel cores, it was concluded that the improved MNSR Monte Carlo model was suitable for neutronic analysis of the Ghana MNSR. From the results of the simulations it was concluded that all the candidates could be utilized as fuel for the proposed GHARR-1 LEU fuel core

(Anim-Sampong et al., n.d.).

A study was undertaken by Odoi et al in 2012 to design an LEU core for GHARR-1. The LEU core was to have similar operational capabilities as the HEU core with acceptable safety margins under both normal and accident conditions (Odoi et al., 2012). As part of the study neutronic analysis was performed on both the HEU and LEU cores using MCNP5/X code. Table 2.2 compares the key parameters of the HEU and LEU cores used for the study (Anim-Sampong et al., n.d.).

Table 2.2: Comparison of specifications of core configurations

Parameter	HEU (344 pins)	LEU (344 pins)	LEU (348 pins)
Fuel Meat	UAl_4 in Al Matrix	UO_2 Pellets	UO_2 Pellets
Fuel Clad Type	303-1 Al alloy	Zircaloy-4	Zircaloy-4
Enrichment (U-235 wt%)	90.2	12.5	12.5
Density of fuel meat (g/cm^3)	3.456	10.6	10.6
U-235 loading per pin/core (g)	2.9/998.12	3.9/1341.6	3.9/1357.2
Uranium wt (%)	27.5	88	88

The 3-D MSNR Monte Carlo model was modified to reflect the material specifications of the core configurations in Table 2.2. Some of the neutronic parameters determined in the study were K_{eff} and its corresponding core reactivity as well as neutron flux distribution at some selected locations of the reactor. A zero fuel burn up was assumed for all simulations in the study. The criticality results indicated that the reactivity of the 344 LEU fuel pins core (2.88 mk) was below the minimum required 3.5 mk reactivity for operation of MNSRs (Odoi et al., 2012). However, that of the 348 LEU fuel pins core with reactivity of 3.84 mk was within the acceptable reactivity range (3.5 mk − 4.0 mk) and compared well with that of the 344 HEU fuel pins core (3.74 mk) (Odoi et al., 2012). The neutron flux variation at the irradiation sites of all the core configurations simulated in the study followed similar trends. It was found out that the thermal neutron flux at the inner irradiation channels of the LEU cores at 30 KW was lower than that of the HEU core. This necessitated the increment of reactor power in order to compensate for the loss in thermal neutron flux of the LEU cores. Based on the results obtained from the study it was concluded that the 348 fuel pin core configuration was suitable for the conversion of the HEU GHARR-1 core to LEU. Furthermore, the results showed that increasing the power of the reactor to 34 KW will compensate for the thermal neutron flux trade off at the inner irradiation channels (Odoi et al., 2012).

2.4 Characterization at GHARR-1 Irradiation Sites

In 2002, a study was carried out by Akaho and Nyarko to characterize two irradiation sites (site 1 and site 6) using the Westcott-formalism. The parameters determined were the modified spectral indices, Westcott g-factor, reduced resonance integral and neutron temperature. Gold solution, zirconium wire and lutetium nitrate solution of appropriate masses were irradiated with and without cadmium cover for the experimental work. Cadmium ratios of both $^1/_v$ nuclides (^{197}Au and ^{96}Zr) and non $^1/_v$ nuclides (Lu) were used to evaluate the modified spectral and Westcott g-factor respectively. The value of the Westcott g-factor was in turn used to evaluate the reduced resonance integral of Lutetium.

It was concluded that the programs developed in the study was suitable for calculating the epithermal flux shaping factor.

In 2010 a study was conducted by Abrefah et al to measure the variation (distribution) of neutron fluxes (axially and radially) at GHARR-1 irradiation channels using Monte Carlo methods. This was to ascertain whether there was a need to make corrections in the sample preparation protocol for neutron activation analysis. It was also to enquire whether there was a need to introduce a correction factor when calculating the concentrations of elements in samples (Abrefah, Anim-Sampong, Nyarko, Akaho, & Sogbadji, 2011). The MCNP input deck used for the study was obtained from a previous study in 2007 (Anim-Sampong et al., n.d.), (Abrefah et al., 2011). This deck was modified by modeling five smaller cylinders and arranging them across the radius of the irradiation channels so as to determine the radial flux distribution. For the axial flux distribution, the length of the irradiation channel was divided into ten equal parts. Two hundred million particle histories were simulated using the MNCP5 code with an initial K_{eff} of 1.004. From the results of the study it was observed that axially neutron fluxes generally increase from the bottom of the channel, peaks at its centre and gradually decreases moving up beyond the centre. This trend was similar to that reported in a previous study (Anim-Sampong et al., n.d.), (Abrefah et al., 2011). The peaking of neutron fluxes at the centre of the irradiation channel was attributed to the fact that the core of the reactor is located at the central region of the irradiation channel. Radially the thermal, epithermal and fast neutron fluxes (measured in $ncm^{-2}s^{-1}$) varied from 1.15×10^{12} to 1.19×10^{12}, 1.20×10^{12} to 1.36×10^{12} and 2.47×10^{11} to 2.97×10^{11} respectively for the inner irradiation sites. For the outer irradiation channels the thermal fluxes were reported to be between 7.14×10^{11} and 7.38×10^{11}, epithermal between 1.94×10^{11} and 2.51×10^{11} and fast between 3.69×10^{10} and 5.14×10^{10}. Generally, the radial flux distribution was flat for both inner and outer irradiation channels. However, the epithermal flux density was higher than the thermal fluxes at the inner channel and vice versa for the outer channel. This was attributed to the difference in the distances of the inner and outer channels from the reactor core (Abrefah et al., 2011). Thus lots of neutrons existed in the lower epithermal energy range when close to core and much more in the thermal energy range further away from the core. It was observed that due to the absorption of neutrons by annulus beryllium reflector around the core, the neutron fluxes at the outer irradiation sites were much lower compared to that of the inner channels. Due to the flat radial flux distribution at the irradiation channels, it was concluded that there was no need to incorporate a correction factor when calculating the elemental concentrations of samples. In the same vain there was no need in reviewing the sample preparation protocols (Abrefah et al., 2011).

In order to compensate for the loss of excess reactivity of the GHARR-1 core, a beryllium reflector was placed in the shim tray at the top of the core. After this, a study was carried out to determine the neutron spectrum parameters at one inner (site 2) and outer (site7) irradiation site. Gold alloy (Al-0.1%Au) wire samples were prepared and irradiated with and without cadmium cover. These samples were used to determine the neutron fluxes (thermal, epithermal and fast). Applying the dual monitor cadmium ratio method (using gold and zirconium wire), the epithermal neutron shaping factor was also determined. The results obtained indicated that the total neutron flux at the inner irradiation site was higher as compared to of the outer irradiation site. The fast neutron flux was observed to be higher than the epithermal neutron flux at the site 2 and vice versa for site 7. The ratio of the thermal to epithermal neutron flux for site 2 was almost twice of that of site 7. This was attributed to the higher level of thermalization at site 2 (site 2 is located inside the beryllium reflector around the core) (Sogbadji, Nyarko, & Akaho, 2011). The value of the epithermal flux shaping factor as well as the neutron fluxes obtained in the study were in good agreement with previous studies carried out at GHARR-1 and another MNSR facility. Thus it was concluded that there was no significant change in the neutron spectrum parameters after the addition of the beryllium reflector (Sogbadji et al., 2011).

A study was carried out by Baidoo et al in 2013 to characterize an irradiation site (Bsite2) of GHARR-1 so as to validate the K_0-IAEA software for neutron activation analysis. This was done using three flux monitors (gold, zirconium and iron). The characterization of the neutron flux parameters was done using the dual monitor cadmium ratio method and the bare multi monitor method employed by the K_0-IAEA software. Comparisons were made between results obtained from the K_0-IAEA software, the dual monitor cadmium ratio method and results of previous studies carried out at the GHARR-1 facility. All parameters except the fast neutron flux determined by the K_0-IAEA software and the dual monitor cadmium ratio method agreed very well within the uncertainty limit. The fast neutron flux could not be calculated by the K_0-IAEA software. The thermal to epithermal neutron flux ratio from the study compared well with a previous study carried out in 2002 (Akaho & Nyarko, 2002), (Baidoo et al., 2013). However the value of the epithermal neutron shaping factor was quite different from that of a study in 2006 (Ahmed et al., 2006), (Baidoo et al., 2013).

2.5 Conversion of HEU to LEU

In 2007 the Portuguese Research Reactor (RPI) was converted from HEU fuel (93.2 %) to LEU fuel (19.75 %). After the conversion a study was carried out to re-characterize the neutron spectrum at three irradiation sites (irradiation position for SIPRA, aerosols and biological samples) (Dung, Freitas, Santos, & Marques, 2010). This was accomplished by irradiating four flux monitors at the irradiation sites. The K_0-IAEA program was used to calculate the neutron spectrum parameters (thermal neutron flux, epithermal neutron spectrum shaping factor, thermal to epithermal neutron flux ratio, thermal to fast neutron flux ratio and neutron temperature). It was observed from the results of the study that the epithermal neutron shaping factor decreased by almost 50 % at the SIPRA irradiation site. At the biological samples site it increased by 33 % and changed to the negative at the aerosols site. Neutron temperature barely changed at all the irradiation sites. The thermal to epithermal neutron flux ratio decreased at the SIPRA, however, it slightly increased at the areosol and biological sites. The thermal to fast neutron flux ratio decreased at all the irradiation sites implying an increase in the fast neutron flux (Dung et al., 2010).

Between November, 2011 and January, 2012 the Dalat Nuclear Research reactor (DNRR) was fully converted from an HEU fuel core to an LEU fuel core (Dien et al., 2014). The neutron spectrum parameters (thermal neutron flux, epithermal neutron spectrum shaping factor, thermal to epithermal neutron flux ratio and fast neutron flux) were characterized at four irradiation sites (channels 7-1 and 13-2, thermal column and rotary rack). These were determined using flux monitors via the bare multi monitor method (Vu et al., 2014). Results from the study showed that generally the thermal neutron flux decreased at all irradiation sites except the thermal column. The increase in the thermal column was attributed to modifications made to it rather than the core conversion (Vu et al., 2014). The fast neutron flux at channel 7-1 and the rotary rack both increased slightly while the thermal to epithermal neutron flux decreased implying an increase in epithermal neutron flux. The absolute value of epithermal neutron shaping factor at these sites however increased.

After previous neutronics feasibility studies showed that the Nigeria Research Reactor-1 (NIRR-1) could be successfully converted from HEU to LEU fuel ($\sim 12.5\,\%$) core (Jonah, Ibrahim, Ajuji, & Onimisi, 2012), a study was carried out in 2012 to determine the impact of the HEU to LEU conversion of the neutron spectrum parameters at the inner and outer irradiation sites of the NIRR-1 facility. The MCNP5 code was used to determine the cadmium ratio of some flux monitors. Using the cadmium ratios determined and employing cadmium ratio for multi-monitor method, the thermal to epithermal neutron flux ratio and the epithermal neutron shaping factor were determined for the HEU and LEU core MCNP models for the NIRR-1. The results of the HEU core were compared to a previous experimental characterization study carried out after the commissioning of the NIRR-1. The results compared well with each other indicating the suitability of the MCNP5 code in determining neutron spectrum parameters. The results obtained for the proposed LEU fuel core were slightly lower than that of the HEU core. This was attributed to neutron spectrum hardening as a result of the increase in amount of ^{238}U in the LEU fuel (Jonah et al., 2012). Due to the small difference in the results of the neutron spectrum parameters of the HEU and LEU cores, it was concluded that the HEU to LEU will have minimal impact on the neutron spectrum parameters at the irradiation sites of the NIRR-1.

As part of a proposed core conversion programme for Syria's MNSR, the MCNP4C code was used for analysis of neutronic parameters as well as neutron fluxes (thermal, epithermal and fast) at two irradiation sites (Aldawanra, Khattab, & Saba, 2015). Using the F5 tally feature of the MCNP4C code, the neutron fluxes and their axial distribution at the irradiation sites were determined for both the existing HEU fuel core and the proposed LEU core. The results of the simulation showed that the axial neutron flux distribution for all three regions of the neutron spectrum followed similar patterns for both the HEU and LEU fuel cores. The neutron fluxes for the LEU fuel core were reported to be slightly lower than that of the HEU. This was attributed to spectrum hardening (Aldawanra et al., 2015).

A study at the DNRR was performed to calculate the difference between neutron flux characteristics at three irradiation sites (channels 1-4 and 7-1 and the neutron trap) using the MNCP code after full conversion of the reactor core. The parameters calculated were the thermal neutron flux, thermal to epithermal neutron flux ratio, epithermal neutron shaping factor and neutron temperature. The results for the LEU fuel core was compared with that of the HEU. The results indicated that, the thermal neutron flux was lower at all the channels for the LEU core. This was attributed to the increase in density atoms of the fissile material (Hung & Cuong, 2016). The thermal to epithermal neutron flux ratio at channel 1-4 and the neutron trap were slightly higher for the LEU indicating a softer epithermal neutron spectra. At channel 7-1 however, the epithermal neutron spectra was harder. The fast neutron flux increased at channels 1-4 and 7-1 while it decreased at the neutron trap. This decrease at the neutron trap was attributed to the replacement of twelve fuel pins with twelve beryllium blocks (Hung & Cuong, 2016). The neutron temperature decreased slightly at the neutron trap and channel 1-4 while it barely changed at channel 7-1.

CHAPTER 3

METHODOLOGY

This chapter describes the MCNP model used for this study. It elaborates on the changes made to the model per results from the zero power test experiments. Also, a description of how the neutron fluxes, flux distribution and neutron spectrum parameters were determined is presented in this chapter.

3.1 MCNP Model

The input deck used for this study was obtained from a study carried out in 2012 by Odoi et al. The input deck was modified in various ways to reflect the current state of the GHARR-1 LEU core. The changes made to the input deck are based on the results from the Zero Power Test Experiment carried out in China, some on site measurements of reactor components and information from the GHARR-1 safety analysis report (SAR). The components remodeled include fuel pins, irradiation channels, reactivity regulator rods and control rod. The remodeling of the fuel pin was to incorporate the helium gas gap between fuel meat and the upper end plug. Figure 3.1 compares the GHARR-1 HEU and LEU fuel pins

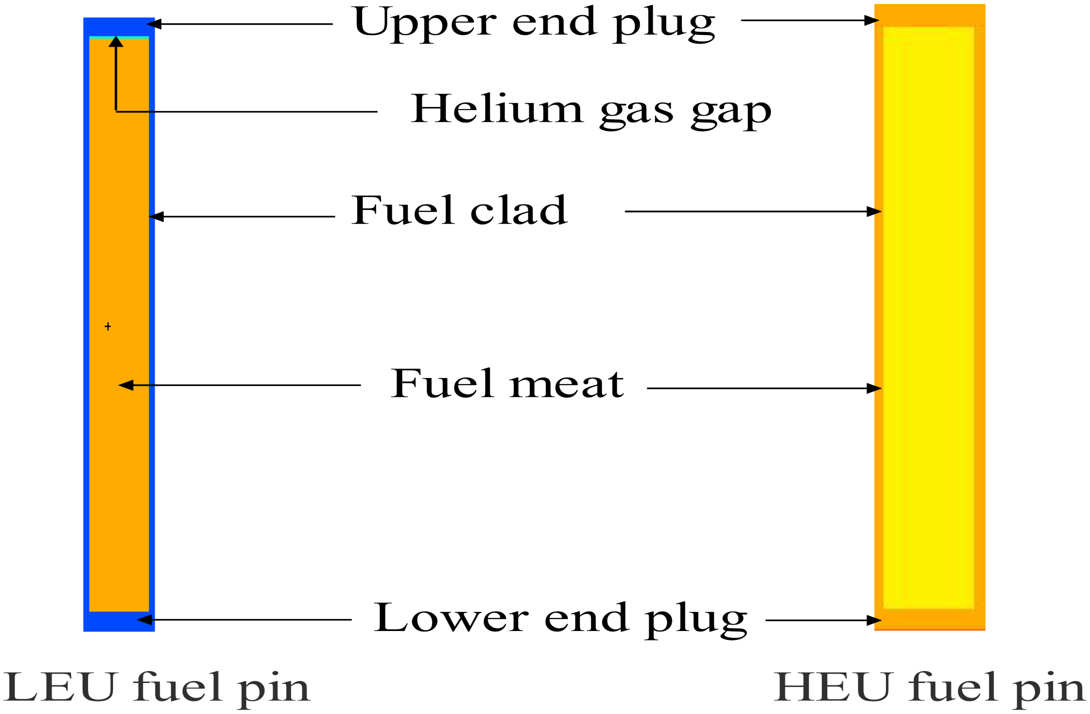

Figure 3.1: MCNP model of GHARR-1 LEU fuel pin

The inner and outer irradiation channels were remodeled to account for the inner thimble. In addition to the inner thimble, the support structure of the inner irradiation sites were also remodeled using a combination of planes, a cylinder and a trauncated cone. These changes are presented in Figure 3.2 and 3.3.

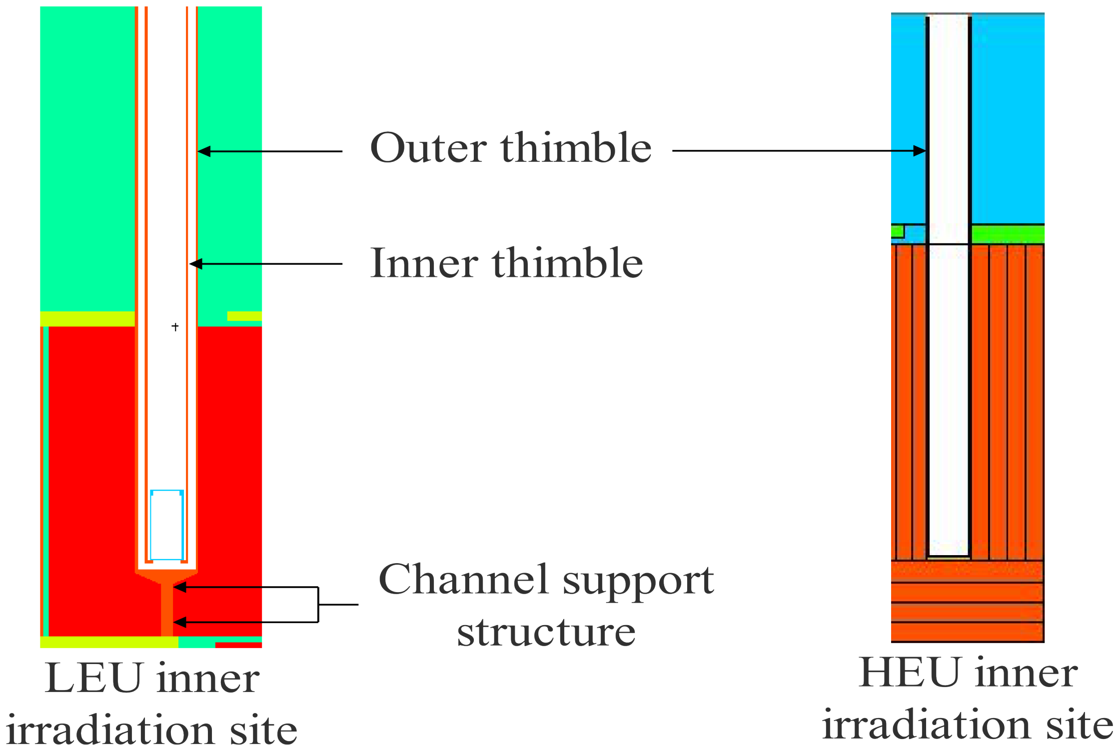

Figure 3.2: Cross sectional view of inner irradiation sites

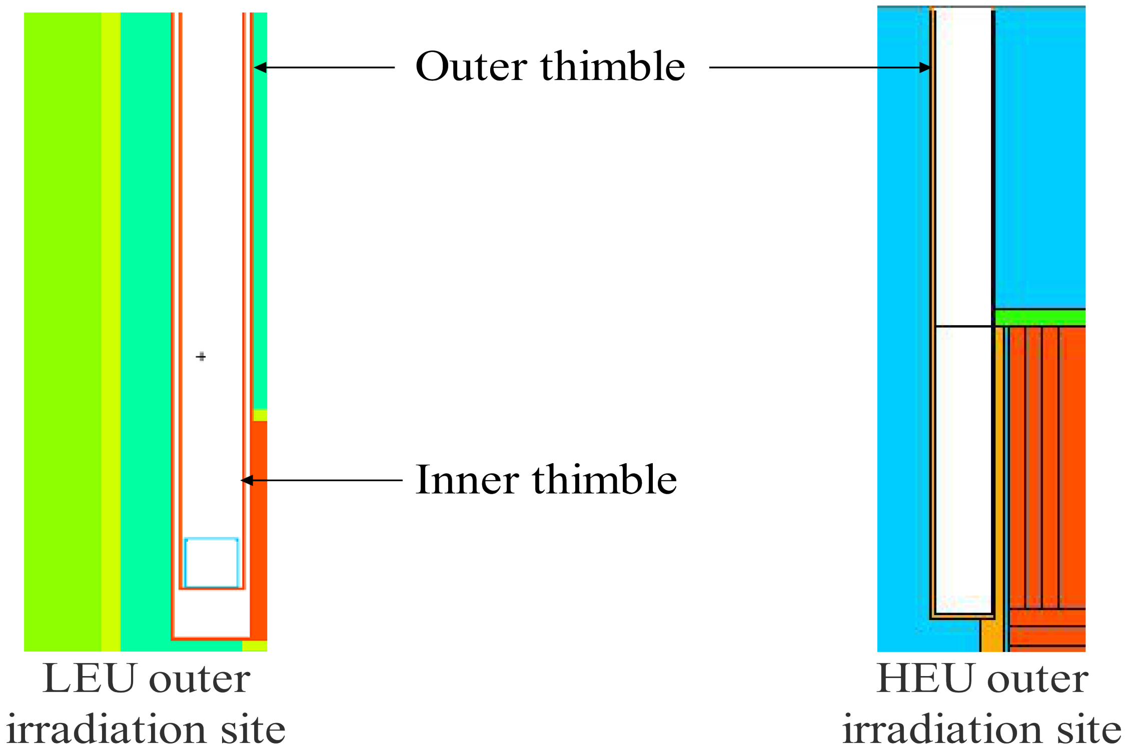

Figure 3.3: Cross sectional view of outer irradiation sites

The dimensions of the reactivity regulator rod was measured using vernier calipers and a tape measure. Based on these dimensions (outer diameter 3.65 cm,inner diameter 2.60 cm, height 35.0 cm, depth 31.5 cm, rod/string connection point 1.5 cm), the reactivity regulator rods were remodeled. Figure 3.4 presents the reactivity regulator rods use for this study and that of the previous HEU core model of the GHARR-1.

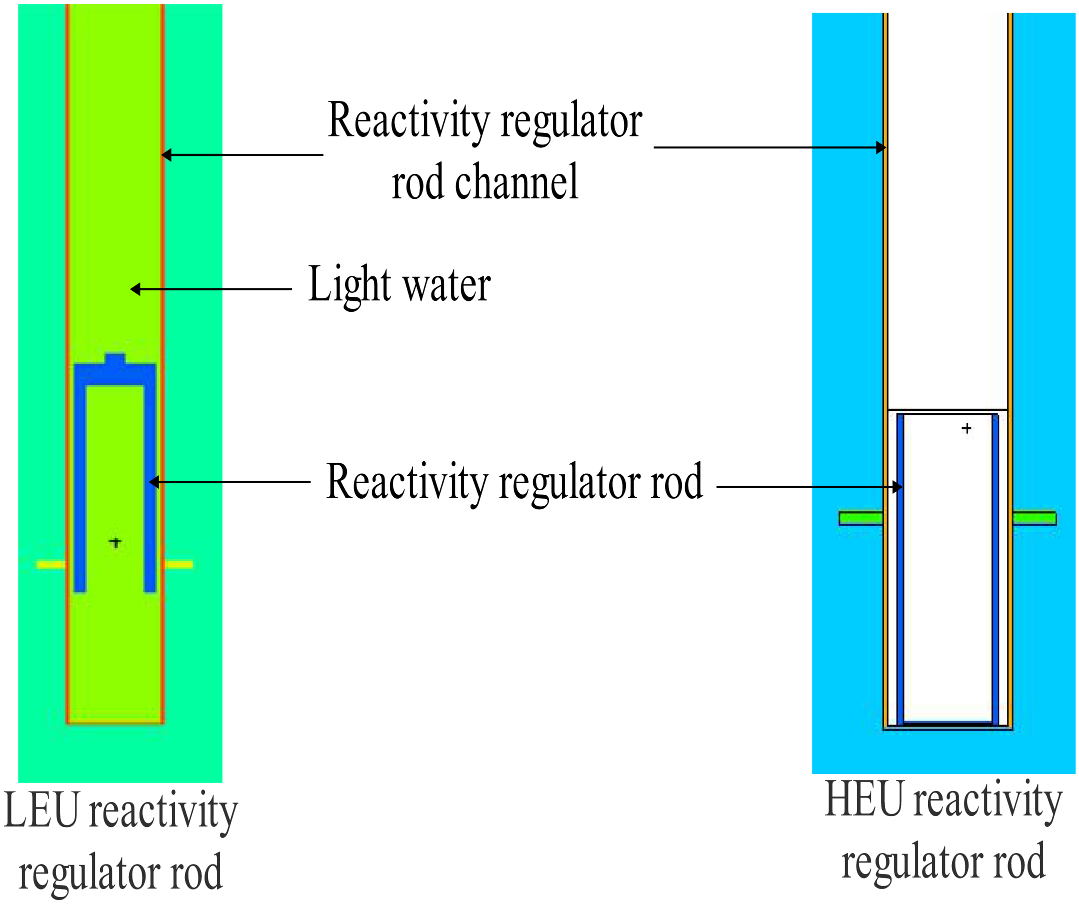

Figure 3.4: Reactivity regulator MCNP model

The composition of the control rod for the GHARR-1 LEU core differs from that of the HEU core. The cadmium absorber for the LEU control rod is clad between stainless steel and a central aluminium rod. This is illustrated in the figure 3.5.

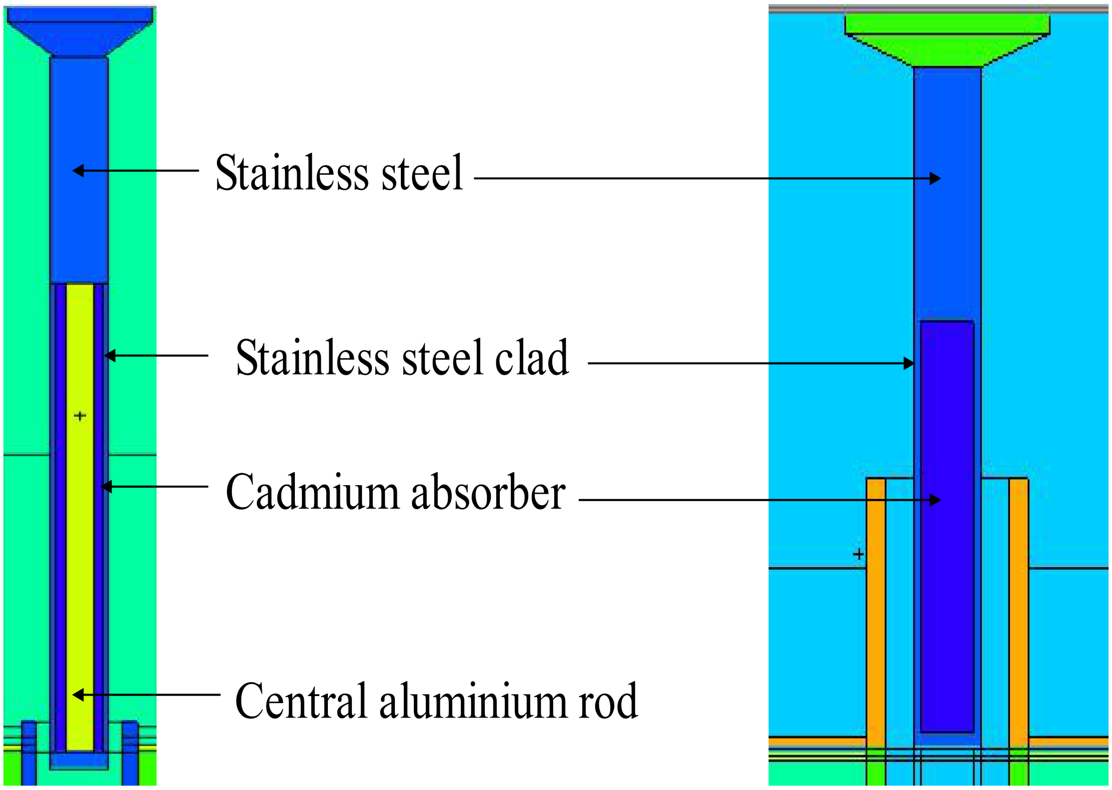

LEU control rod

HEU control rod

Figure 3.5: GHARR-1 LEU core control rod

In order to depict the arrangement of fuel pins in the fuel cage as presented in the zero power test experiment results, the arrangement of fuel pins on the first ring were changed. This was done by recalculating the coordinates of these pins. Furthermore, the number and positions of the dummy rods on the tenth fuel pin ring were modified. Figures 3.6 and 3.7 illustrate a two dimensional (2D) horizontal cross section and three dimensional (3D) view of GHARR-1 LEU core.

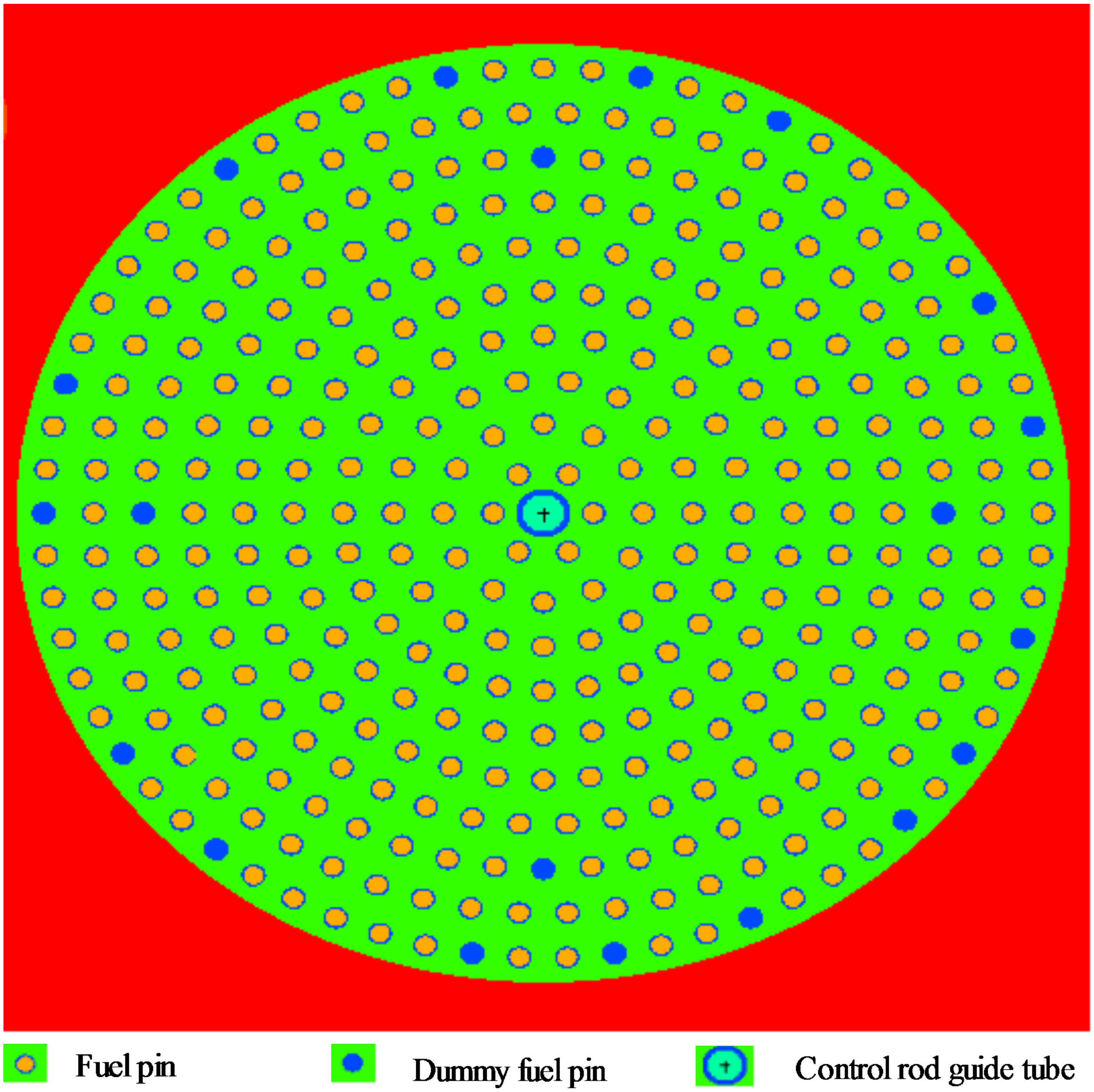

Figure 3.6: 2D view of the GHARR-1 LEU core

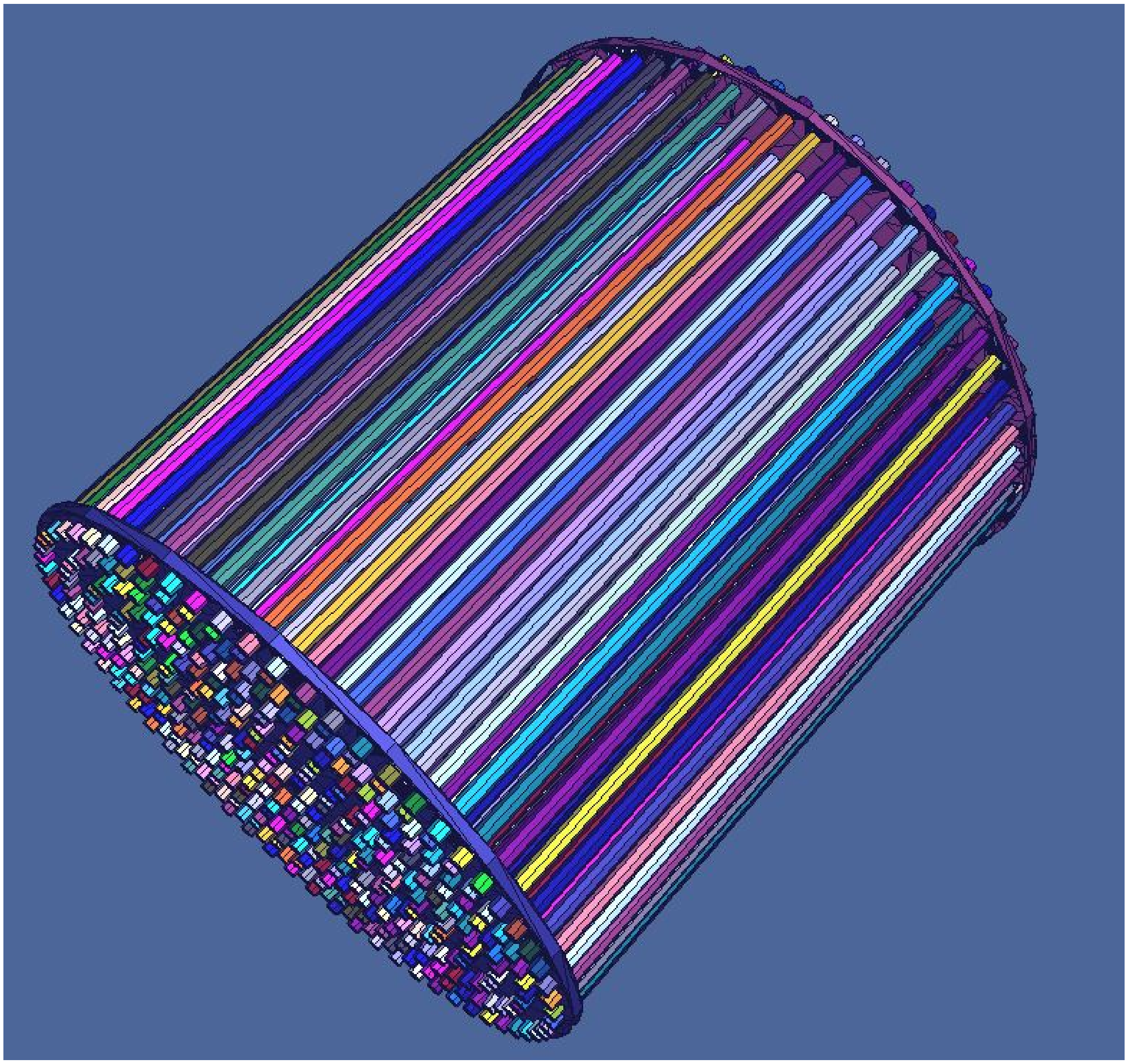

Figure 3.7: 3D view of the GHARR-1 MCNP core

Rabbit capsules were modeled both in dimension and composition into the various irradiation channels. Vernier calipers and a meter rule were used to obtain the dimensions of the rabbit capsules. Figure 3.9 shows the rabbit capsules at an inner and outer irradiation site. The input deck for remodeled components is presented in appendix B. Figures 3.8 and 3.9 show the horizontal and vertical cross sectional view of the GHARR-1 MCNP model.

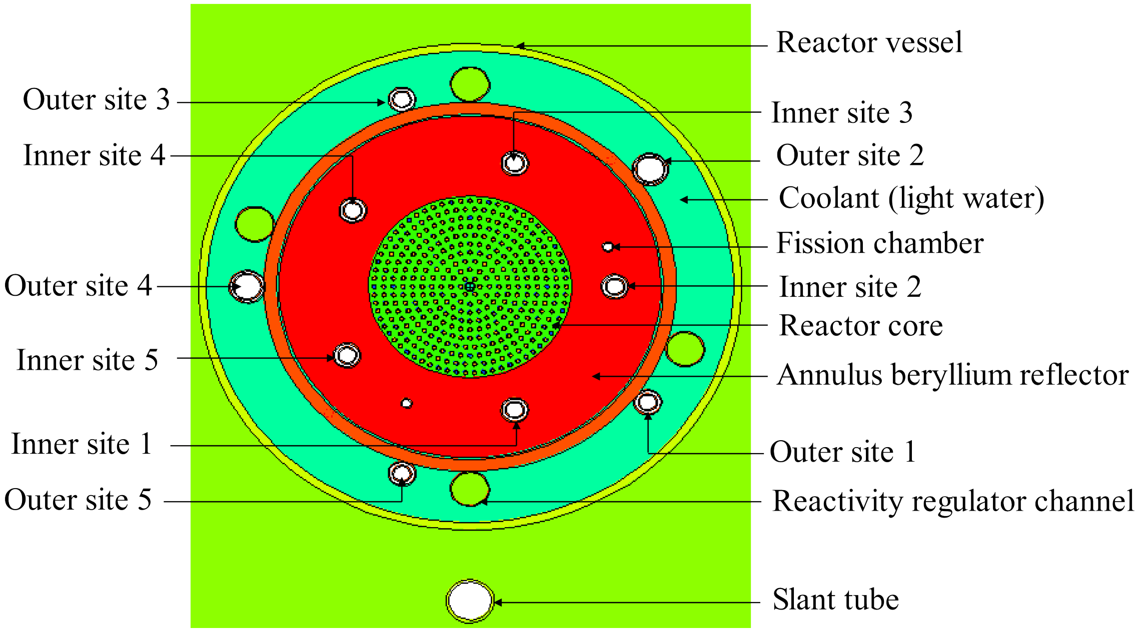

Figure 3.8: Horizontal cross sectional view of the GHARR-1 MCNP model

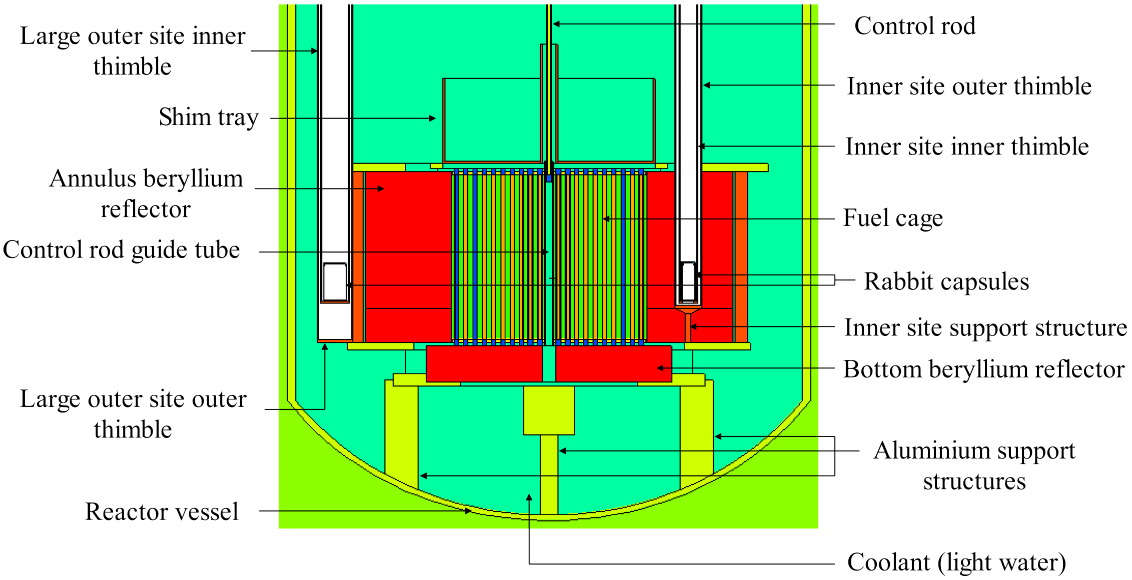

Figure 3.9: Horizontal cross sectional view of the GHARR-1 MCNP model

3.2 MCNP Calculations

The MCNP model described in the previous section was simulated using the MCNP5 code to determine the neutron fluxes and neutron spectrum parameters within rabbit capsules at the irradiation sites of the GHARR-1 facility. Employing MCNP's criticality card (KCODE), 600,000 particles per cycle were simulated for 530 cycles (first 30 cycles were skipped in order to achieve spatial neutron distribution before data to estimate desire results are gatherd) with an initial K_{eff} guess of 1.004. The ENDF-B/V and ENDF-B/VI cross section data libraries were employed in the modeling and simulation of the GHARR-1 MCNP model used for this study. Four input files were used for this study. First of all the LEU core model was simulated without rabbit capsules in the irradiation sites (LEU base deck). This was to determine the multiplication factor and hence reactivity of the model. The GHARR-1 HEU MCNP model of GHARR-1 was revised to account of the remodeled reactivity regulator rods, inner and outer irradiation channels and positions of first ring of fuel pins. This model (HEU base deck) was simulated to determine the multiplication factor and reactivity of the HEU core model. These aforementioned input files were modified by introducing rabbit capsules at the irradiation sites and addition of tally cards to determine neutron fluxes and reaction rates in some selected foils.

3.2.1 Neutron flux and flux distribution

The F4 tally card together with some auxiliary cards (FM and FS cards) were employed to determine the neutron fluxes and spectrum parameters. For each tally card, the neutron energy spectrum was divided into 12,208 energy bins. For the neutron flux distribution in the rabbit capsules, the F4 and FS cards were employed. The FS card was used to divide the volume of the rabbit capsule into six segments as shown in Figure 3.10.

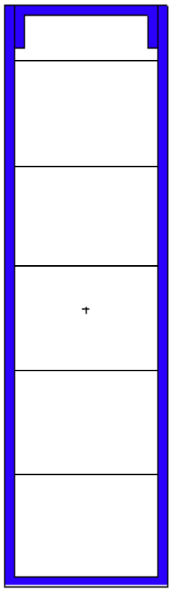

Figure 3.10: Segmentation of rabbit capsule for neutron flux distribution

The neutron fluxes at the various segments as well as the whole volume of the rabbit capsule was simulated. MCNP outputs neutron flux in per cm^2 ($^1/_{\text{cm}^2}$). To convert these fluxes into conventional neutron flux in neutrons per cm^2 per second (ncm^{-2}s^{-1}), a normalization factor (N_f) has to be established. Basically, this factor is dependent upon the reactor power and the number of neutrons per fission, $\overline{\nu}$. Equations (3.1) and (3.2) illustrate how this factor is calculated.

$$\left(\frac{1\,\text{joule/sec}}{\text{watt}}\right)\left(\frac{1\,\text{MeV}}{1.602\times10^{-13}\,\text{joules}}\right)\left(\frac{\text{fission}}{180\,\text{MeV}}\right) = 3.467\times10^{10}\,\text{fissions/watt sec} \tag{3.1}$$

$$N_f = 3.467\times10^{10}\text{fissions/watt sec}\times P\text{ watt}\times\overline{\nu}\text{ neutrons/fission} \tag{3.2}$$

P is the steady state reactor power. Simplifying equation (3.2),

$$N_f = 3.467 \times 10^{10} \times P \times \bar{\nu} \text{ neutrons/sec} \tag{3.3}$$

The Table (3.1) below shows the energy ranges used to determine the flux at each of the three neutron spectrum regions (thermal, epithermal and fast).

Table 3.1: Neutron spectrum energy ranges

Neutron spectrum region	Energy range
Thermal neutrons	0 - 0.55 eV
Epithermal neutrons	0.55 ev - 100 keV
Fast neutrons	100 keV - 20 MeV

The neutron flux for each of the regions was calculated as the sum of neutron fluxes at each energy within the energy range of the neutron spectrum. This is illustrated by equation (3.4).

$$\phi = \left(\sum_{E=i}^{k} \varphi(E) \right) N_f \tag{3.4}$$

Where ϕ is the convential neutron flux in ncm^{-2}s^{-1}, E is neutron energy, i and k are the lower and upper energy limits respectively for each energy range.

3.2.2 Neutron spectrum parameters

In order to determine the neutron spectrum parameters (α and f), the reaction rates of the various foils or flux monitors at each of the irradiation sites (using the FMn card together with the F4 card) were calculated. Based on the cadmium cut-off energy (0.55 eV), the cadmium ratio for the foils were determined using equation (3.5).

$$R_{Cd} = \frac{\sum_{E=i}^{k} \varphi(E)\sigma(E)}{\sum_{E=E_{Cd}}^{k} \varphi(E)\sigma(E)} \tag{3.5}$$

The table 3.2 shows the list of flux monitors, the respective reactions for which the reaction rates were determined as well as some constants associated with the flux monitors.

Table 3.2: Neutron spectrum energy ranges

Flux Monitor	Reaction(s)	$\overline{E}_r$(eV)	Q_o	F_{Cd}
Gold	$^{197}Au(n,\gamma)\,^{198}Au$	5.65	15.7	0.991
Zirconium	$^{94}Zr(n,\gamma)\,^{95}Zr$	6260	5.31	1

The reaction rates of the $^{197}Au(n,\gamma)\,^{198}Au$ and $^{94}Zr(n,\gamma)\,^{95}Zr$ reactions and hence their cadmium ratios were calculated for each of the irradiation sites. Based on the cadmium ratio method described in section 3.2.2.1, the thermal to epithermal neutron ratio and the epithermal neutron spectrum shaping factor were determined. Again, the cadmium-ratio for multi-monitor method described in section 3.2.2.2 was employed in determining the epithermal neutron spectrum shaping factor.

3.2.2.1 Cd-ratio method

From equation $I_0(\alpha) = 1\text{eV}^\alpha \int_{E_{Cd}}^{\infty} \frac{\sigma(E)dE}{E^{1+\alpha}}$, the resonance integral for the non-ideal $1/E^{1+\alpha}$ distribution is given by equation (3.6).

$$I_o(\alpha) = \left(\frac{I_o - 0.426\sigma_o}{\overline{E}_r^{-\alpha}} + \frac{0.426\sigma_o}{(2\alpha+1)(E_{Cd})^\alpha} \right) 1eV^\alpha \tag{3.6}$$

Where I_o is the resonance integral for the ideal $1/E$ distribution, $\overline{E}_r$ is the effective resonance energy. Multiplying both sides of equation (3.6) by $\frac{1}{\sigma_o}$, equation (3.6) becomes equation (3.7) as shown below.

$$Q_o(\alpha) = \left(\frac{Q_o - 0.426}{\overline{E}_r^{-\alpha}} + \frac{0.426}{(2\alpha+1)(E_{Cd})^\alpha} \right) \tag{3.7}$$

Q_o and $Q_o(\alpha)$ are the ratio of resonance integral for the ideal and non-ideal epithermal neutron flux distribution respectively to the thermal neutron flux cross section. For a nuclide irradiated with and without cadmium covered, the thermal to epithermal neutron flux ratio is given by equation (3.8).

$$f = (R_{Cd} - 1)(F_{Cd} Q_o(\alpha)) \tag{3.8}$$

F_{Cd} is the cadmium transmission factor. For any two nuclides which are irradiated together under the same conditions in a stable neutron flux, the value of f are approximately equal. Based on this α can be determined by iterating equation (3.9).

$$(R_{Cd,1} - 1)(F_{Cd,1} Q_{o,1}(\alpha)) = (R_{Cd,2} - 1)(F_{Cd,2} Q_{o,2}(\alpha)) \tag{3.9}$$

3.2.2.2 Cd-ratio for multi-monitor method

This method for determining α is applicable to reactors with a stable neutron flux with respect to time. The monitors used to determine α should have a $\sigma(v) \sim {}^{1}\!/_{v}$ dependence up to approximately 1.5 eV. With these conditions met, α can be obtained as the slope of the straight line from a plot of

$\mathrm{Log}\overline{\mathrm{E}}_{\mathrm{r,i}}$ against $\mathrm{Log}\dfrac{\overline{\mathrm{E}}_{\mathrm{r,i}}^{-\alpha}}{(\mathrm{F}_{\mathrm{Cd,i}}\mathrm{R}_{\mathrm{Cd,i}}-1)\mathrm{Q}_{\mathrm{o,i}}(\alpha)}$, for i=1,2,...,N.

Alternatively, α can be determined by solving the equation 3.10 below,

$$\alpha+\frac{\sum_{i}^{N}\left\{\left(Log\overline{E}_{r,i}-\frac{\sum_{i}^{N}Log\overline{E}_{r,i}}{N}\right)\left(Log\frac{\overline{E}_{r,i}^{-\alpha}}{(F_{Cd,i}R_{Cd,i}-1)Q_{o,i}(\alpha)}-\frac{\sum_{i}^{N}Log\frac{\overline{E}_{r,i}^{-\alpha}}{(F_{Cd,i}R_{Cd,i}-1)Q_{o,i}(\alpha)}}{N}\right)\right\}}{\sum_{i}^{N}\left(Log\overline{E}_{r,i}-\frac{\sum_{i}^{N}Log\overline{E}_{r,i}}{N}\right)^{2}}=0 \tag{3.10}$$

$\mathrm{F}_{\mathrm{Cd,i}}$ is cadmium transmission factor for ith flux monitor, $\mathrm{R}_{\mathrm{Cd,i}}$ is cadmium ratio for ith flux monitor, $\mathrm{E}_{\mathrm{r,i}}$ is effective resonance energy for ith flux monitor and α the epithermal neutron shaping factor.

CHAPTER 4

RESULTS AND DISCUSSION

This chapter provides and discusses the results obtained from the study and how it compares with previous studies carried out on the GHARR-1 HEU core and other research reactors.

4.1 Criticality results

Using the criticality calculation feature of MCNP5 code, the K_{eff} and reactivity of the models simulated are presented in Table 4.1.

Table 4.1: K_{eff} and Reactivity of GHARR-1 HEU and LEU models

Model	K_{eff}	Reactivity
HEU base deck	1.00398 ± 0.00005	3.96 ± 0.05mk
HEU	1.00405 ± 0.00005	4.03 ± 0.05mk
LEU base deck	1.00405 ± 0.00005	4.03 ± 0.05mk
LEU	1.00410 ± 0.00005	4.08 ± 0.05mk

The reactivity of the HEU base deck is in good agreement with the experimentally determined value (3.99 mk) recorded at the commissioning of GHARR-1 with HEU core in 1995 (Gbadago et al., 2011). Considering the uncertainty margins, the reactivity of the LEU base deck is within the accepted limits for operation of an MNSR (3.5 mk - 4.0 mk). The models with rabbit capsules at the irradiation channels recorded slightly higher reactivities. This can be attributed to the material compositon of the rabbit capsule, polyethylene. Polyethylene is mainly made of hydrogen and carbon which have high neutron scattering cross sections.

4.2 Neutron spectrum parameters

Tables 4.2 and 4.3 provide results of the cadmium ratio and resonance integral to thermal neutron cross section ratio of ^{197}Au and ^{94}Zr flux monitors and the neutron spectrum parameters respectively at the inner irradiation sites of the GHARR-1 with HEU core using the MCNP5 code.

Table 4.2: Cadmium ratios and non-ideal resonance integral to thermal neutron cross section for flux monitors at inner irradiation sites of HEU core

	Site 1	Site 2	Site 3	Site 4	Site 5	Ref
R_{Cd}						
^{197}Au	2.02±0.05	2±0.05	1.97±0.05	2.01±0.05	1.97±0.05	This work
^{94}Zr	2.67±0.09	2.57±0.09	2.54±0.09	2.52±0.09	2.53±0.09	This work
^{197}Au	2.36				2.10	(Akaho & Nyarko, 2002)
^{94}Zr	2.85				2.68	(Akaho & Nyarko, 2002)
$Q_o(\alpha)$						
^{197}Au	18.63±0.14	18.87±0.15	18.82±0.15	19.08±0.16	18.83±0.15	This work
^{94}Zr	11.35±0.37	12.07±0.37	11.93±0.37	12.72±0.37	11.95±0.37	This work
^{197}Au	18.79				18.92	(Akaho & Nyarko, 2002)
^{94}Zr	12.62				12.40	(Akaho & Nyarko, 2002)
$Q_o(\alpha)^*$						
^{197}Au	18.76±0.15	18.91±0.16	18.86±0.16	19.10±0.17	18.90±0.16	This work
^{94}Zr	12.75±0.36	13.53±0.36	13.36±0.36	14.23±0.37	13.49±0.36	This work

Ref: Reference

$Q_o(\alpha)$: Non ideal resonance integral to thermal neutron cross section using cadmium ratio method

$Q_o(\alpha)^*$: Non ideal resonance integral to thermal neutron cross section using cadmium ratio for multi-monitor method

Table 4.3: Neutron spectrum parameters at inner irradiation sites for HEU core

	f	α	α^*	Ref
Site 1	18.94±0.51	-0.097±0.004	-0.107±0.004	This work
	18.80	-0.104		(Akaho & Nyarko, 2002)
Site 2	18.94±0.52	-0.104±0.004	-0.114±0.004	This work
Site 3	18.34±0.51	-0.103±0.004	-0.112±0.004	This work
Site 4	19.29±0.54	-0.11±0.004	-0.122±0.004	This work
Site 5	18.27±0.51	-0.103±0.004	-0.114±0.004	This work
	17.28	-0.107		(Akaho & Nyarko, 2002)

Ref: Reference
α: Epithermal shaping factor using Cd-ratio method.
α^*: Epithermal shaping factor using Cd-ratio for multi-monitor method.

The cadmium ratio determined from this study for the two flux monitors used even though compared very well to that of the previous experimental work was slightly lower. This can be attributed to the fact that fuel burn-up was not considered in this study. However, the results from the previous study was carried out eight years after commissioning of the GHARR-1 and hence there was a fair amount of fuel burn-up. In a similar manner, results of the thermal to epithermal neutron flux ratio from this study compared well to that of the previous study with maximum deviation below 6 %. Same can be said of the results of the epithermal neutron shaping factor. The results of the two different methods used to determine the epithermal neutron shaping factor compared well with each other and with the results of the previous experimental work carried out by Akaho and Nyarko (Akaho & Nyarko, 2002).

Tables 4.4 and 4.5 provide results of the cadmium ratio and resonance integral to thermal neutron cross section ratio of ^{197}Au and ^{94}Zr flux monitors and the neutron spectrum parameters respectively at the outer irradiation sites.

Table 4.4: Cadmium ratios and non-ideal resonance integral to thermal neutron cross section for flux monitors at inner irradiation sites of HEU core

	Site 1	Site 2	Site 3	Site 4	Site 5	Ref
R_{Cd}						
^{197}Au	4.05±0.27	3.75±0.18	3.81±0.24	4.11±0.19	3.91±0.18	This work
^{94}Zr	8.54±0.76	8.76±0.81	8.03±0.71	8.73±0.73	8.2±0.76	This work
^{197}Au	3.92					(Akaho & Nyarko, 2002)
^{94}Zr	8.76					(Akaho & Nyarko, 2002)
$Q_o(\alpha)$						
^{197}Au	16.61±0.06	16.61±0.05	16.62±0.05	16.44±0.06	16.59±0.06	This work
^{94}Zr	6.76±0.22	6.58±0.2	6.65±0.21	6.71±0.22	6.75±0.22	This work
^{197}Au	16.42					(Akaho & Nyarko, 2002)
^{94}Zr	6.76					(Akaho & Nyarko, 2002)
$Q_o(\alpha)$*						
^{197}Au	16.55±0.05	16.40±0.04	16.49±0.05	16.52±0.05	16.55±0.05	This work
^{94}Zr	6.88±0.20	6.58±0.17	6.75±0.19	6.82±0.19	6.87±0.20	This work

Ref: Reference

$Q_o(\alpha)$: Non ideal resonance integral to thermal neutron cross section using cadmium ratio method

$Q_o(\alpha)$*: Non ideal resonance integral to thermal neutron cross section using cadmium ratio for multi-monitor method

Table 4.5: Neutron spectrum parameters at inner irradiation sites for HEU core

	f	α	α*	Ref
Site 1	50.94±0.86	-0.035±0.003	-0.032±0.003	This work
	49.00	-0.026		(Akaho & Nyarko, 2002)
Site 2	45.59±0.49	-0.031±0.005	-0.027±0.004	This work
Site 3	46.78±0.47	-0.033±0.005	-0.030±0.005	This work
Site 4	51.87±0.51	-0.034±0.005	-0.031±0.004	This work
Site 5	48.59±0.5	-0.035±0.005	-0.032±0.004	This work

Ref: Reference
α: Epithermal shaping factor using Cd-ratio method.
α*: Epithermal shaping factor using Cd-ratio for multi-monitor method.

Just as with the inner irradiation sites, cadmium ratio for the flux monitors are generally lower (up to 3 %) than that of the previous study for the outer irradiation sites. However, these results are in good agreement with each other. Same can be said of the thermal to epithermal neutron flux ratio and the epithermal neutron shaping factor. These results prove the suitability of the MCNP5 code for neutron spectrum parameter characterization.

Tables 4.6 and 4.7 provide results of the cadmium ratio and resonance integral to thermal neutron cross section ratio of ^{197}Au and ^{94}Zr flux monitors and the neutron spectrum parameters respectively at the inner irradiation sites of the GHARR-1 with LEU core using the MCNP5.

Table 4.6: Cadmium ratios and non-ideal resonance integral to thermal neutron cross section for flux monitors at inner irradiation sites of LEU core

	Site 1	Site 2	Site 3	Site 4	Site 5
R_{Cd}					
^{197}Au	1.97±0.05	1.96±0.05	1.91±0.05	1.98±0.05	1.96±0.05
^{94}Zr	2.67±0.10	2.59±0.11	2.53±0.11	2.57±0.10	2.55±0.10
$Q_o(\alpha)$					
^{197}Au	18.39±0.13	18.58±0.14	18.51±0.13	18.75±0.14	18.71±0.14
^{94}Zr	10.68±0.36	11.22±0.37	11.01±0.36	11.70±0.37	11.59±0.37
$Q_o(\alpha)^*$					
^{197}Au	18.42±0.14	18.63±0.15	18.55±0.15	18.81±0.16	18.77±0.16
^{94}Zr	11.80±0.36	12.53±0.36	12.24±0.36	13.17±0.36	13.02±0.36

Table 4.7: Neutron spectrum parameters at inner irradiation sites for LEU core

	f	α	α^*
Site 1	17.84±0.48	-0.09±0.005	-0.098±0.004
Site 2	17.84±0.49	-0.097±0.005	-0.105±0.004
Site 3	16.84±0.47	-0.093±0.005	-0.102±0.005
Site 4	18.37±0.51	-0.1±0.005	-0.111±0.004
Site 5	17.96±0.5	-0.099±0.005	-0.109±0.004

α: Epithermal shaping factor using Cd-ratio method.
α^*: Epithermal shaping factor using Cd-ratio for multi-monitor method.

Comparison of the cadmium ratios of the two flux monitors at the inner sites of the LEU core to that of the HEU core generally indicate a slight decrease (below 5 %) for the LEU core. For thermal to epithermal neutron flux ratio that of the LEU core was slightly lower than that of the HEU with deviations between 4 % and 8 %. This is attributed to the increase in the inventory of ^{238}U in the LEU core as compared to the HEU core. The absolute values of the epithermal neutron shaping factor just like the other parameters is lower (up to 10 % lower) in the case of the LEU core as compared to the HEU core. Tables 4.8 and 4.9 provide results of the cadmium ratio and resonance integral to thermal neutron cross section ratio of ^{197}Au and ^{94}Zr flux monitors and the neutron spectrum parameters respectively of the outer irradiation sites .

Table 4.8: Cadmium ratios and non-ideal resonance integral to thermal neutron cross section for flux monitors at inner irradiation sites of LEU core

	Site 1	Site 2	Site 3	Site 4	Site 5
R_{Cd}					
^{197}Au	3.91±0.10	3.69±0.11	3.75±0.10	3.68±0.13	3.57±0.12
^{94}Zr	8.34±0.42	7.78±0.46	7.93±0.38	8.03±0.50	7.52±0.51
$Q_o(\alpha)$					
^{197}Au	16.61±0.05	16.61±0.05	16.62±0.05	16.44±0.04	16.59±0.05
^{94}Zr	6.59±0.21	6.59±0.21	6.59±0.21	6.27±0.18	6.57±0.20
$Q_o(\alpha)^*$					
^{197}Au	16.44±0.05	16.45±0.05	16.45±0.05	16.24±0.03	16.41±0.05
^{94}Zr	6.67±0.19	6.68±0.19	6.68±0.19	6.27±0.14	6.60±0.18

Table 4.9: Neutron spectrum parameters at inner irradiation sites for LEU core

	f	α	α^*
Site 1	48.34±0.86	-0.032±0.003	-0.029±0.003
Site 2	44.69±0.81	-0.032±0.003	-0.029±0.003
Site 3	45.69±0.82	-0.032±0.003	-0.029±0.003
Site 4	44.05±0.79	-0.026±0.003	-0.021±0.003
Site 5	42.63±0.78	-0.031±0.003	-0.028±0.003

α: Epithermal shaping factor using Cd-ratio method.
α^*: Epithermal shaping factor using Cd-ratio for multi-monitor method.

At the outer irradiation sites, a trend of results similar to the inner irradiation sites were obtained. All parameters except the absolute value of the epithermal neutron shaping factor were over two times that of the inner irradiation sites. These are attributed to the high level of thermalization at the outer irradiation sites. From the results of both the

GHARR-1 LEU and HEU core irradiation sites, there is a clear indication of a hardened neutron spectrum due to the negative value of the epithermal neutron shaping factor. The epithermal neutron distribution at the inner irradiation sites tend to deviate more from the ideal $^{1}/_{E}$ distribution due to the higher absolute value of the epithermal neutron shaping factor at the inner irradiation sites compared to that of the outer irradiation sites. However, results from the LEU core irradiation sites indicate a harder neutron spectrum. This can be attributed to the increase in amount of U^{238} in the LEU fuel meat.

Uncertainties associated with the various neutron spectrum parameters were calculated from equations presented in Appendix C.

4.3 Neutron flux

In this section, the results of the neutron flux within the whole volume of the rabbit capsules at the irradiation sites are presented. Each figure in this section provides and compares the neutron flux within a particular energy range at half and full power for both the GHARR-1 HEU and LEU models. From Figure 4.1, there is a clear indication that the thermal neutron flux at both half and full power for the HEU and LEU cores are comparable. Generally however, the LEU thermal flux is up to 7 % higher than that of the HEU thermal flux at the inner irradiation sites. This is solely due to the higher thermal power for the LEU core. From Figure 4.2 and 4.3, same can be said of the epithermal aand fast energy regions with increase in flux up to 10 % and 7 % respectively. Appendix D presents data used for the barchart plots in this section.

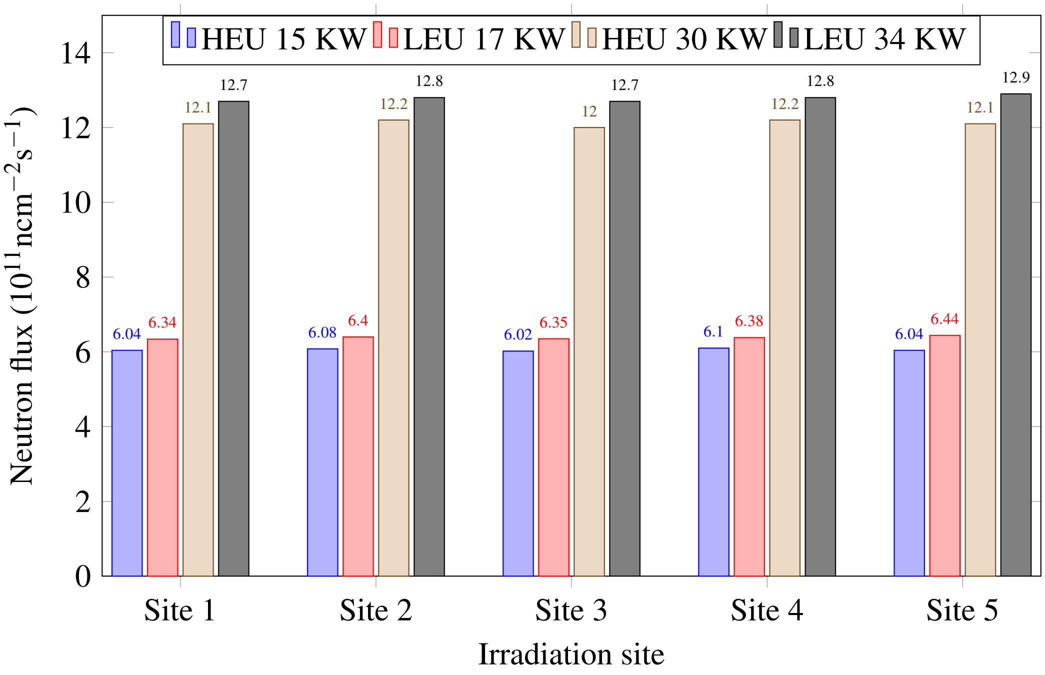

Figure 4.1: Thermal neutron flux at inner irradiation sites for GHARR-1 LEU and HEU cores at Half and Full Power

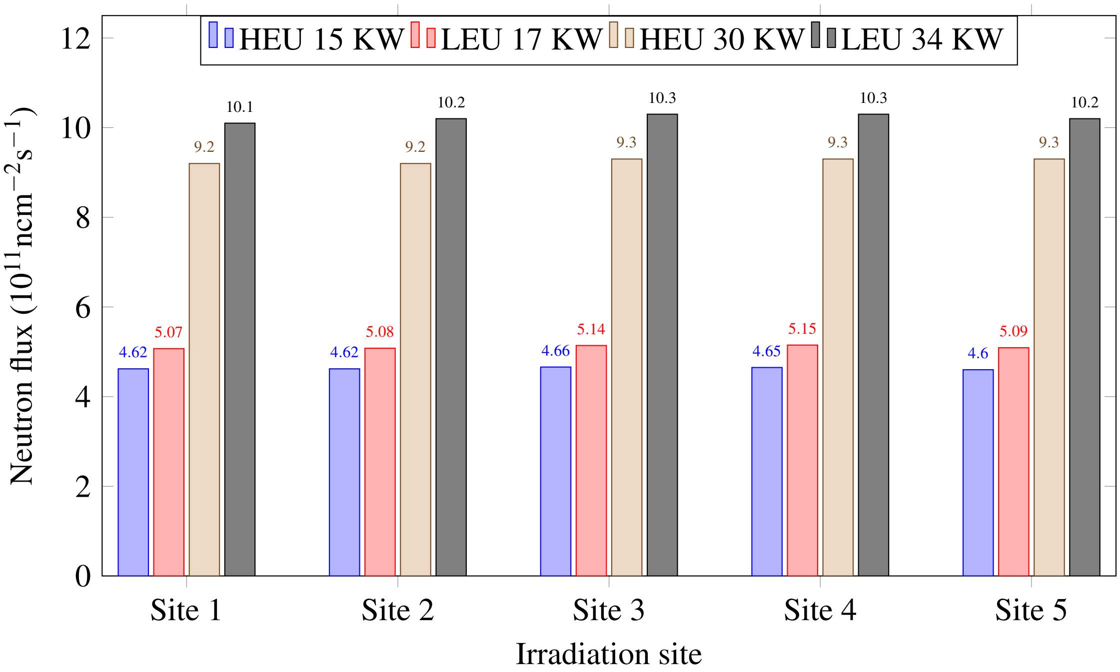

Figure 4.2: Epithermal neutron flux at inner irradiation sites for GHARR-1 LEU and HEU cores at Half and Full Power

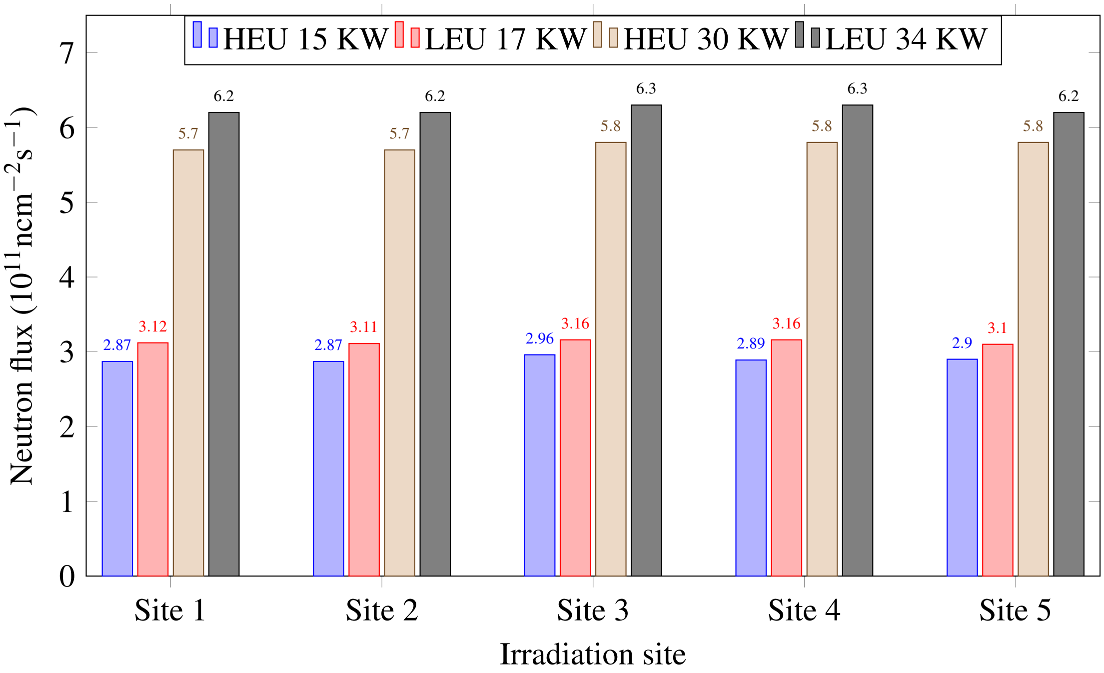

Figure 4.3: Fast neutron flux at inner irradiation sites for GHARR-1 LEU and HEU cores at Half and Full Power

From Figure 4.4, 4.5 and 4.6 it is observed that the neutron fluxes in all three energy regions are higher for the LEU core compared to the HEU core. For the thermal and epithermal regions, neutron flux for the LEU core was up to 15 % higher than that of the HEU core. That for the fast energy region was up to 8 % higher for the LEU core.

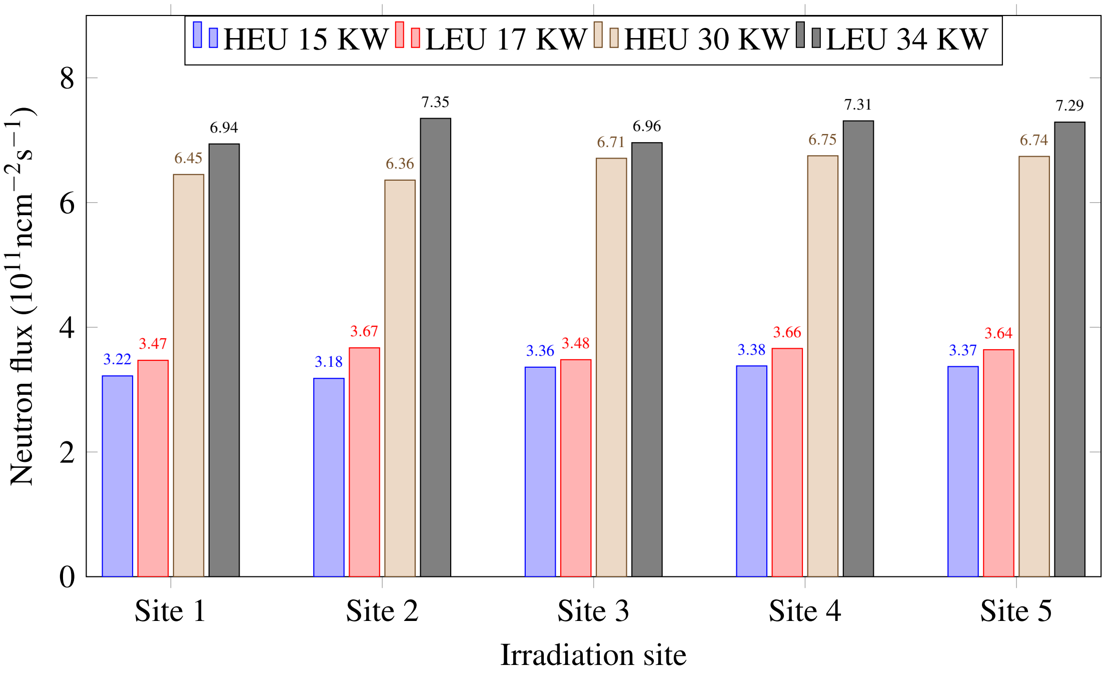

Figure 4.4: Thermal neutron flux at outer irradiation sites for GHARR-1 LEU and HEU cores at Half and Full Power

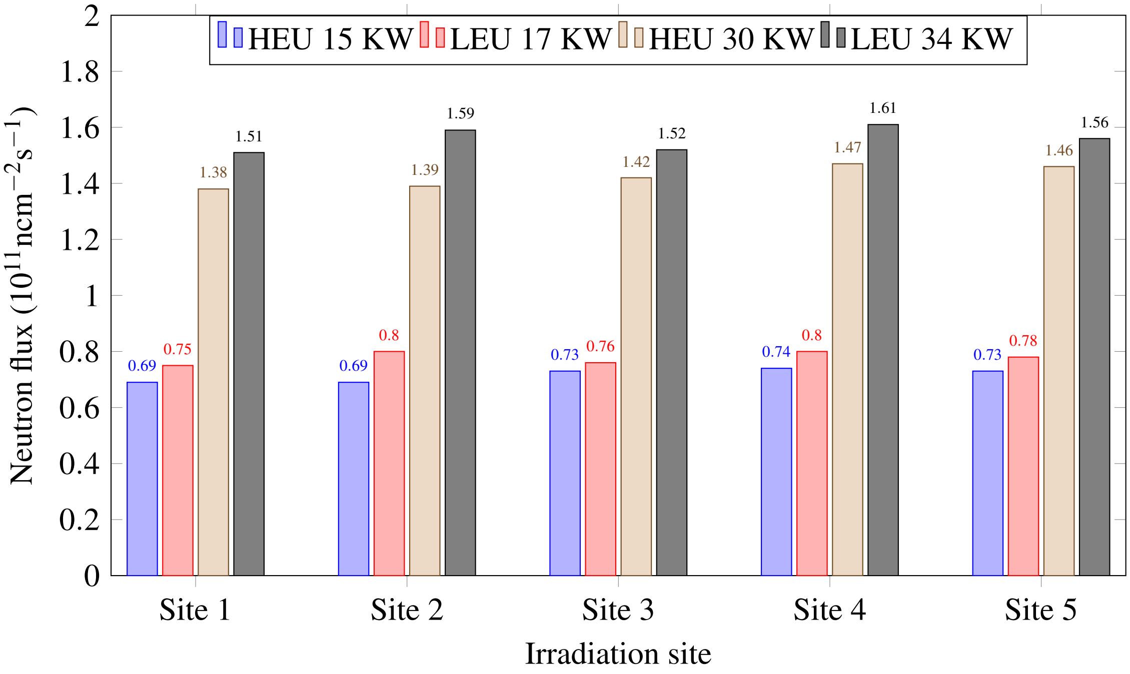

Figure 4.5: Epithermal neutron flux at outer irradiation sites for GHARR-1 LEU and HEU cores at Half and Full Power

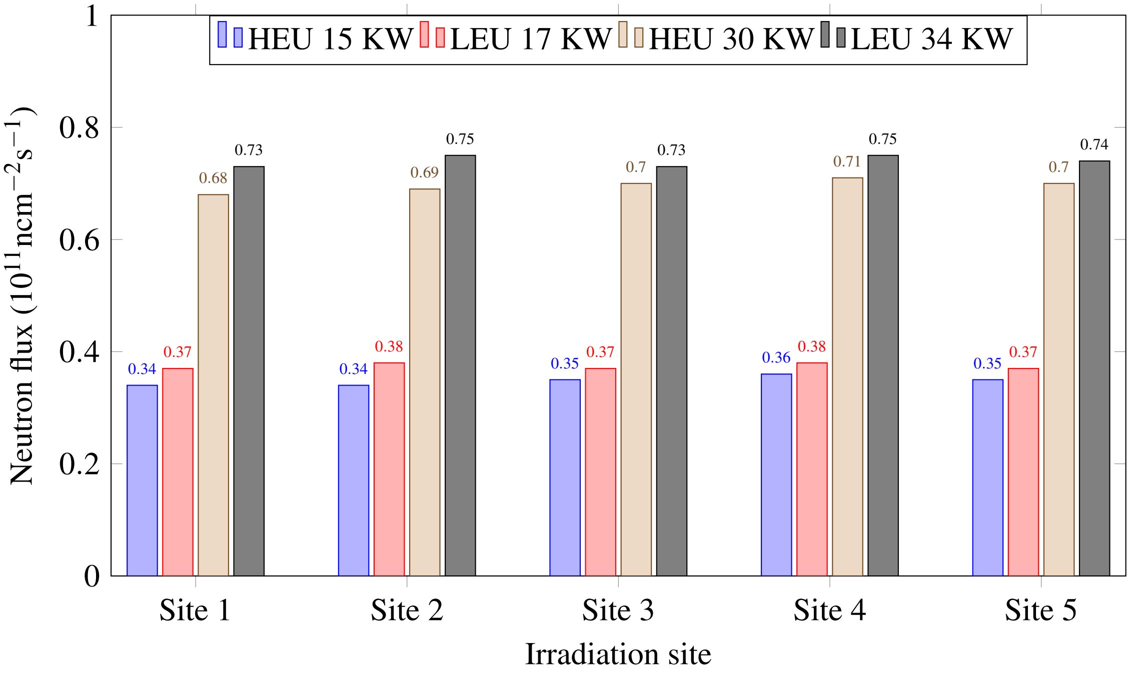

Figure 4.6: Fast neutron flux at outer irradiation sites for GHARR-1 LEU and HEU cores at Half and Full Power

4.4 Neutron flux distributions

This section provides a comparison between the neutron flux distribution within the irradiation sites of the GHARR-1 HEU and LEU models. Figures 4.7 to 4.16 illustrates neutron flux distribution at half power and full power for the inner irradiation sites. Appendix E presents data used for the flux distribution plots in this section.

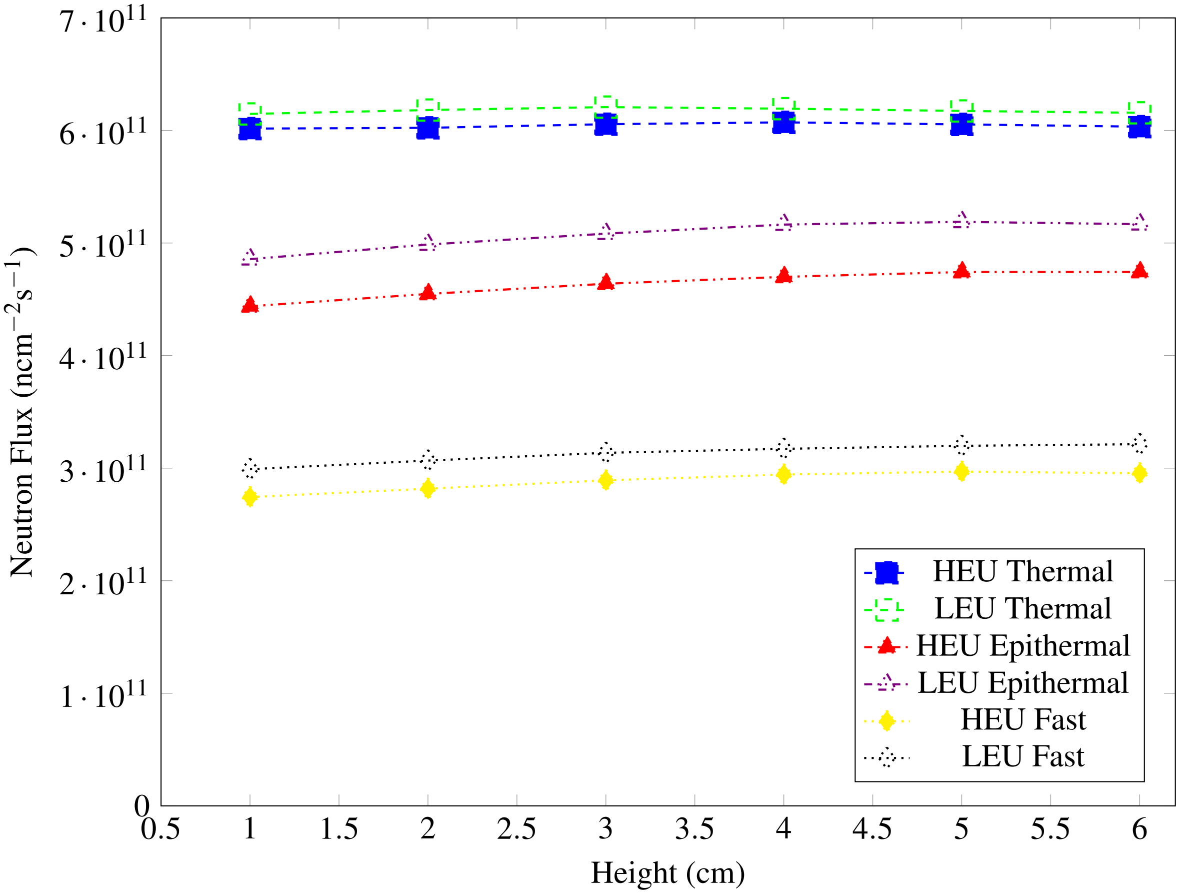

Figure 4.7: Comparison of LEU and HEU neutron flux distribution at Inner site 1 at Half Power

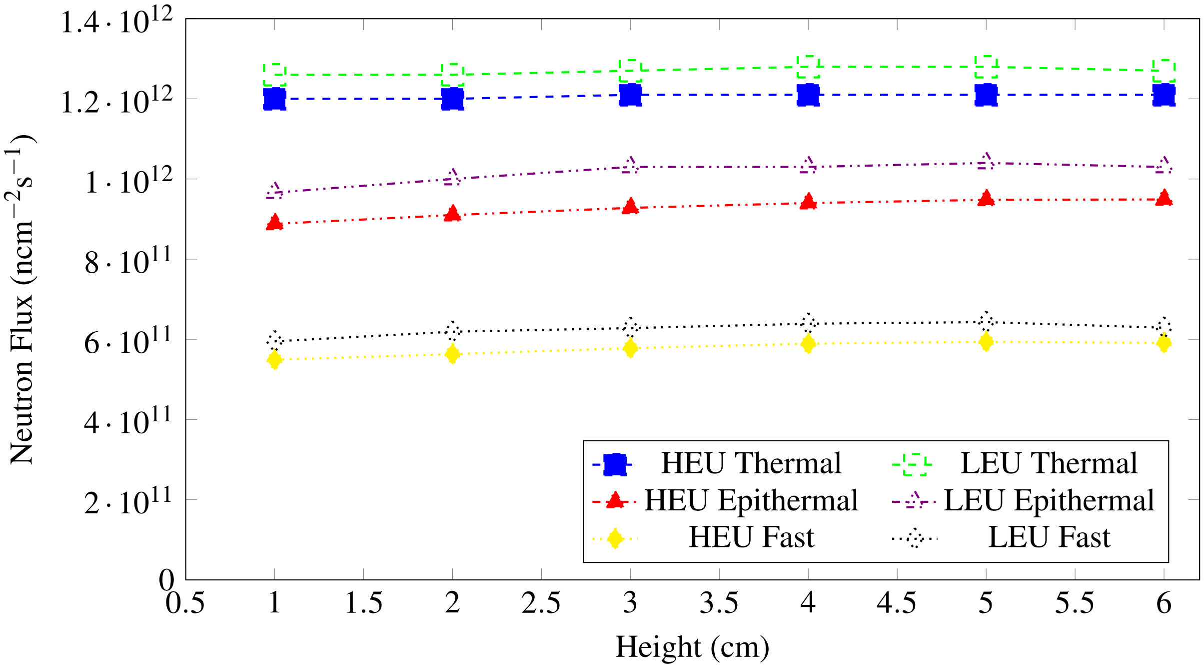

Figure 4.8: Comparison of LEU and HEU neutron flux distribution at Inner site 1 at Full Power

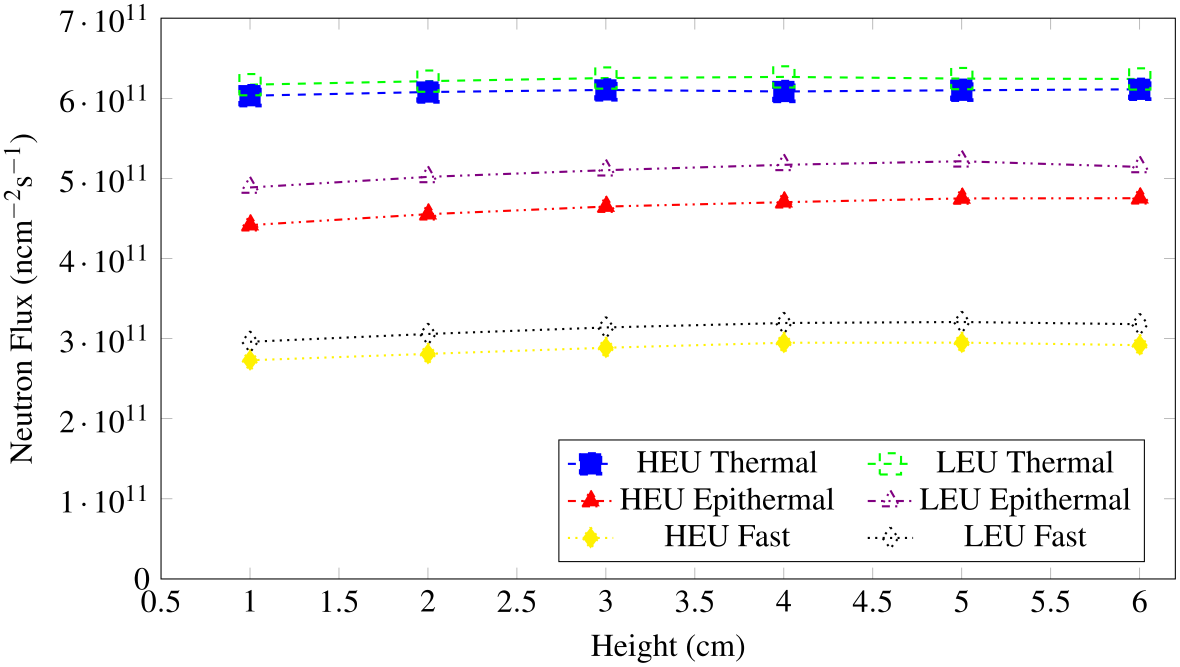

Figure 4.9: Comparison of LEU and HEU neutron flux distribution at Inner site 2 at Half Power

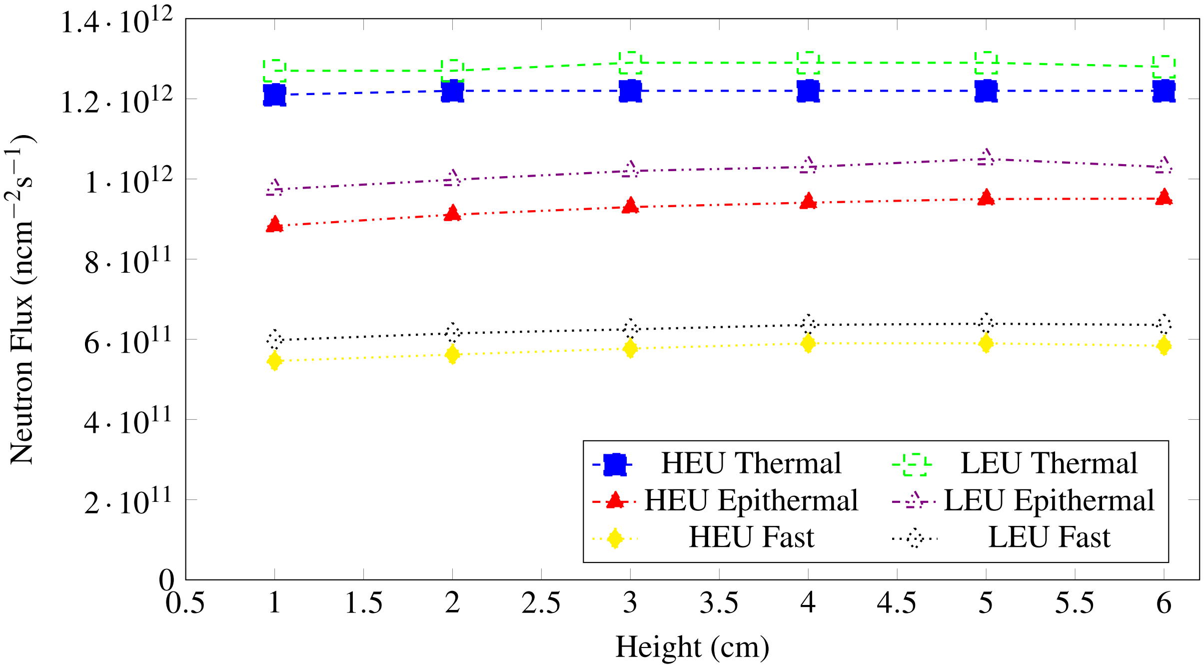

Figure 4.10: Comparison of LEU and HEU neutron flux distribution at Inner site 2 at Full Power

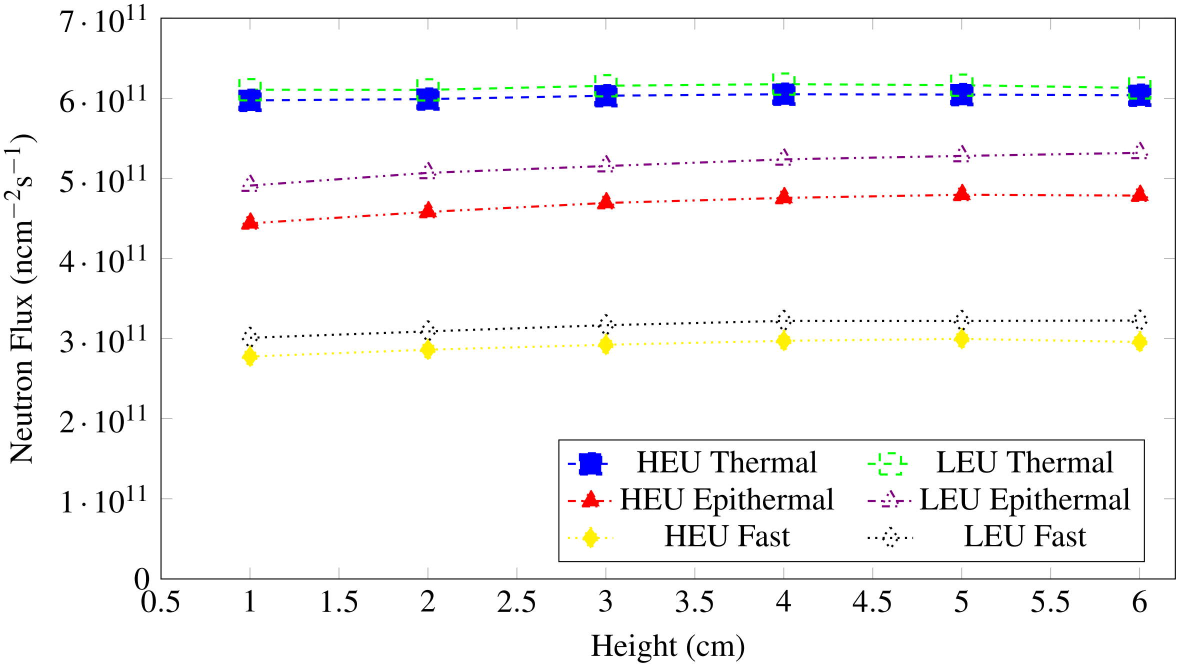

Figure 4.11: Comparison of LEU and HEU neutron flux distribution at Inner site 3 at Half Power

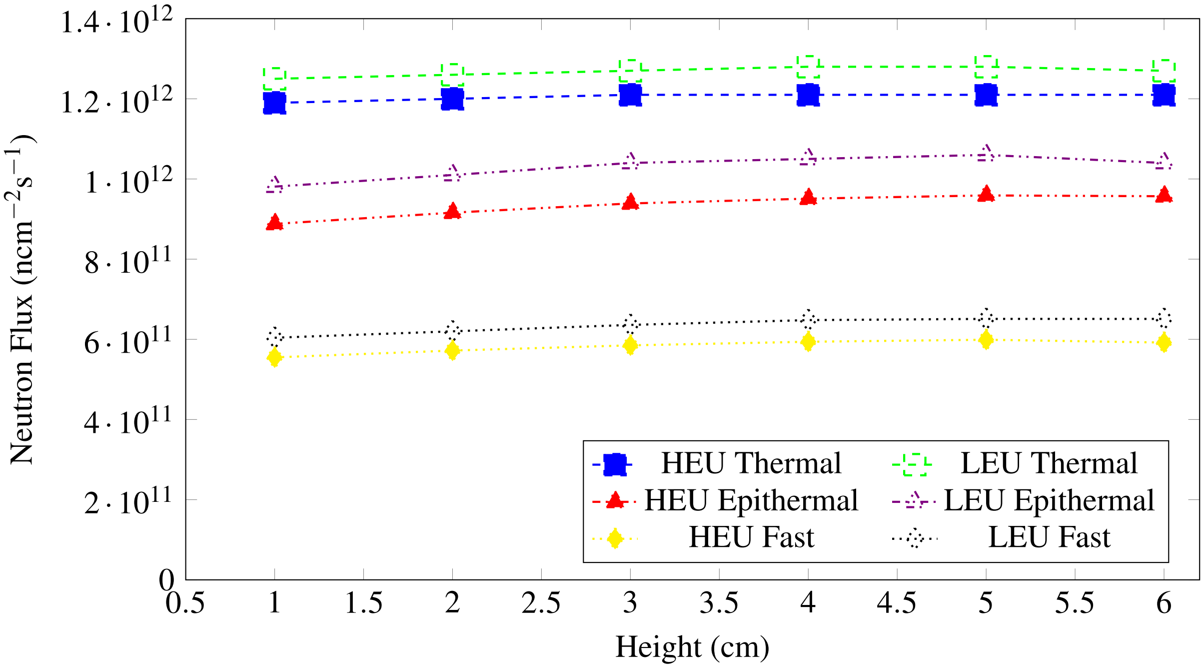

Figure 4.12: Comparison of LEU and HEU neutron flux distribution at Inner site 3 at Full Power

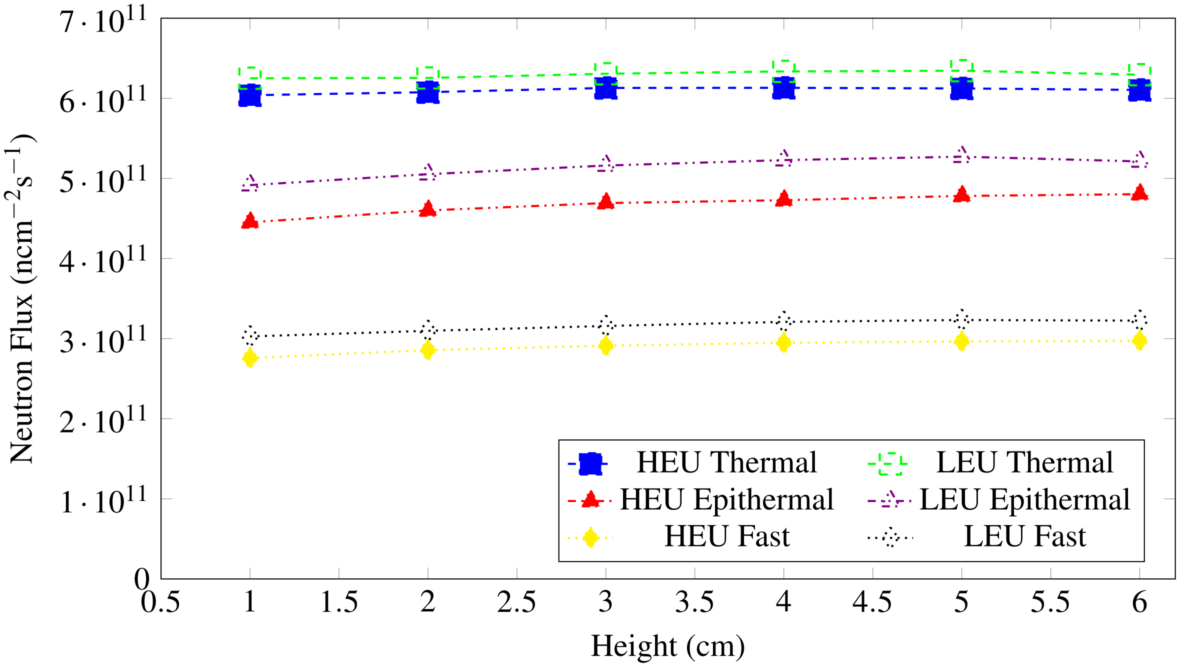

Figure 4.13: Comparison of LEU and HEU neutron flux distribution at Inner site 4 at Half Power

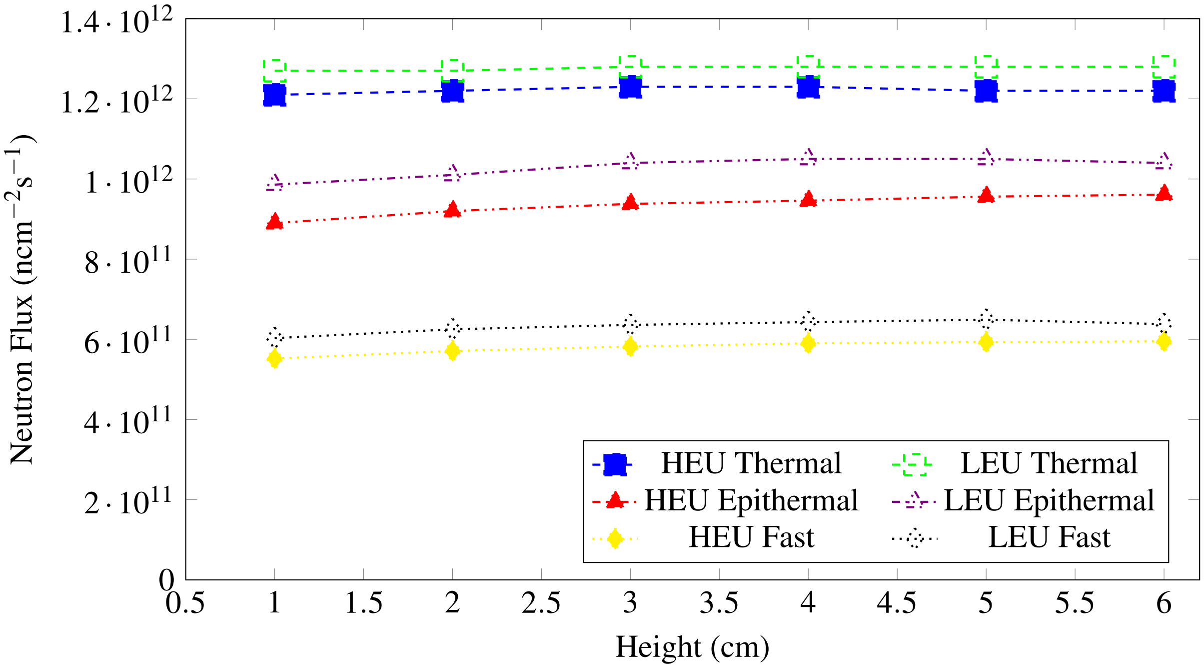

Figure 4.14: Comparison of LEU and HEU neutron flux distribution at Inner site 4 at Full Power

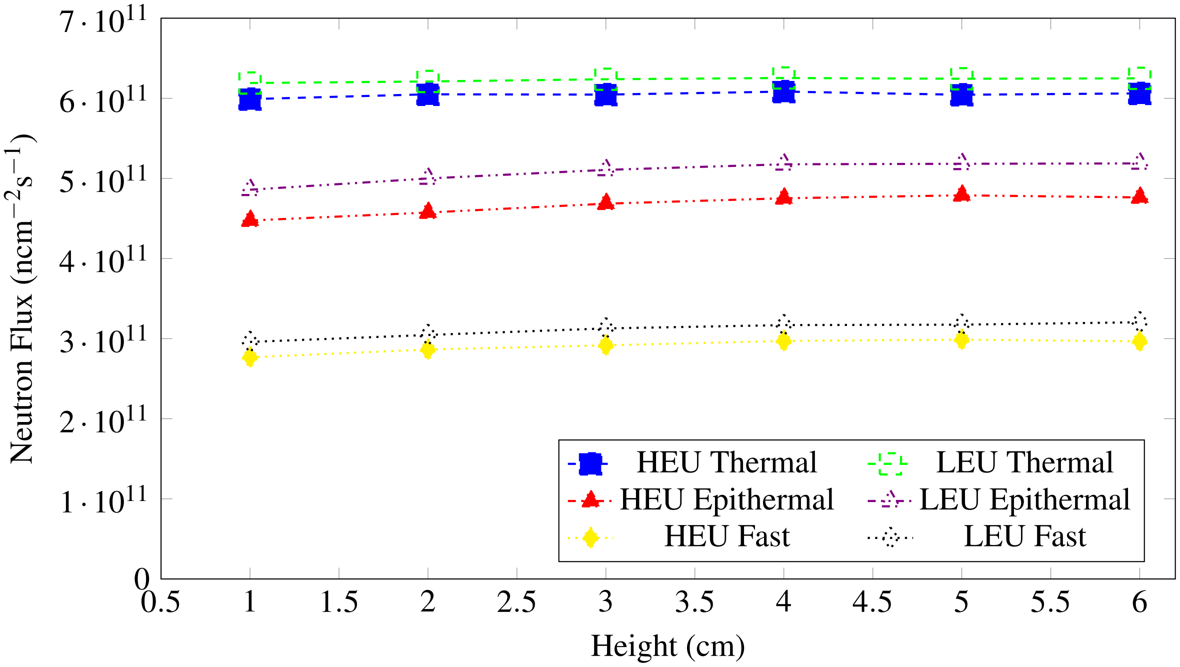

Figure 4.15: Comparison of LEU and HEU neutron flux distribution at Inner site 5 at Half Power

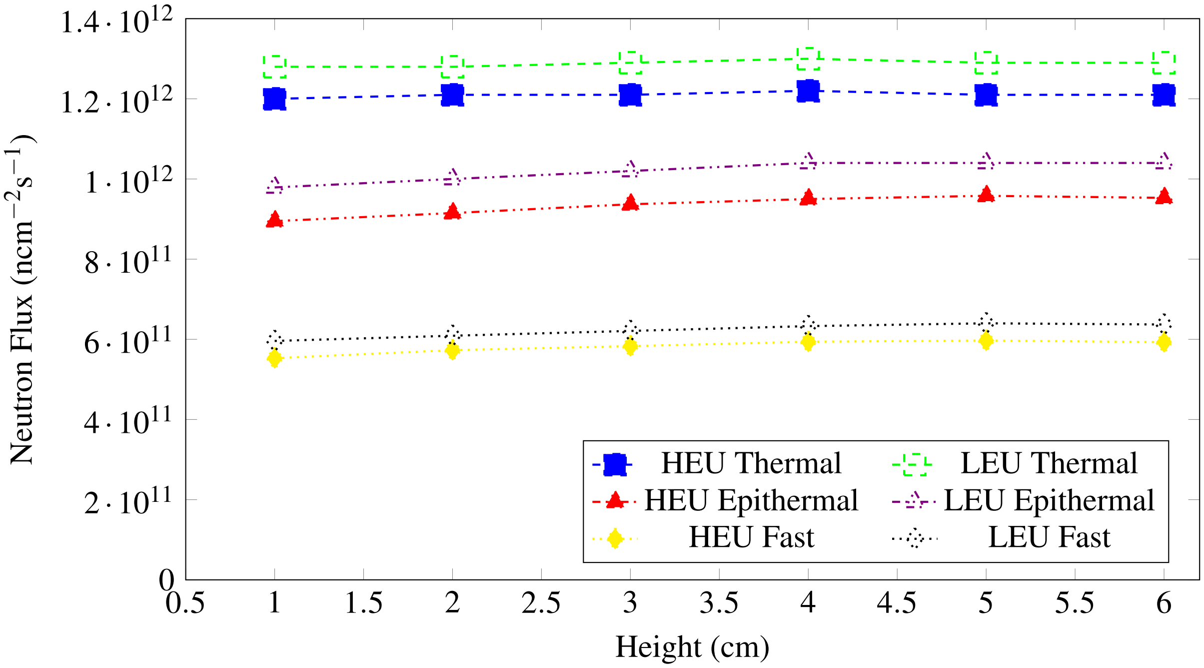

Figure 4.16: Comparison of LEU and HEU neutron flux distribution at Inner site 5 at Full Power

From 4.7 to 4.16 it is observed that the thermal neutron flux shows a fairly flat distribution. This indicates a uniformity in the thermal neutron flux distribution at the inner irradiation sites. Also, the distribution of thermal neutron flux for the LEU and HEU cores are similar. This shows that the conversion of the GHARR-1 core will have minimal changes in the thermal neutron flux distribution in the inner irradiation sites. Unlike the thermal neutron flux distribution, the epithermal neutron flux distribution steadily rises up to the fifth (5 cm from the bottom of the rabbit capsule) segment of the rabbit capsule before dipping slowly above the fifth segment. However just like the thermal neutron flux, the epithermal neutron flux distribution for both the LEU and HEU cores compare well with each other. For the fast neutron energy region, the neutron rises steadily up to the fifth segment then it begins to level off beyond the fifth segment. Again the neutron flux distribution in this region for LEU and HEU cores follow a similar pattern.

Table 4.10: Average neutron flux ranges for inner irradiation sites of LEU core at 17 KW and 34 KW

	Neutron Flux in $10^{11}\text{cm}^{-2}\text{s}^{-1}$					
Power Level	Thermal	Epithermal	Fast	Thermal Ratio	Epithermal Ratio	Fast Ratio
17 KW	6.34 - 6.44	4.89 - 5.25	3.00 - 3.23	0.98	0.93	0.93
34 KW	12.7 - 12.9	9.78 - 10.5	6.00 - 6.46	0.98	0.93	0.93

Table 4.10 gives the range of neutron fluxes in the rabbit capsules as well as the ratio of the minimum to maximum neutron flux in each of the capsules at the inner irradiation sites. The ratio of thermal flux indicates a high level of uniformity of thermal flux at the inner irradiation sites (deviation below 2 %). This further confirms the observation made from the thermal neutron flux distribution plots. This can be attributed to the location (inside the annulus beryllium reflector) of the inner irradiation sites, resulting in high levels of thermalization. The epithermal and fast neutron flux ratio indicate a fairly uniform epithermal and fast neutron flux distribution (deviation below 8 %).

For the outer irradiation sites (Figures 4.17 to 4.26), the neutron flux distributions for the thermal and fast energy regions are almost flat. This indicates uniformity of thermal and fast neutron flux in the outer irradiation sites. In the epithermal region, there is a steady rise neutron flux from the bottom of the rabbit capsule. Just as in the case of the inner irradiation sites, the neutron flux distribution at the outer irradiation sites for both the LEU and HEU cores show similar trends.

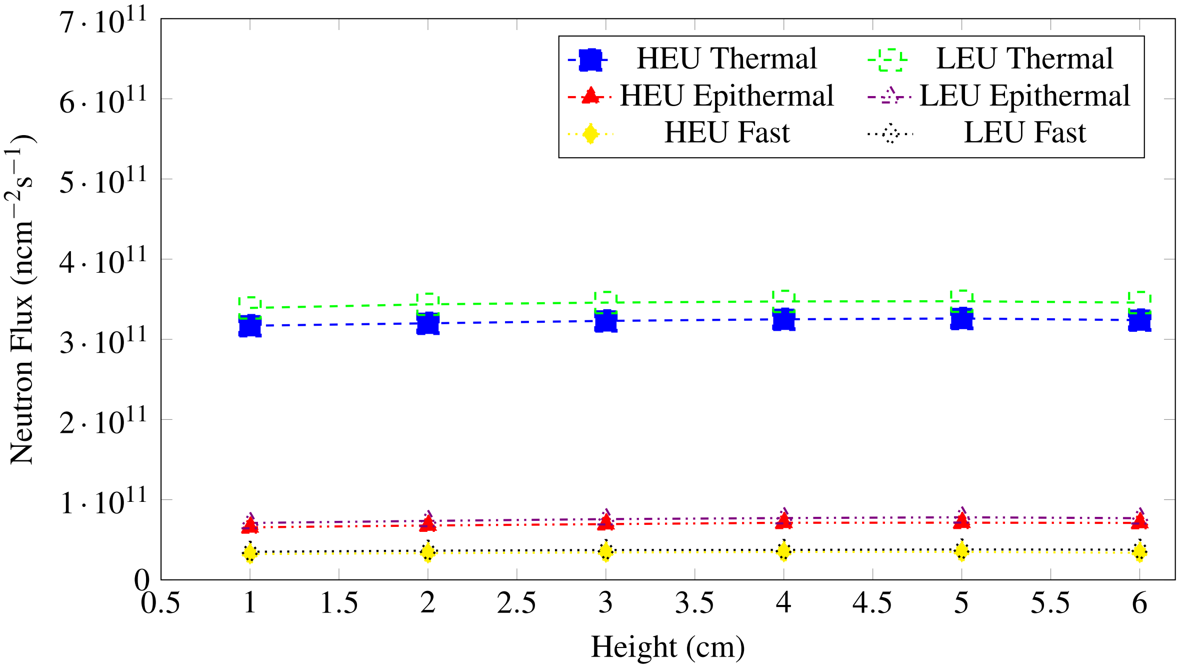

Figure 4.17: Comparison of LEU and HEU neutron flux distribution at Outer site 1 at Half Power

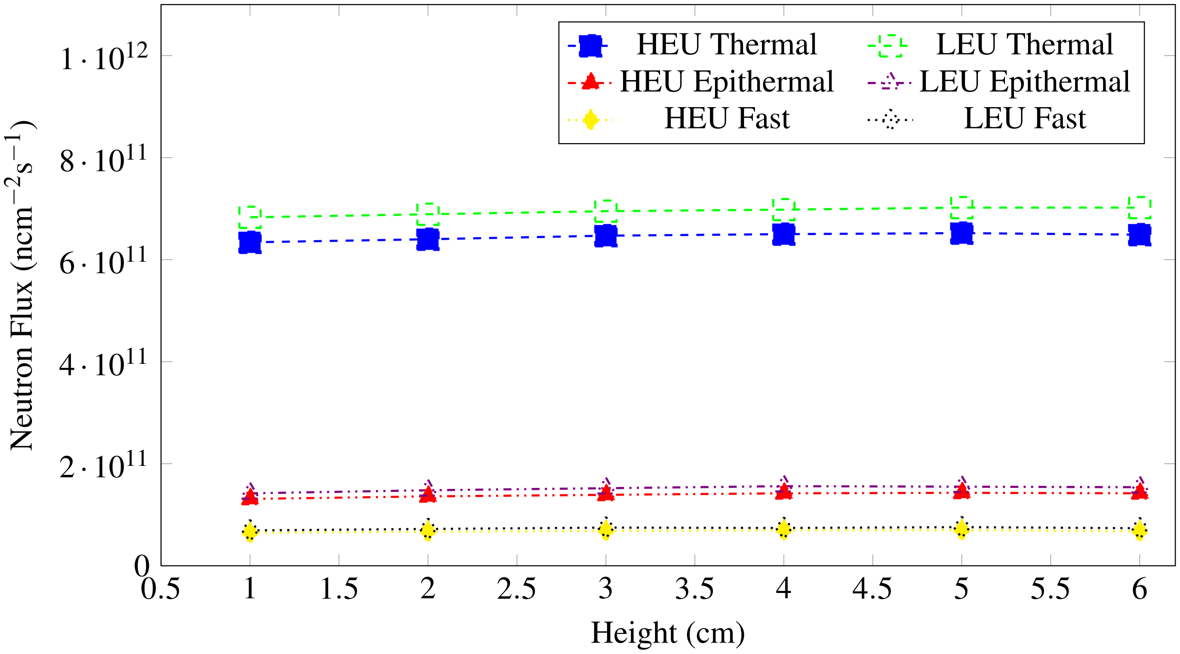

Figure 4.18: Comparison of LEU and HEU neutron flux distribution at Outer site 1 at Full Power

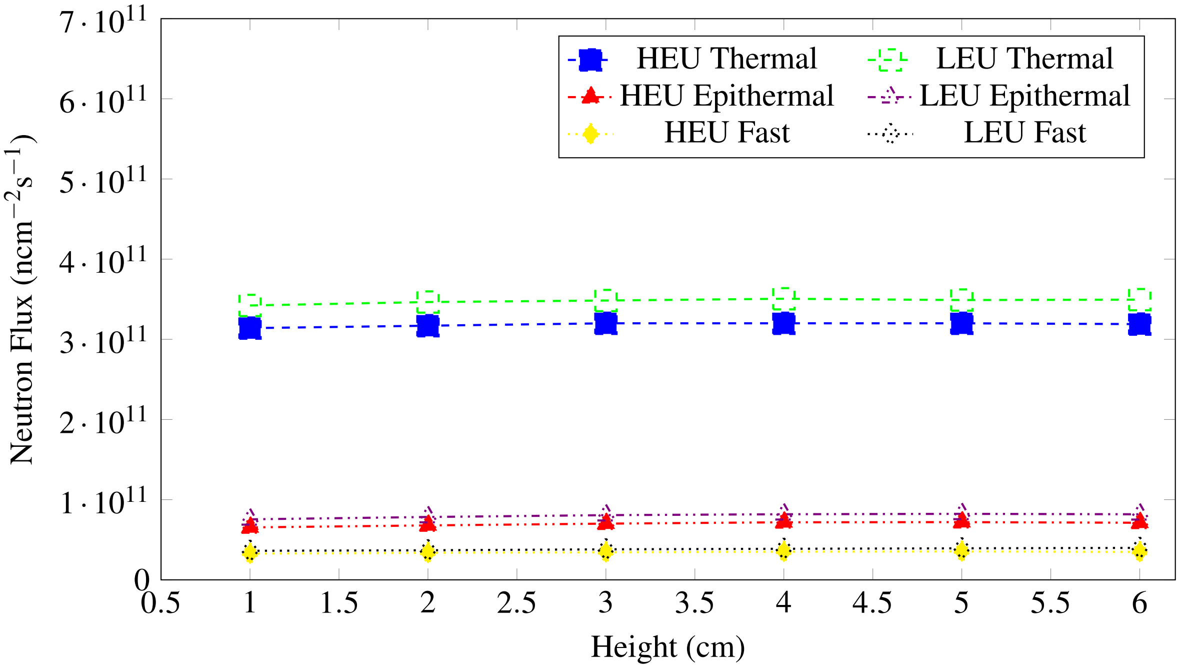

Figure 4.19: Comparison of LEU and HEU neutron flux distribution at Outer site 2 at Half Power

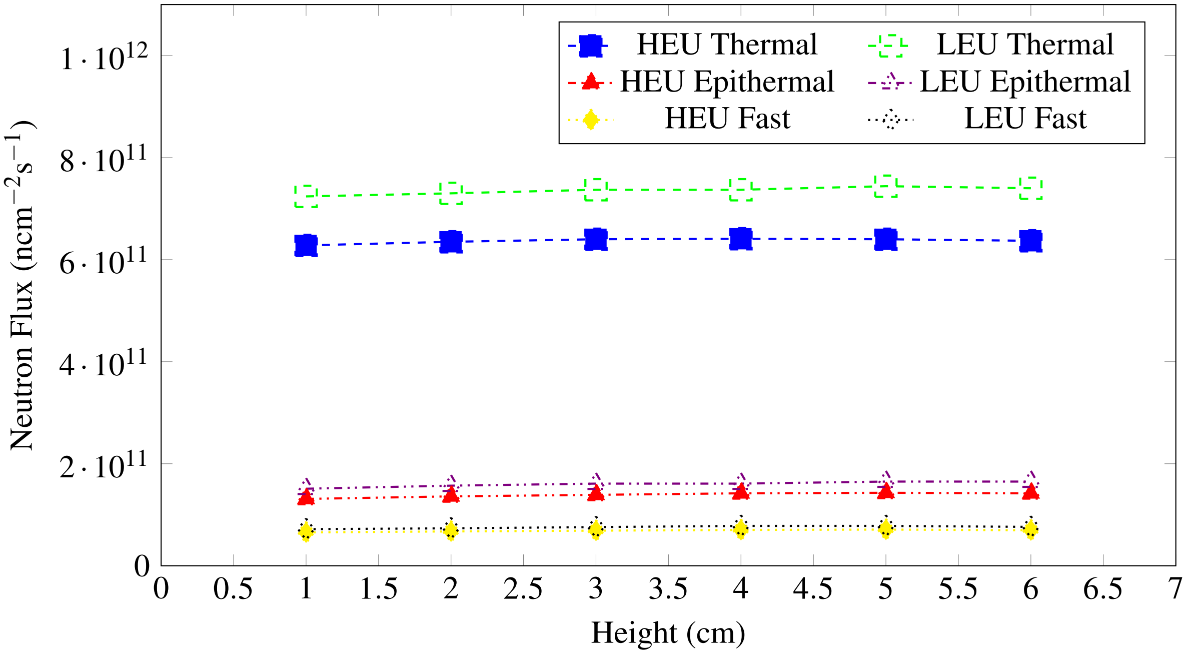

Figure 4.20: Comparison of LEU and HEU neutron flux distribution at Outer site 2 at Full Power

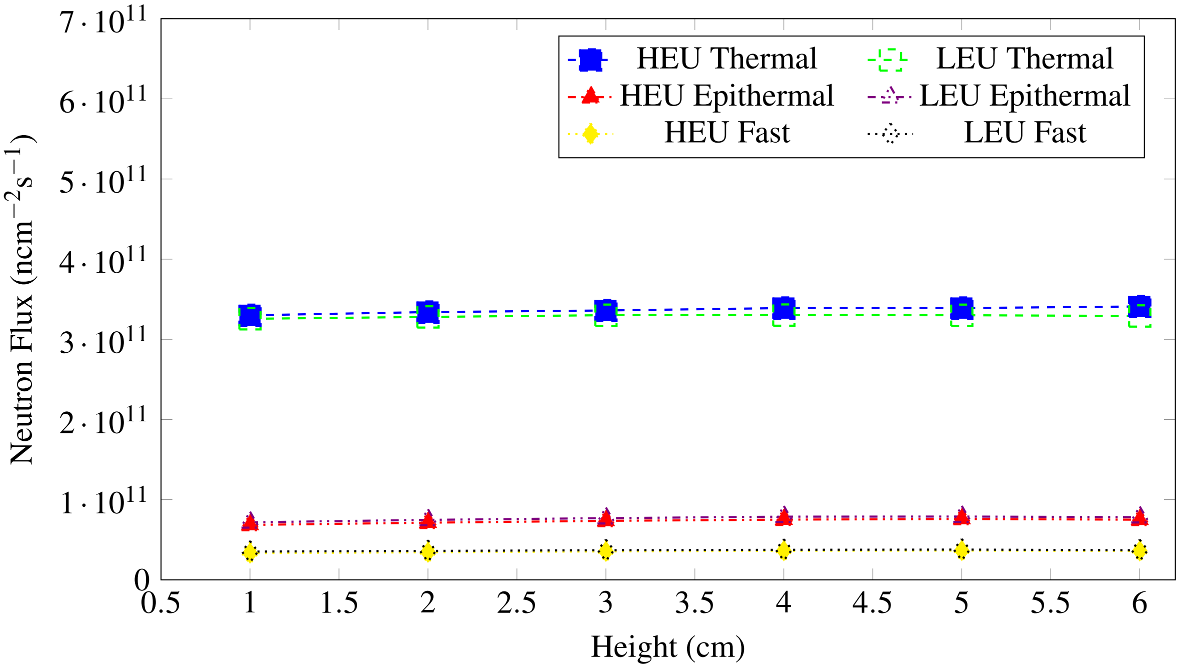

Figure 4.21: Comparison of LEU and HEU neutron flux distribution at Outer site 3 at Half Power

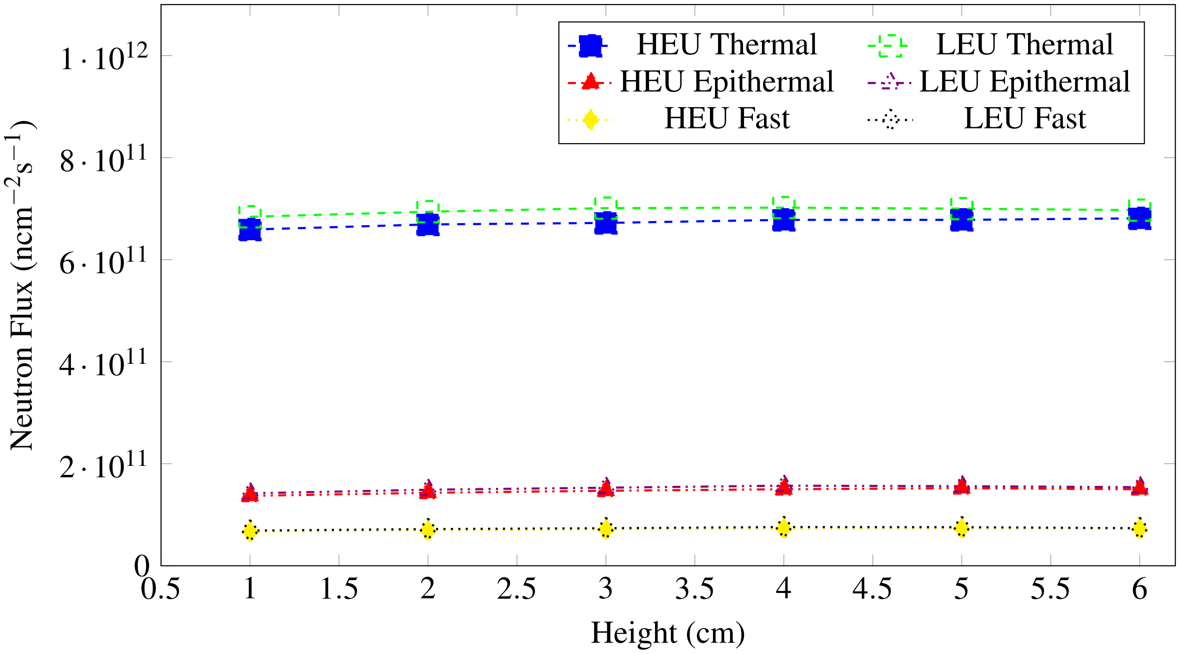

Figure 4.22: Comparison of LEU and HEU neutron flux distribution at Outer site 3 at Full Power

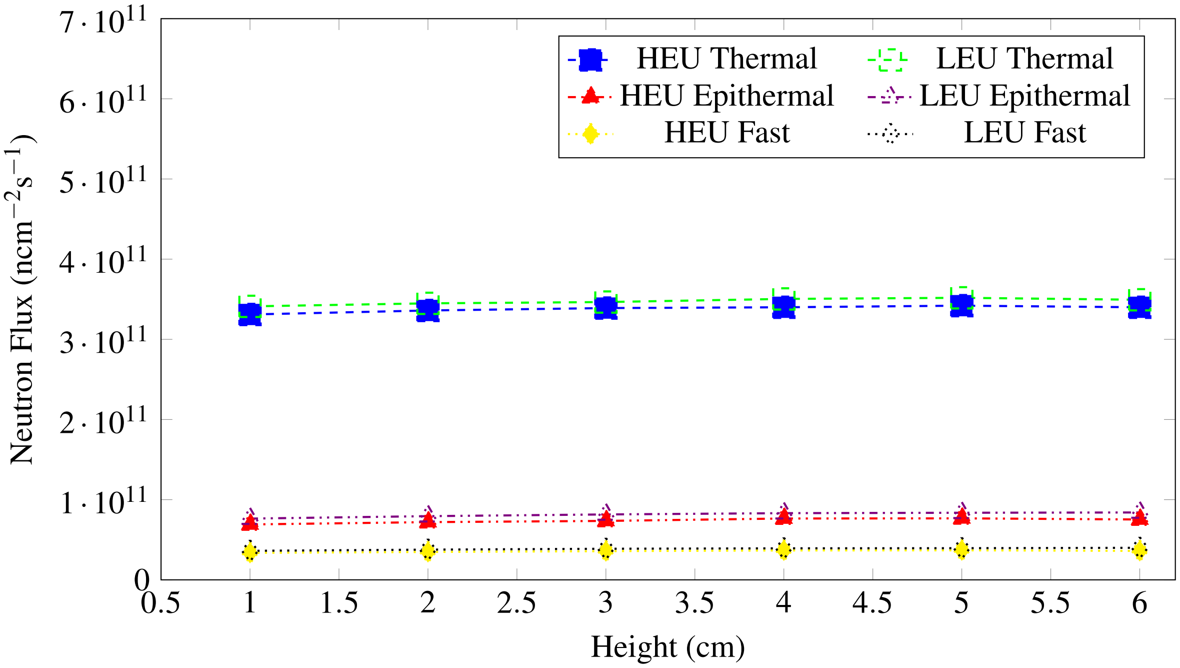

Figure 4.23: Comparison of LEU and HEU neutron flux distribution at Outer site 4 at Half Power

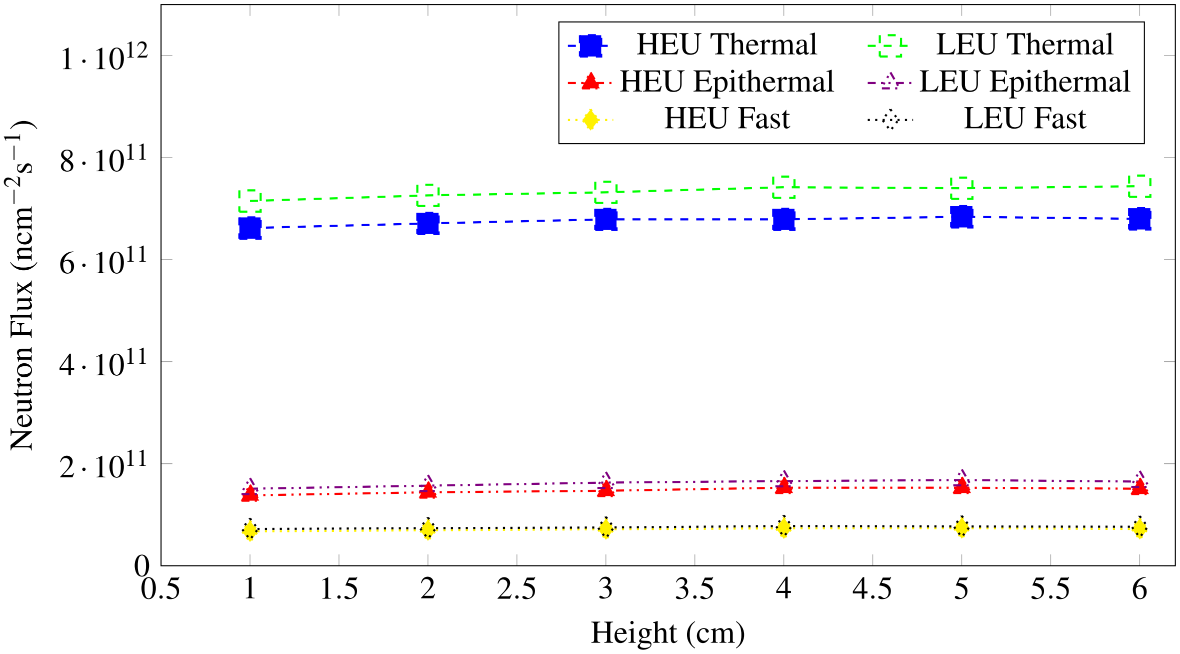

Figure 4.24: Comparison of LEU and HEU neutron flux distribution at Outer site 4 at Full Power

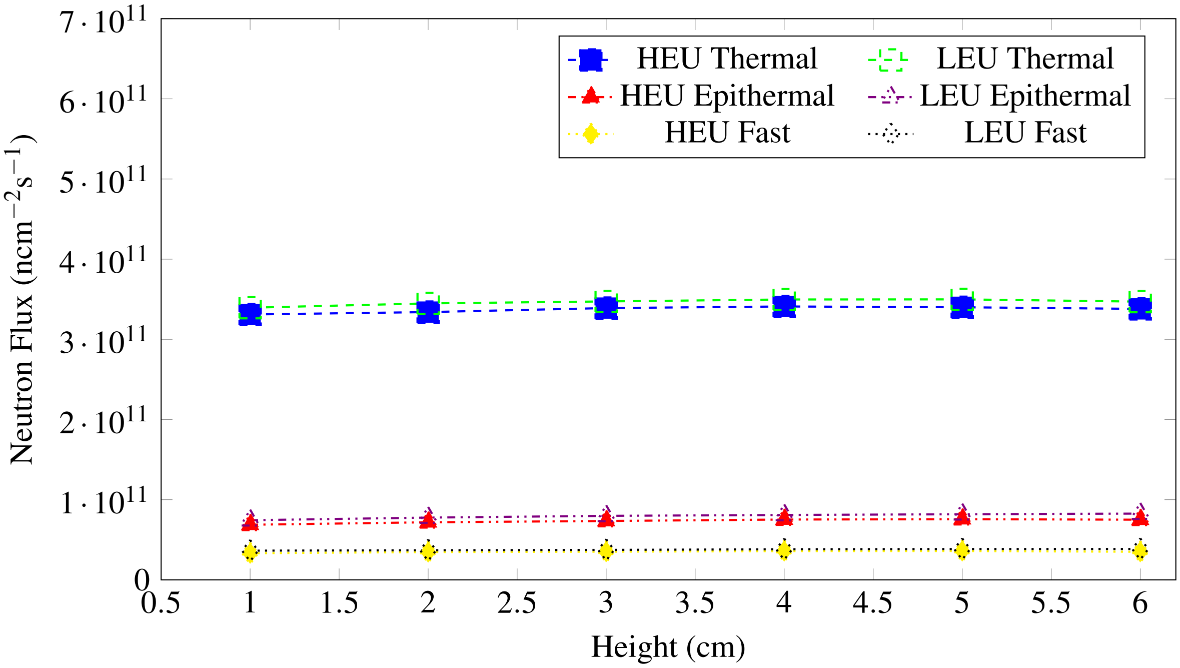

Figure 4.25: Comparison of LEU and HEU neutron flux distribution at Outer site 5 at Half Power

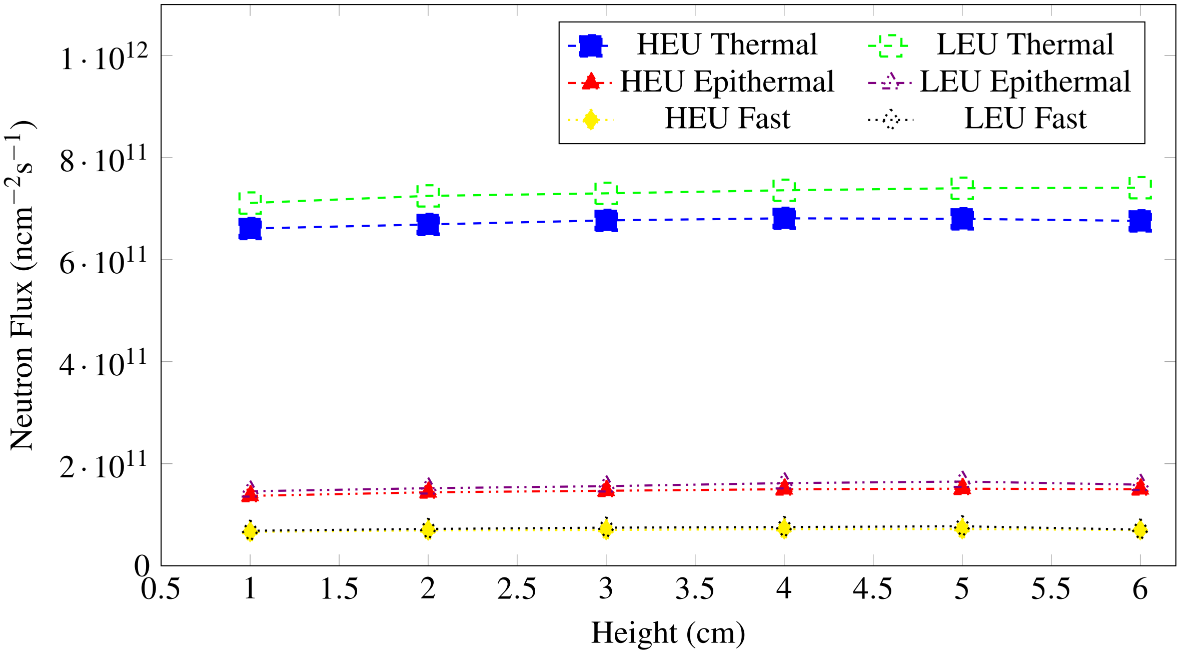

Figure 4.26: Comparison of LEU and HEU neutron flux distribution at Outer site 5 at Full Power

Table 4.11 gives the range of neutron fluxes in the rabbit capsules as well as the ratio of the minimum to maximum neutron flux in each of the capsules at the outer irradiation sites. Just as at the inner irradiation sites, the thermal neutron flux at the outer irradiation sites are very stable (with deviation up to 3 %). The fast neutron flux distribution for the outer irradiation sites also shows a high level of uniformity with deviation up to 10 %. The epithermal neutron flux though fairly uniform shows the highest level of deviation up to 8 %.

Table 4.11: Average neutron flux ranges for outer irradiation sites of LEU core at 17 KW and 34 KW

	Neutron Flux in $10^{11}\text{cm}^{-2}\text{s}^{-1}$					
Power Level	Thermal	Epithermal	Fast	Thermal Ratio	Epithermal Ratio	Fast Ratio
17 KW	3.52 - 3.64	0.74 - 0.82	0.36 - 0.39	0.97	0.90	0.92
34 KW	7.04 - 7.28	1.48 - 1.64	0.72 - 0.78	0.97	0.90	0.92

Generally, the neutron flux distribution at the inner irradiation sites for all three neutron energy ranges are slightly more stable as compared to the outer irradiation sites. However, it can be said from the Figures 4.7 to 4.26 and Tables 4.10 and 4.11 that neutron flux distribution in the volume of rabbit capsules at the GHARR-1 irradiation facility is very uniform. Appendix E presents data used for neutron flux distribution plots in this section.

CHAPTER 5

CONCLUSIONS AND RECOMMENDATIONS

5.1 Conclusion

The main objective of this research was to characterize the neutron spectrum within the volume of rabbit capsules at irradiation sites of the GHARR-1 LEU core. Theoretical method using the MNCP5 code were employed in determining the neutron fluxes and neutron flux distribution at the irradiation sites. Also, the MCNP5 code was used to determine the cadmium ratio of flux monitors based on reaction rates. Results of the neutron flux distribution generally indicated uniformity in all three neutron spectrum energy regions. The neutron flux distribution at the inner irradiation sites were however determined to be more uniform (up to 2 % for thermal, 5 % for epithermal and 3 % for fast) as compared to that of the outer irradiation sites. Also the thermal neutron flux was observed to have the most unifrom distribution (uniformity between 96 % and 99 %).

Based on the cadmium ratios obtained, the resonance integral to thermal cross section ratio, thermal to epithermal neutron flux ratio and the epithermal neutron shaping factor were determined. To validate the methodology, the neutron spectrum of the GHARR-1 HEU core was also characterized. The results obtained compared very well with reults of previous experimental work carried out on the GHARR-1 HEU core. Results of the LEU core irradiation sites (lower absolute value of epithermal neutron shaping factor, thermal to epithermal neutron flux ratio and an increase in thermal power to compensate for thermal neutron flux trade off) indicate some levels of neutron spectrum hardening. Neutron spectrum hardening is the shift of the entire neutron spectrum from lower neutron energies towards higher energies. This results in reduction in the neutron flux in the lower energy ranges. The minimal differences between the neutron flux levels and the neutron spectrum parameters of HEU and LEU cores imply that converting of the Ghana MNSR will not have substantial effects on the characteristics of the neutron spectrum at the irradiation sites.

5.2 Recommendations

There are areas of improvement for this study. Experimental neutron spectrum characterization can be carried out after loading of the GHARR-1 LEU core. This will feature validate the theoretical work carried out in this study.

Burn-up studies could be incorporated into the material card of fuel elements for future characterization work especially after the GHARR-1 LEU core has been used for a substantial amount of time.

APPENDICES

A MCNP Tally Cards

A.0.1 F4 Tally Card

In monte carlo (using the MCNP code) neutron flux can be determined at a point, over a surface or in a volume. For this study the neutron flux within a volume is to be determined. The average neutron flux in a volume, V is given by equation (5.1).

$$\bar{\phi} = \frac{1}{V} \int dE \int dt \int d^3\overrightarrow{r}\,\Phi(\overrightarrow{r}, E, t) \tag{5.1}$$

$\Phi(\overrightarrow{r}, E, t)$ is referred to as the energy dependent neutron flux (neutron spectrum).
$\Phi(\overrightarrow{r}, E, t) = \nu n(\overrightarrow{r}, E, t)$. n is the neutron density and ν is the neutron velocity. Thus equation (5.1) becomes,

$$\bar{\phi} = \frac{1}{V} \int dE \int d^3\overrightarrow{r} \int dt\, \nu n(\overrightarrow{r}, E, t) \tag{5.2}$$

The differential unit of track length, $ds = \nu dt$. Putting this into equation (5.2)

$$\bar{\phi} = \frac{1}{V} \int dE \int d^3\overrightarrow{r} \int ds\, n(\overrightarrow{r}, E, t) \tag{5.3}$$

$n(\overrightarrow{r}, E, t)ds$ is defined as the neutron track length density.
MCNP calculates the neutron flux in a cell as the sum of the track lengths of all neutrons that traverse the volume of the cell. this is illustrated by equation (5.4).

$$\bar{\phi} = \frac{1}{V} \sum_i T_i \tag{5.4}$$

T_i is the track length of the ith neutron in the cell. Figure 5.1 illustrates eight neutron tracks in a volume of interest.

The error or standard deviation of the estimated neutron flux in MCNP is proportional to the inverse of the square root of the total number of track lengths, N for a given problem $\left(\sigma_{ref} \propto 1/\sqrt{N}\right)$. This is a shortfall of the monte carlo method since small error margins is computationally expensive (Snoj & Trkov, 2015).

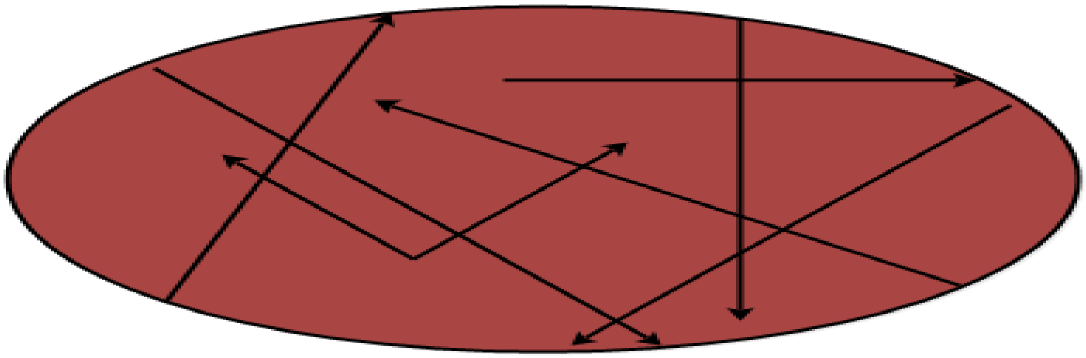

Figure 5.1: Neutron track lengths in a cell

A.0.2 FM Tally Card

The FM card feature of the MCNP code is generally used to modify any flux or current tally of the form $\int \varphi(E)dE$ into $C\int \varphi(E)R_m(E)dE$. $\varphi(E)$ is energy dependent neutron flux (in particles/cm^2), R$_m(E)$ is an operator of additive and/or multiplicative response function or quantity know to the MCNP code, C is a scalar constant and m is the material number which is listed in the data card section of the input file. To determine the ration rate in a material or nuclide using the FM card, energy dependent cross sections are used as the response function.

B Input deck for remodeled components

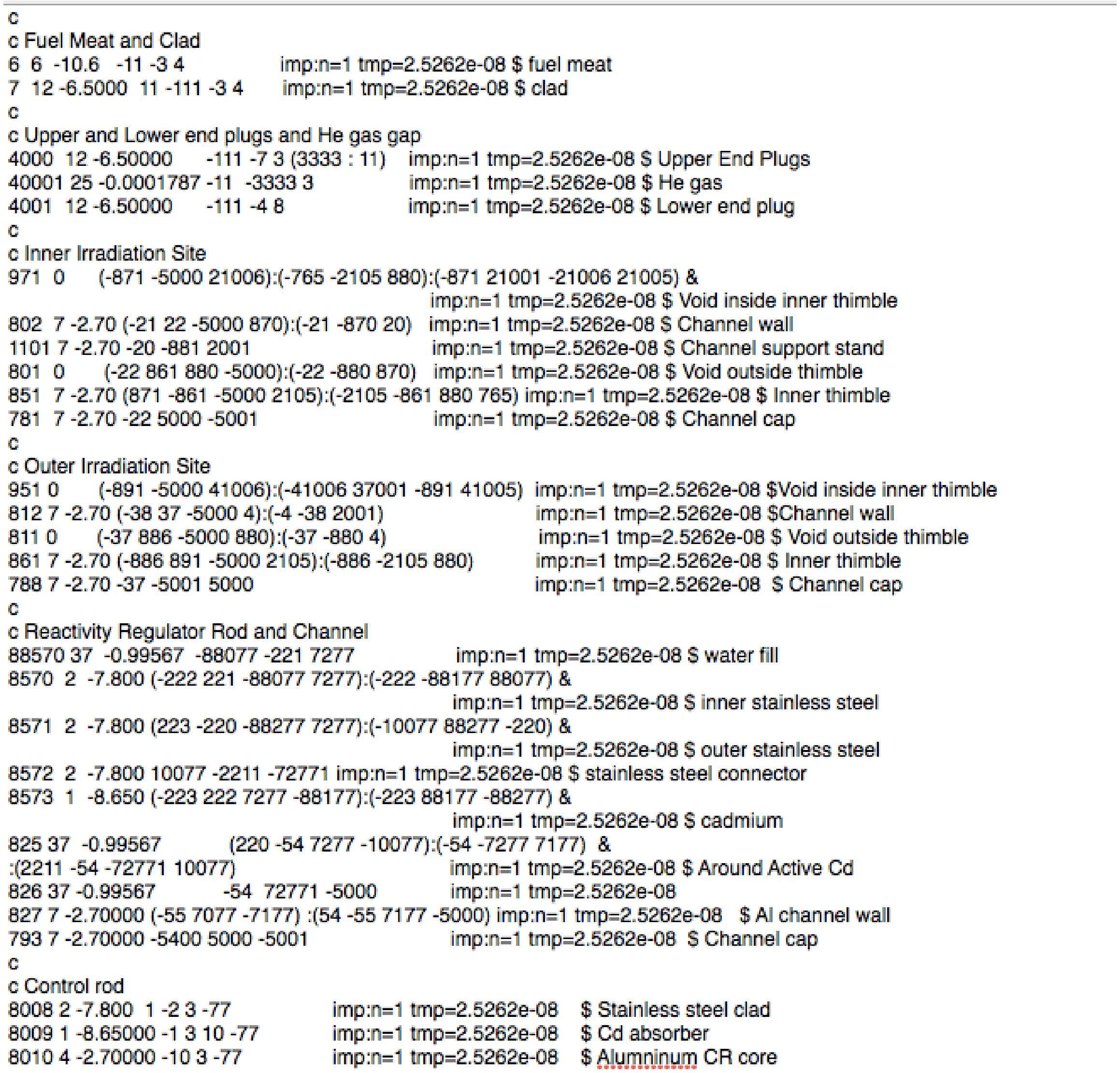

```
c
c Fuel Meat and Clad
6  6  -10.6   -11 -3 4              imp:n=1 tmp=2.5262e-08 $ fuel meat
7  12 -6.5000  11 -111 -3 4         imp:n=1 tmp=2.5262e-08 $ clad
c
c Upper and Lower end plugs and He gas gap
4000  12 -6.50000     -111 -7 3 (3333 : 11)    imp:n=1 tmp=2.5262e-08 $ Upper End Plugs
40001 25 -0.0001787 -11  -3333 3              imp:n=1 tmp=2.5262e-08 $ He gas
4001  12 -6.50000     -111 -4 8                imp:n=1 tmp=2.5262e-08 $ Lower end plug
c
c Inner Irradiation Site
971  0     (-871 -5000 21006):(-765 -2105 880):(-871 21001 -21006 21005) &
                                              imp:n=1 tmp=2.5262e-08 $ Void inside inner thimble
802  7 -2.70 (-21 22 -5000 870):(-21 -870 20)   imp:n=1 tmp=2.5262e-08 $ Channel wall
1101 7 -2.70 -20 -881 2001                      imp:n=1 tmp=2.5262e-08 $ Channel support stand
801  0      (-22 861 880 -5000):(-22 -880 870)  imp:n=1 tmp=2.5262e-08 $ Void outside thimble
851  7 -2.70 (871 -861 -5000 2105):(-2105 -861 880 765) imp:n=1 tmp=2.5262e-08 $ Inner thimble
781  7 -2.70 -22 5000 -5001                     imp:n=1 tmp=2.5262e-08 $ Channel cap
c
c Outer Irradiation Site
951 0      (-891 -5000 41006):(-41006 37001 -891 41005)  imp:n=1 tmp=2.5262e-08 $Void inside inner thimble
812 7 -2.70 (-38 37 -5000 4):(-4 -38 2001)               imp:n=1 tmp=2.5262e-08 $Channel wall
811 0      (-37 886 -5000 880):(-37 -880 4)              imp:n=1 tmp=2.5262e-08 $ Void outside thimble
861 7 -2.70 (-886 891 -5000 2105):(-886 -2105 880)       imp:n=1 tmp=2.5262e-08 $ Inner thimble
788 7 -2.70 -37 -5001 5000                               imp:n=1 tmp=2.5262e-08  $ Channel cap
c
c Reactivity Regulator Rod and Channel
88570 37  -0.99567  -88077 -221 7277               imp:n=1 tmp=2.5262e-08 $ water fill
8570  2  -7.800 (-222 221 -88077 7277):(-222 -88177 88077) &
                                                   imp:n=1 tmp=2.5262e-08 $ inner stainless steel
8571  2  -7.800 (223 -220 -88277 7277):(-10077 88277 -220) &
                                                   imp:n=1 tmp=2.5262e-08 $ outer stainless steel
8572  2  -7.800 10077 -2211 -72771 imp:n=1 tmp=2.5262e-08 $ stainless steel connector
8573  1  -8.650 (-223 222 7277 -88177):(-223 88177 -88277) &
                                                   imp:n=1 tmp=2.5262e-08 $ cadmium
825 37  -0.99567          (220 -54 7277 -10077):(-54 -7277 7177)  &
:(2211 -54 -72771 10077)                          imp:n=1 tmp=2.5262e-08 $ Around Active Cd
826 37 -0.99567           -54  72771 -5000         imp:n=1 tmp=2.5262e-08
827 7 -2.70000 (-55 7077 -7177) :(54 -55 7177 -5000) imp:n=1 tmp=2.5262e-08   $ Al channel wall
793 7 -2.70000 -5400 5000 -5001                   imp:n=1 tmp=2.5262e-08  $ Channel cap
c
c Control rod
8008 2 -7.800  1 -2 3 -77           imp:n=1 tmp=2.5262e-08    $ Stainless steel clad
8009 1 -8.65000 -1 3 10 -77         imp:n=1 tmp=2.5262e-08    $ Cd absorber
8010 4 -2.70000 -10 3 -77           imp:n=1 tmp=2.5262e-08    $ Alumninum CR core
```

Figure 5.2: Cell cards

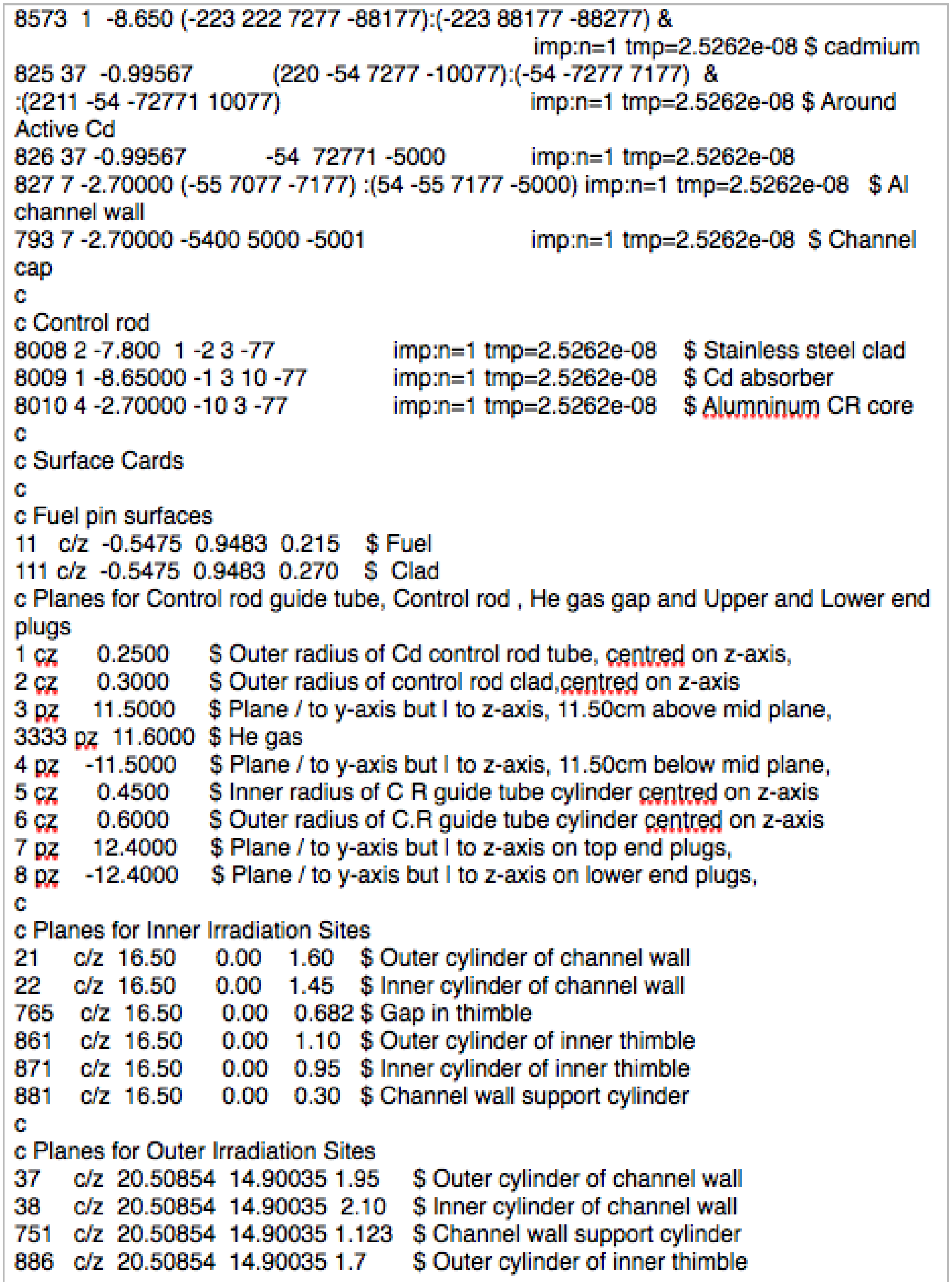

```
8573  1  -8.650 (-223 222 7277 -88177):(-223 88177 -88277) &
                                                        imp:n=1 tmp=2.5262e-08 $ cadmium
825 37  -0.99567          (220 -54 7277 -10077):(-54 -7277 7177)  &
:(2211 -54 -72771 10077)                                imp:n=1 tmp=2.5262e-08 $ Around
Active Cd
826 37 -0.99567          -54  72771 -5000           imp:n=1 tmp=2.5262e-08
827 7 -2.70000 (-55 7077 -7177) :(54 -55 7177 -5000) imp:n=1 tmp=2.5262e-08   $ Al
channel wall
793 7 -2.70000 -5400 5000 -5001                         imp:n=1 tmp=2.5262e-08  $ Channel
cap
c
c Control rod
8008 2 -7.800  1 -2 3 -77              imp:n=1 tmp=2.5262e-08    $ Stainless steel clad
8009 1 -8.65000 -1 3 10 -77            imp:n=1 tmp=2.5262e-08    $ Cd absorber
8010 4 -2.70000 -10 3 -77              imp:n=1 tmp=2.5262e-08    $ Alumninum CR core
c
c Surface Cards
c
c Fuel pin surfaces
11   c/z  -0.5475  0.9483  0.215    $ Fuel
111 c/z  -0.5475  0.9483  0.270    $  Clad
c Planes for Control rod guide tube, Control rod , He gas gap and Upper and Lower end
plugs
1 cz      0.2500     $ Outer radius of Cd control rod tube, centred on z-axis,
2 cz      0.3000     $ Outer radius of control rod clad,centred on z-axis
3 pz     11.5000     $ Plane / to y-axis but l to z-axis, 11.50cm above mid plane,
3333 pz  11.6000  $ He gas
4 pz    -11.5000     $ Plane / to y-axis but l to z-axis, 11.50cm below mid plane,
5 cz      0.4500     $ Inner radius of C R guide tube cylinder centred on z-axis
6 cz      0.6000     $ Outer radius of C.R guide tube cylinder centred on z-axis
7 pz     12.4000     $ Plane / to y-axis but l to z-axis on top end plugs,
8 pz    -12.4000     $ Plane / to y-axis but l to z-axis on lower end plugs,
c
c Planes for Inner Irradiation Sites
21     c/z  16.50      0.00     1.60    $ Outer cylinder of channel wall
22     c/z  16.50      0.00     1.45    $ Inner cylinder of channel wall
765     c/z  16.50      0.00     0.682 $ Gap in thimble
861     c/z  16.50      0.00     1.10    $ Outer cylinder of inner thimble
871     c/z  16.50      0.00     0.95    $ Inner cylinder of inner thimble
881     c/z  16.50      0.00     0.30    $ Channel wall support cylinder
c
c Planes for Outer Irradiation Sites
37     c/z  20.50854  14.90035 1.95      $ Outer cylinder of channel wall
38     c/z  20.50854  14.90035  2.10     $ Inner cylinder of channel wall
751   c/z  20.50854  14.90035 1.123    $ Channel wall support cylinder
886   c/z  20.50854  14.90035 1.7        $ Outer cylinder of inner thimble
```

Figure 5.3: Surface cards

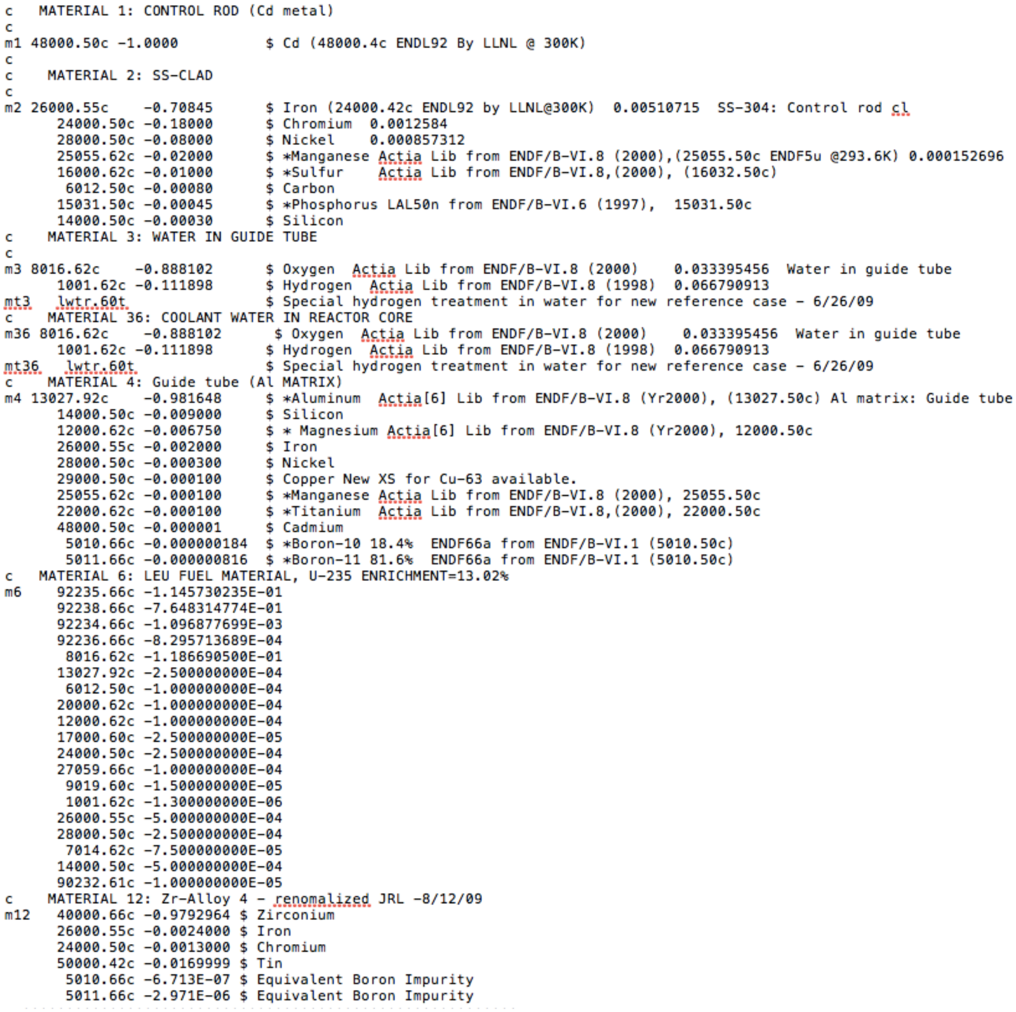

```
c   MATERIAL 1: CONTROL ROD (Cd metal)
c
m1 48000.50c -1.0000          $ Cd (48000.4c ENDL92 By LLNL @ 300K)
c
c    MATERIAL 2: SS-CLAD
c
m2 26000.55c    -0.70845      $ Iron (24000.42c ENDL92 by LLNL@300K)  0.00510715  SS-304: Control rod cl
      24000.50c -0.18000      $ Chromium  0.0012584
      28000.50c -0.08000      $ Nickel    0.000857312
      25055.62c -0.02000      $ *Manganese Actia Lib from ENDF/B-VI.8 (2000),(25055.50c ENDF5u @293.6K) 0.000152696
      16000.62c -0.01000      $ *Sulfur    Actia Lib from ENDF/B-VI.8,(2000), (16032.50c)
       6012.50c -0.00080      $ Carbon
      15031.50c -0.00045      $ *Phosphorus LAL50n from ENDF/B-VI.6 (1997),  15031.50c
      14000.50c -0.00030      $ Silicon
c    MATERIAL 3: WATER IN GUIDE TUBE
c
m3 8016.62c    -0.888102      $ Oxygen  Actia Lib from ENDF/B-VI.8 (2000)    0.033395456  Water in guide tube
      1001.62c -0.111898      $ Hydrogen  Actia Lib from ENDF/B-VI.8 (1998)  0.066790913
mt3   lwtr.60t                $ Special hydrogen treatment in water for new reference case - 6/26/09
c    MATERIAL 36: COOLANT WATER IN REACTOR CORE
m36 8016.62c    -0.888102      $ Oxygen  Actia Lib from ENDF/B-VI.8 (2000)    0.033395456  Water in guide tube
      1001.62c -0.111898      $ Hydrogen  Actia Lib from ENDF/B-VI.8 (1998)  0.066790913
mt36   lwtr.60t               $ Special hydrogen treatment in water for new reference case - 6/26/09
c    MATERIAL 4: Guide tube (Al MATRIX)
m4 13027.92c    -0.981648     $ *Aluminum  Actia[6] Lib from ENDF/B-VI.8 (Yr2000), (13027.50c) Al matrix: Guide tube
      14000.50c -0.009000     $ Silicon
      12000.62c -0.006750     $ * Magnesium Actia[6] Lib from ENDF/B-VI.8 (Yr2000), 12000.50c
      26000.55c -0.002000     $ Iron
      28000.50c -0.000300     $ Nickel
      29000.50c -0.000100     $ Copper New XS for Cu-63 available.
      25055.62c -0.000100     $ *Manganese Actia Lib from ENDF/B-VI.8 (2000), 25055.50c
      22000.62c -0.000100     $ *Titanium  Actia Lib from ENDF/B-VI.8,(2000), 22000.50c
      48000.50c -0.000001     $ Cadmium
       5010.66c -0.000000184  $ *Boron-10 18.4%  ENDF66a from ENDF/B-VI.1 (5010.50c)
       5011.66c -0.000000816  $ *Boron-11 81.6%  ENDF66a from ENDF/B-VI.1 (5010.50c)
c   MATERIAL 6: LEU FUEL MATERIAL, U-235 ENRICHMENT=13.02%
m6    92235.66c -1.145730235E-01
      92238.66c -7.648314774E-01
      92234.66c -1.096877699E-03
      92236.66c -8.295713689E-04
       8016.62c -1.186690500E-01
      13027.92c -2.500000000E-04
       6012.50c -1.000000000E-04
      20000.62c -1.000000000E-04
      12000.62c -1.000000000E-04
      17000.60c -2.500000000E-05
      24000.50c -2.500000000E-04
      27059.66c -1.000000000E-04
       9019.60c -1.500000000E-05
       1001.62c -1.300000000E-06
      26000.55c -5.000000000E-04
      28000.50c -2.500000000E-04
       7014.62c -7.500000000E-05
      14000.50c -5.000000000E-04
      90232.61c -1.000000000E-05
c    MATERIAL 12: Zr-Alloy 4 - renomalized JRL -8/12/09
m12   40000.66c -0.9792964 $ Zirconium
      26000.55c -0.0024000 $ Iron
      24000.50c -0.0013000 $ Chromium
      50000.42c -0.0169999 $ Tin
       5010.66c -6.713E-07 $ Equivalent Boron Impurity
       5011.66c -2.971E-06 $ Equivalent Boron Impurity
```

Figure 5.4: Material cards

C Uncertainty Analysis

Error analysis carried out in this study employed the rules of error propagation. For errors in the cadmium ratio and neutron flux errors were calculated using the addition and substraction as well as multiplication and addition rules. For the neutron spectrum parameters the errors associated with each parameter as a result of of other parameters were calculated using the equations C.5 to C.13 below F. De Corte et al., 1981. For each of the parameters, the error associated with it was calculated as the square root of the sum of the squares of each parameter contributing to the error in that particular parameter. The errors calculated using equations C.5 to C.13 are in percentage.

$$Z_\alpha(A_n) = 0.434 \cdot \frac{f + Q_{o,n(\alpha)}}{f} \left| \frac{1}{\alpha} \frac{\left[log\bar{E}_{r,n} - \frac{\sum_i^N log\bar{E}_{r,n}}{N} \right]}{U_i} \right| \tag{C.5}$$

Where U_i is given by equation C.6.

$$U_i = \sum_i^N \left\{ \left[log\bar{E}_{r,i} - \frac{\sum_i^N log\bar{E}_{r,i}}{N} \right] \left[V_i - \frac{\sum_i^N V_i}{N} \right] \right\} \tag{C.6}$$

Where V_i is given by equation C.7.

$$V_i = \frac{q_{o,i}(\alpha)}{Q_{o,i}(\alpha)} log\bar{E}_{r,i} + \frac{0.26 C_\alpha}{Q_{o,i}(\alpha)} \left(\frac{1.67}{\alpha + 0.5} - 1 \right) \tag{C.7}$$

$$Z_\alpha(Q_{o,n}) = \left[Z_\alpha(A_n) \cdot \frac{f + Q_{o,n(\alpha)}}{f} \right] \frac{(\bar{E}_{r,n})^{-\alpha} Q_{o,n}}{Q_{o,n}(\alpha)} \tag{C.8}$$

$$Z_\alpha(\bar{E}_{r,n}) = \left[Z_\alpha(A_n) \cdot \frac{f + Q_{o,n(\alpha)}}{f} \right] \cdot |\alpha| \cdot \frac{q_{o,n}(\alpha)}{Q_{o,n}(\alpha)} \tag{C.9}$$

$$Z_{Q_o(\alpha)}(\alpha) = Z_f(\alpha) = \left| \frac{\alpha}{Q_o(\alpha)} \left\{ q_o(\alpha) ln\bar{E}_r + 0.60 C_\alpha \left(\frac{1.67}{\alpha + 0.5} - 1 \right) \right\} \right| \tag{C.10}$$

$$Z_{Q_o(\alpha)} = \frac{q_o}{q_o(\alpha)} \cdot Z_{Q_o(\alpha)}(\alpha) \tag{C.11}$$

$$Z_f(R_{Cd}, r) = 1 + \frac{Q_{o,r}(\alpha)}{f} \tag{C.12}$$

$$Z_f(E_r) = \left| \alpha \cdot \frac{q_o(\alpha)}{Q_o(\alpha)} \right| \tag{C.13}$$

$Z_\alpha(A_n)$ is the error in α as a result of Activity, $Z_\alpha(Q_{o,n})$ is the error in α as a result of Q_o, $Z_\alpha(\bar{E}_{r,n})$ is the error in α as a result of $\bar{E}_r$, $Z_{Q_o(\alpha)}(\alpha)$ error in $Q_o(\alpha)$ as a result of α, $Z_{Q_o(\alpha)}$ is the error in $Q_o(\alpha)$, $Z_f(R_{Cd}, r)$ error in *f* as a result of R_{Cd}, $Z_f(E_r)$ error in *f* as a result of $\bar{E}_r$ and $Z_f(\alpha)$ error in *f* as a result of α.

D Comparism of HEU and LEU Neutron Fluxes

Table 5.1: Neutron flux at inner irradiation sites for LEU at 17 KW and HEU at 15 KW

		Neutron flux in $10^{11}\text{ncm}^{-2}\text{s}^{-1}$		
Site		Thermal	Epithermal	Fast
1	LEU	6.34±0.0092	5.07±0.0092	3.12±0.0071
	HEU	6.04±0.0060	4.62±0.0059	2.87±0.0045
2	LEU	6.40±0.0093	5.08±0.0092	3.11±0.0070
	HEU	6.08±0.0060	4.62±0.0059	2.87±0.0045
3	LEU	6.35±0.0092	5.14±0.0093	3.16±0.0071
	HEU	6.02±0.0060	4.66±0.0059	2.91±0.0045
4	LEU	6.38±0.0092	5.15±0.0093	3.16±0.0071
	HEU	6.10±0.0061	4.65±0.0059	2.89±0.0045
5	LEU	6.44±0.0093	5.09±0.0092	3.10±0.0070
	HEU	6.04±0.0060	4.66±0.0059	2.90±0.0045

Table 5.2: Neutron flux at inner irradiation sites for LEU at 34 KW and HEU at 30 KW

		Neutron flux in $10^{12}\text{ncm}^{-2}\text{s}^{-1}$		
Site		Thermal	Epithermal	Fast
1	LEU	1.27±0.0184	1.01±0.0184	0.62±0.0141
	HEU	1.21±0.00121	0.92±0.00117	0.57±0.0009
2	LEU	1.28±0.0185	1.02±0.0184	0.62±0.0141
	HEU	1.22±0.00121	0.92±0.00117	0.57±0.0009
3	LEU	1.27±0.0184	1.03±0.0185	0.63±0.0142
	HEU	1.2±0.0012	0.93±0.00118	0.58±0.00091
4	LEU	1.28±0.0185	1.03±0.0185	0.63±0.0142
	HEU	1.22±0.00121	0.93±0.00118	0.58±0.0009
5	LEU	1.29±0.0186	1.02±0.0184	0.62±0.0141
	HEU	1.21±0.00121	0.93±0.00118	0.58±0.00091

Table 5.3: Neutron flux at outer irradiation sites for LEU at 17 KW and HEU at 15 KW

		Neutron flux in $10^{11}\mathrm{ncm}^{-2}\mathrm{s}^{-1}$		
Site		Thermal	Epithermal	Fast
1	LEU	3.47±0.0078	0.75±0.0056	0.37±0.0034
	HEU	3.22±0.0028	0.69±0.0016	0.34±0.0011
2	LEU	3.67±0.0116	0.8±0.0081	0.38±0.0048
	HEU	3.18±0.0028	0.69±0.0016	0.34±0.0011
3	LEU	3.48±0.0076	0.76±0.0055	0.37±0.0034
	HEU	3.36±0.004	0.73±0.0023	0.35±0.0015
4	LEU	3.66±0.0116	0.8±0.0082	0.38±0.0048
	HEU	3.38±0.004	0.74±0.0023	0.36±0.0015
5	LEU	3.64±0.0114	0.78±0.0077	0.37±0.0045
	HEU	3.37±0.004	0.73±0.0023	0.35±0.0015

Table 5.4: Neutron flux at outer irradiation sites for LEU at 34 KW and HEU at 30 KW

		Neutron flux in $10^{11}\mathrm{ncm}^{-2}\mathrm{s}^{-1}$		
Site		Thermal	Epithermal	Fast
1	LEU	6.94±0.0088	1.51±0.0051	0.73±0.0035
	HEU	6.45±0.0071	1.38±0.0057	0.68±0.0022
2	LEU	7.35±0.0124	1.59±0.0072	0.75±0.0048
	HEU	6.36±0.0071	1.39±0.0056	0.69±0.0022
3	LEU	6.96±0.0088	1.52±0.0051	0.73±0.0035
	HEU	6.71±0.0106	1.46±0.0079	0.7±0.0031
4	LEU	7.31±0.0124	1.61±0.0072	0.75±0.0047
	HEU	6.75±0.0106	1.47±0.008	0.71±0.0031
5	LEU	7.29±0.0124	1.56±0.0071	0.74±0.0047
	HEU	6.74±0.0104	1.46±0.008	0.7±0.0031

E Neutron flux distribution

Column numbers 1 to 5 for each table in this section represent irradiation site numbers.

Table 5.5: Neutron flux at LEU core inner irradiation sites at 17 KW

Neutron flux in $10^{11}\mathrm{ncm}^{-2}\mathrm{s}^{-1}$					
Thermal flux					
	1	2	3	4	5
1 cm	6.29±0.0167	6.33±0.0167	6.27±0.0166	6.34±0.0167	6.39±0.0168
2 cm	6.31±0.0167	6.37±0.0168	6.32±0.0167	6.35±0.0167	6.41±0.0169
3 cm	6.35±0.0168	6.43±0.0169	6.36±0.0168	6.39±0.0168	6.45±0.0169
4 cm	6.39±0.0168	6.44±0.0169	6.42±0.0169	6.41±0.0169	6.48±0.0170
5 cm	6.38±0.0170	6.44±0.0171	6.38±0.0170	6.41±0.0171	6.45±0.0171
6 cm	6.34±0.0278	6.42±0.0282	6.36±0.0280	6.38±0.0280	6.46±0.0282
Epithermal flux					
	1	2	3	4	5
1 cm	4.83±0.0166	4.87±0.0167	4.90±0.0168	4.93±0.0168	4.9±0.0168
2 cm	5.02±0.0170	4.99±0.0169	5.06±0.0171	5.07±0.017	5.01±0.0170
3 cm	5.14±0.0172	5.12±0.0172	5.19±0.0173	5.18±0.0172	5.12±0.0171
4 cm	5.15±0.0172	5.16±0.0172	5.26±0.0174	5.27±0.0174	5.19±0.0173
5 cm	5.20±0.0175	5.23±0.0175	5.29±0.0176	5.27±0.0176	5.21±0.0175
6 cm	5.16±0.0288	5.15±0.0288	5.22±0.029	5.22±0.0291	5.21±0.0290
Fast flux					
	1	2	3	4	5
1 cm	2.97±0.0131	2.99±0.0131	3.02±0.0132	3.02±0.0132	2.98±0.0131
2 cm	3.09±0.0134	3.07±0.0133	3.10±0.0134	3.13±0.0134	3.05±0.0132
3 cm	3.14±0.0134	3.12±0.0134	3.18±0.0135	3.18±0.0135	3.11±0.0134
4 cm	3.19±0.0136	3.18±0.0135	3.24±0.0137	3.22±0.0136	3.17±0.0135
5 cm	3.22±0.0138	3.19±0.0137	3.25±0.0138	3.24±0.0138	3.20±0.0137
6 cm	3.15±0.0228	3.18±0.0231	3.26±0.0234	3.19±0.023	3.18±0.0230

Table 5.6: Neutron flux at LEU core outer irradiation sites at 17 KW

	Neutron flux in 10^{11}ncm^{-2}s^{-1}				
	Thermal flux				
	1	2	3	4	5
1 cm	3.41±0.0075	3.62±0.0011	3.42±0.0007	3.57±0.0011	3.55±0.0011
2 cm	3.45±0.0075	3.65±0.0115	3.47±0.0076	3.63±0.0114	3.63±0.0114
3 cm	3.47±0.0075	3.69±0.0115	3.5±0.0076	3.66±0.0114	3.65±0.0114
4 cm	3.49±0.0076	3.68±0.0116	3.51±0.0076	3.71±0.0115	3.68±0.0115
5 cm	3.51±0.0076	3.72±0.0115	3.5±0.0076	3.7±0.0116	3.7±0.0115
6 cm	3.51±0.0077	3.7±0.0117	3.49±0.0077	3.72±0.0117	3.71±0.0117
	Epithermal flux				
	1	2	3	4	5
1 cm	0.71±0.0044	0.75±0.0068	0.71±0.0043	0.75±0.0067	0.73±0.0067
2 cm	0.74±0.0044	0.79±0.0067	0.75±0.0045	0.79±0.0067	0.76±0.0066
3 cm	0.76±0.0044	0.8±0.0067	0.77±0.0045	0.81±0.0067	0.78±0.0066
4 cm	0.78±0.0045	0.81±0.0068	0.78±0.0045	0.83±0.0068	0.81±0.0067
5 cm	0.77±0.0046	0.82±0.0068	0.78±0.0046	0.84±0.0069	0.83±0.0068
6 cm	0.77±0.0046	0.83±0.0069	0.77±0.0046	0.83±0.007	0.80±0.0070
	Fast flux				
	1	2	3	4	5
1 cm	0.35±0.0030	0.36±0.0047	0.34±0.0032	0.36±0.0046	0.34±0.0044
2 cm	0.36±0.0031	0.37±0.0046	0.36±0.0031	0.37±0.0046	0.36±0.0045
3 cm	0.37±0.0031	0.38±0.0046	0.37±0.0031	0.37±0.0046	0.37±0.0045
4 cm	0.37±0.0032	0.39±0.0047	0.38±0.0032	0.39±0.0046	0.38±0.0046
5 cm	0.38±0.0032	0.39±0.0047	0.38±0.0032	0.38±0.0047	0.39±0.0046
6 cm	0.37±0.0033	0.38±0.0048	0.37±0.0033	0.38±0.0047	0.35±0.0047

Table 5.7: Neutron flux at LEU core inner irradiation sites at 34 KW

	Neutron flux in $10^{12} \mathrm{ncm}^{-2}\mathrm{s}^{-1}$				
	Thermal flux				
	1	2	3	4	5
1 cm	1.26±0.0033	1.27±0.0033	1.25±0.0033	1.27±0.0033	1.28±0.0034
2 cm	1.26±0.0033	1.27±0.0034	1.26±0.0033	1.27±0.0034	1.28±0.0034
3 cm	1.27±0.0335	1.29±0.0338	1.27±0.0336	1.28±0.0337	1.29±0.0338
4 cm	1.28±0.0337	1.29±0.0338	1.28±0.0338	1.28±0.0338	1.3±0.0339
5 cm	1.28±0.034	1.29±0.0342	1.28±0.034	1.28±0.0341	1.29±0.0342
6 cm	1.27±0.0556	1.28±0.0563	1.27±0.056	1.28±0.056	1.29±0.0564
	Epithermal flux				
	1	2	3	4	5
1 cm	0.97±0.0341	0.97±0.0337	0.98±0.0341	0.99±0.0340	0.98±0.0340
2 cm	1.00±0.0343	1.00±0.0338	1.01±0.0341	1.01±0.0341	1.00±0.0339
3 cm	1.03±0.0344	1.02±0.0343	1.04±0.0345	1.04±0.0345	1.02±0.0343
4 cm	1.03±0.0344	1.03±0.0344	1.05±0.0348	1.05±0.0348	1.04±0.0345
5 cm	1.04±0.0349	1.05±0.0350	1.06±0.0352	1.05±0.0351	1.04±0.0349
6 cm	1.03±0.0575	1.03±0.0579	1.04±0.0581	1.04±0.0579	1.04±0.0564
	Fast flux				
	1	2	3	4	5
1 cm	0.59±0.0266	0.60±0.0264	0.60±0.0266	0.60±0.0268	0.60±0.0267
2 cm	0.62±0.0267	0.61±0.0266	0.62±0.0267	0.63±0.0268	0.61±0.0265
3 cm	0.63±0.0269	0.62±0.0268	0.64±0.0270	0.64±0.0270	0.62±0.0267
4 cm	0.64±0.0271	0.64±0.0270	0.65±0.0273	0.64±0.0272	0.63±0.0270
5 cm	0.64±0.0275	0.64±0.0274	0.65±0.0276	0.65±0.0276	0.64±0.0274
6 cm	0.63±0.0455	0.64±0.0461	0.65±0.0469	0.64±0.0460	0.64±0.0460

Table 5.8: Neutron flux at LEU core outer irradiation sites at 34 KW

	Neutron flux in $10^{12} ncm^{-2}s^{-1}$				
	Thermal flux				
	1	2	3	4	5
1 cm	6.83±0.015	7.24±0.0023	6.84±0.0015	7.15±0.0023	7.11±0.0023
2 cm	6.89±0.0151	7.3±0.0229	6.94±0.0151	7.26±0.0229	7.25±0.0228
3 cm	6.95±0.0151	7.37±0.0231	7.01±0.0152	7.32±0.023	7.3±0.0229
4 cm	6.98±0.0152	7.37±0.0231	7.02±0.0153	7.42±0.0232	7.36±0.0231
5 cm	7.02±0.0154	7.44±0.0235	7±0.0154	7.4±0.0234	7.4±0.0234
6 cm	7.02±0.0256	7.4±0.0389	6.97±0.0255	7.44±0.039	7.41±0.0389
	Epithermal flux				
	1	2	3	4	5
1 cm	1.42±0.0009	1.51±0.0013	1.42±0.0009	1.51±0.0013	1.46±0.0013
2 cm	1.48±0.0089	1.57±0.0134	1.49±0.0089	1.57±0.0134	1.52±0.0132
3 cm	1.52±0.009	1.61±0.0135	1.53±0.009	1.63±0.0136	1.56±0.0134
4 cm	1.56±0.0091	1.61±0.0136	1.57±0.0091	1.66±0.0138	1.62±0.0136
5 cm	1.55±0.0092	1.65±0.0139	1.56±0.0092	1.68±0.014	1.65±0.0139
6 cm	1.54±0.0155	1.65±0.0233	1.54±0.0152	1.65±0.0231	1.59±0.0228
	Fast flux				
	1	2	3	4	5
1 cm	0.69±0.0006	0.72±0.0009	0.69±0.0006	0.72±0.0009	0.69±0.0009
2 cm	0.72±0.0063	0.73±0.0091	0.72±0.0063	0.74±0.0091	0.72±0.0091
3 cm	0.75±0.0064	0.76±0.0093	0.74±0.0063	0.75±0.0092	0.75±0.0092
4 cm	0.74±0.0064	0.78±0.0094	0.76±0.0064	0.78±0.0094	0.76±0.0093
5 cm	0.76±0.0065	0.78±0.0095	0.76±0.0065	0.77±0.0095	0.77±0.0095
6 cm	0.74±0.0112	0.76±0.0161	0.74±0.0111	0.76±0.0163	0.71±0.0155

Table 5.9: Neutron flux at HEU core inner irradiation sites at 15 KW

	Neutron flux in $10^{11}\text{ncm}^{-2}\text{s}^{-1}$				
	Thermal flux				
	1	2	3	4	5
1 cm	6.02±0.0109	6.03±0.0109	5.97±0.0109	6.04±0.0109	5.99±0.0109
2 cm	6.02±0.0109	6.08±0.011	5.99±0.0109	6.08±0.011	6.05±0.011
3 cm	6.06±0.011	6.1±0.011	6.03±0.011	6.13±0.0111	6.05±0.011
4 cm	6.07±0.011	6.09±0.011	6.05±0.011	6.13±0.0111	6.08±0.0111
5 cm	6.05±0.0111	6.1±0.0112	6.05±0.0111	6.12±0.0112	6.04±0.0111
6 cm	6.03±0.0182	6.11±0.0184	6.04±0.0182	6.1±0.0183	6.06±0.0183
	Epithermal flux				
	1	2	3	4	5
1 cm	4.44±0.0107	4.42±0.0106	4.44±0.0107	4.45±0.0107	4.47±0.0107
2 cm	4.55±0.0108	4.55±0.0108	4.58±0.0108	4.6±0.0109	4.57±0.0108
3 cm	4.64±0.0109	4.65±0.0109	4.69±0.011	4.69±0.011	4.68±0.011
4 cm	4.7±0.011	4.7±0.011	4.76±0.011	4.73±0.011	4.75±0.011
5 cm	4.74±0.0111	4.75±0.0111	4.8±0.0112	4.78±0.0112	4.79±0.0112
6 cm	4.74±0.0185	4.75±0.0185	4.79±0.0185	4.8±0.0186	4.76±0.0185
	Fast flux				
	1	2	3	4	5
1 cm	2.74±0.0084	2.73±0.0083	2.78±0.0084	2.76±0.0084	2.77±0.0084
2 cm	2.82±0.0085	2.81±0.0085	2.86±0.0085	2.86±0.0085	2.86±0.0086
3 cm	2.89±0.0086	2.89±0.0086	2.92±0.0086	2.91±0.0086	2.92±0.0086
4 cm	2.94±0.0087	2.95±0.0087	2.97±0.0087	2.95±0.0087	2.97±0.0087
5 cm	2.97±0.0088	2.95±0.0088	3±0.0088	2.96±0.0088	2.99±0.0088
6 cm	2.95±0.0148	2.92±0.0147	2.96±0.0148	2.97±0.0149	2.97±0.0148

Table 5.10: Neutron flux at HEU core outer irradiation sites at 15 KW

	Neutron flux in 10^{11}ncm^{-2}s^{-1}				
	Thermal flux				
	1	2	3	4	5
1 cm	3.17±0.0048	3.14±0.0048	3.3±0.0073	3.31±0.0073	3.31±0.0073
2 cm	3.2±0.0048	3.17±0.0048	3.34±0.0073	3.36±0.0073	3.34±0.0073
3 cm	3.23±0.0049	3.2±0.0049	3.36±0.0074	3.39±0.0074	3.39±0.0074
4 cm	3.25±0.0049	3.2±0.0049	3.39±0.0074	3.4±0.0074	3.41±0.0074
5 cm	3.26±0.005	3.2±0.0049	3.39±0.0075	3.42±0.0075	3.4±0.0075
6 cm	3.24±0.0081	3.19±0.0081	3.41±0.0125	3.4±0.0125	3.38±0.0124
	Epithermal flux				
	1	2	3	4	5
1 cm	0.66±0.0028	0.65±0.0028	0.68±0.0042	0.69±0.0042	0.69±0.0042
2 cm	0.68±0.0028	0.68±0.0028	0.71±0.0043	0.72±0.0043	0.72±0.0043
3 cm	0.69±0.0029	0.7±0.0029	0.74±0.0043	0.73±0.0043	0.73±0.0043
4 cm	0.71±0.0029	0.72±0.0029	0.75±0.0044	0.77±0.0044	0.75±0.0044
5 cm	0.71±0.0029	0.72±0.0029	0.76±0.0044	0.77±0.0045	0.76±0.0044
6 cm	0.71±0.0049	0.71±0.0049	0.75±0.0074	0.75±0.0074	0.75±0.0074
	Fast flux				
	1	2	3	4	5
1 cm	0.32±0.002	0.33±0.002	0.33±0.0029	0.34±0.0029	0.33±0.0029
2 cm	0.33±0.002	0.34±0.002	0.34±0.003	0.35±0.003	0.35±0.003
3 cm	0.34±0.002	0.34±0.002	0.35±0.003	0.36±0.003	0.35±0.003
4 cm	0.35±0.0021	0.35±0.0021	0.36±0.003	0.37±0.003	0.36±0.003
5 cm	0.35±0.0021	0.35±0.0021	0.37±0.0031	0.37±0.0031	0.36±0.003
6 cm	0.34±0.0035	0.35±0.0035	0.36±0.0053	0.36±0.0053	0.35±0.0052

Table 5.11: Neutron flux at HEU core inner irradiation sites at 30 KW

	Neutron flux in 10^{12}ncm^{-2}s^{-1}				
	Thermal flux				
	1	2	3	4	5
1 cm	1.2±0.00218	1.21±0.00219	1.19±0.00218	1.21±0.00219	1.2±0.00218
2 cm	1.2±0.00219	1.22±0.0022	1.2±0.00218	1.22±0.0022	1.21±0.0022
3 cm	1.21±0.0022	1.22±0.00221	1.21±0.0022	1.23±0.00221	1.21±0.0022
4 cm	1.21±0.0022	1.22±0.00221	1.21±0.0022	1.23±0.00221	1.22±0.00221
5 cm	1.21±0.00222	1.22±0.00223	1.21±0.00223	1.22±0.00224	1.21±0.00222
6 cm	1.21±0.00365	1.22±0.00369	1.21±0.00365	1.22±0.00366	1.21±0.00366
	Epithermal flux				
	1	2	3	4	5
1 cm	0.89±0.00213	0.88±0.00213	0.89±0.00213	0.89±0.00213	0.89±0.00214
2 cm	0.91±0.00216	0.91±0.00216	0.92±0.00217	0.92±0.00217	0.91±0.00216
3 cm	0.93±0.00218	0.93±0.00218	0.94±0.00219	0.94±0.00219	0.94±0.00219
4 cm	0.94±0.00219	0.94±0.0022	0.95±0.00221	0.95±0.0022	0.95±0.00221
5 cm	0.95±0.00223	0.95±0.00223	0.96±0.00224	0.96±0.00224	0.96±0.00224
6 cm	0.95±0.0037	0.95±0.0037	0.96±0.0037	0.96±0.00371	0.95±0.00371
	Fast flux				
	1	2	3	4	5
1 cm	0.55±0.00167	0.55±0.00167	0.56±0.00168	0.55±0.00168	0.55±0.00168
2 cm	0.56±0.0017	0.56±0.00169	0.57±0.00171	0.57±0.00171	0.57±0.00171
3 cm	0.58±0.00172	0.58±0.00172	0.58±0.00173	0.58±0.00172	0.58±0.00173
4 cm	0.59±0.00173	0.59±0.00174	0.59±0.00174	0.59±0.00174	0.59±0.00174
5 cm	0.59±0.00176	0.59±0.00175	0.6±0.00177	0.59±0.00176	0.6±0.00177
6 cm	0.59±0.00297	0.58±0.00294	0.59±0.00296	0.59±0.00298	0.59±0.00296

Table 5.12: Neutron flux at HEU core outer irradiation sites at 30 KW

	Neutron flux in $10^{11}\mathrm{ncm}^{-2}\mathrm{s}^{-1}$				
	Thermal flux				
	1	2	3	4	5
1 cm	6.34±0.0096	6.28±0.0096	6.59±0.0145	6.62±0.0145	6.61±0.0145
2 cm	6.4±0.0097	6.35±0.0097	6.69±0.0146	6.71±0.0147	6.69±0.0147
3 cm	6.47±0.0097	6.4±0.0097	6.72±0.0147	6.79±0.0148	6.77±0.0148
4 cm	6.5±0.0098	6.41±0.0097	6.78±0.0148	6.79±0.0148	6.81±0.0149
5 cm	6.52±0.0099	6.4±0.0099	6.78±0.015	6.84±0.0151	6.8±0.015
6 cm	6.49±0.0163	6.37±0.0162	6.81±0.025	6.8±0.0249	6.76±0.0248
	Epithermal flux				
	1	2	3	4	5
1 cm	1.31±0.0056	1.31±0.0055	1.37±0.0083	1.38±0.0084	1.37±0.0084
2 cm	1.36±0.0057	1.36±0.0057	1.43±0.0085	1.44±0.0086	1.44±0.0085
3 cm	1.39±0.0057	1.4±0.0058	1.47±0.0086	1.47±0.0086	1.47±0.0086
4 cm	1.42±0.0058	1.44±0.0058	1.5±0.0087	1.53±0.0088	1.5±0.0087
5 cm	1.43±0.0059	1.44±0.0059	1.52±0.0089	1.53±0.0089	1.51±0.0089
6 cm	1.42±0.0098	1.42±0.0098	1.5±0.0147	1.51±0.0148	1.5±0.0148
	Fast flux				
	1	2	3	4	5
1 cm	0.64±0.0039	0.65±0.004	0.67±0.0058	0.67±0.0058	0.66±0.0058
2 cm	0.67±0.004	0.67±0.004	0.69±0.0059	0.7±0.0059	0.69±0.0059
3 cm	0.68±0.0041	0.69±0.0041	0.71±0.006	0.72±0.006	0.7±0.006
4 cm	0.7±0.0041	0.7±0.0041	0.73±0.0061	0.73±0.0061	0.72±0.006
5 cm	0.7±0.0042	0.71±0.0042	0.73±0.0061	0.74±0.0062	0.72±0.0061
6 cm	0.68±0.0033	0.7±0.0033	0.72±0.0046	0.72±0.0046	0.7±0.0046

REFERENCES

Abrefah, R. G., Anim-Sampong, S., Nyarko, B. J. B., Akaho, E. H. K., & Sogbadji, R. B. M. (2011). Measure ment of neutron flux distribution in the irradiation channel in the Ghana Research Reactor-1 using monte carlo method. *Progress in Nuclear Energy*, *53*, 189–194.

Adelfang, P. & Atger, A. (Eds.). (2006). Fuel Cycle and Waste Newsletter. *Conversion of Reasearch Reactors from HEU to LEU fuel*, *2.1*. Retrieved from http://www.iaea.org/OurWork/ST/NE/NEFW/index.html

Ahmed, Y., Umar, I., Ewa, I., Ajuji, A., Nyarko, B., & Akaho, E. (2006). *AN ALTERNATIVE APPROACH TO THE DETERMINATION OF EPITHERMAL FLUX−SHAPING FACTOR (α) FOR K_0 −NAA*. United Nations Educational Scientific, Cultural Organization, and International Atomic Energy Agency, THE ABDUS SALAM INTERNATIONAL CENTRE FOR THEORETICAL PHYSICS.

Akaho, E. H. K. & Nyarko, B. J. B. (2002). Characterization of neutron flux spectra in irradiation sites of MNSR reactor using Wescott-formalism for k_0 neutron activaton analysis method. *Applied Radiation and Isotopes*, *57*, 265–273.

Aldawanra, S., Khattab, K., & Saba, G. (2015). Neutronic analysis for core conversion (HEU-LEU) of the low power research reactor using MCNP4C code. *NUKLEONIKA*, *60*(2), 367–371.

Anim-Sampong, S., Maakuu, B. T., & Akaho, E. (2007). *MONTE CARLO NEUTRON TRANSPORT SIMULATION OF THE GHANA RESEARCH REACTOR-1*. Department of Nuclear Engineering and Materials Science National Nuclear Research Institute Ghana Atomic Energy Commission.

Anim-Sampong, S., Maakuu, B. T., Akaho, E., Andam, A., Liaw, J. J. R., & Matos, J. E. (n.d.). *Progress in the neuronic core conversion (HEU-LEU) analysis of Ghana research reactor-1*.

Baidoo, I. K., Nyarko, B. J. B., Akaho, E. H. K., Dampare, S. B., Sogbadji, R. B. M., & Poku, L. O. (2013). Characterization of low power research reactor neutrons for the validaton of k_0-naa standardization based on k_0-iaea software. *Applied Radiation and Isotopes*, *79*, 85–93.

Booth, T. E., Hughes, H. G., Zukaitis, A., Brown, F. B., Mosteller, R. D., Boggs, M., … Sweezy, J. E. (2003, April). *MCNP: A General Monte Carlo N Particle Transport Code, Version 5*.

Brewer, R. (2009, January). *Criticality Calculations with MCNP5: A Primer*.

Corte, F. D. [F. De], Hammami, K. S.-E., Moens, L., Simonits, A., Wispelaere, A. D., & Hoste, J. (1981). THE ACCURACY AND PRECISION OF THE EXPERIMENTAL $\alpha-$DETERMINATION IN THE $1/E^{\alpha+1}$ EPITHERMAL REACTOR-NEUTRON SPECTRUM. *Journal of Radioanalytical Chemistry*, *62*, 209–255.

Corte, F. D. [Frans De]. (1987). *The k_0-standardization method, A move to the optimization of neutron activation analysis* (Doctoral dissertation, University of Gent, Belgium).

Dien, N. N., Vien, L. B., Vinh, L. V., Dong, D. V., Hai, N. X., Son, P. N., & Vu, C. D. (2014). Resilts of Operation and Utilization of the Dalat Nuclear Research Reactor. *Nuclear Science and Technology*, *4*, 01–09.

Dung, H. M., Freitas, M. C., Santos, J. P., & Marques, J. G. (2010). Re-characterization of Irradiation Facilities for K_0-NAA at RPI after Conversion to LEU and Re-arrangement of Core Configuration. *Nuclear Instruments and Methods in Physics Research*, *A 622*, 438–442.

Gbadago, J., Addo, M., Ennison, I., Odoi, H. C., Boffie, J., Boafo, E., … Debrah, S. (2011). *Ghana Research Reactor−1Safety Analysis Report, Revised Version*. Ghana Atomic Energy Commission Technical Report, GAEC-NNRI-RT.

Glascock, M. D. (2015). Overview of Neutron Activation Analysis. Retrieved from http://archaeometry.missouri.edu/naa_overview.html

Hamidatou, L., Slamene, H., Akhal, T., & Zouranen, B. (2013). Concepts, Instrumentation and Techniques of Neutron Activation Analysis. In *Imaging and Radioanalytical Techniques in Interdisciplinary Research – Fundamentals and Cutting Edge Applications* (Chap. 6). InTech, Chapters published. doi:10.5772/3426

Hung, T. V. & Cuong, N. K. (2016). Neutron Flux Characteristics in the Irradiation Channels of Dalat Reactor after Converting from HEU to LEU Fuels. *Journal of nuclear Energy Science and Power Generation technology*.

Jonah, S. A., Ibrahim, Y. V., Ajuji, A. S., & Onimisi, M. Y. (2012). The impact of HEU to LEU conversion of commercial MNSR: Determination of neutron spectrum parameters in irradiation channels of NIRR−1 using MCNP code. *Annals of Nuclear Energy*, *39*(1), 15–17.

Jovanovic, S., Vukotic, P., Smodis, B., Jacimovic, R., Mihaljevic, N., & Stegnar, P. (1988). Epithermal neutron flux characterization of the TRIGA MARK II reactor, Ljubljana, Yugoslavia, for use in NAA. *Journal of Radioanalytical and Nuclear Chemistry*, *129*, 343–349.

Moteff, J., Wright, S., Droulers, Y., Zijp, W., Dahl, R., Yoshikawa, H. H., & Keddar, A. (1970). *Neutron Fluence Measurements*. International Atomic Energy Agency.

Odoi, H. C., Akaho, E. H. K., Nyarko, B. J. B., Abrefah, R. G., Ampomah-Amoako, E., Sogbadji, R. B. M., . . . Kalimullah, M. (2012, October). Conversion of International MNSR – Reference Case of Ghana MNSR. RERTR 2012 - 34th INTERNATIONAL MEETING ON REDUCED ENRICHMENT FOR RESEARCH AND TEST REACTORS. Warsaw, Poland.

Argonne, China sign agreement to develop Zero Power Test Facility. (2010, October). Retrieved from http://www.ne.anl.gov/About/headlines/20101027.shtml

CRP on conversion of Miniature Neutron Source Research Reactors (MNSR) to Low Enriched Uranium (LEU). (2014, June). Retrieved from https://www.iaea.org/OurWork/ST/NE/NEFW/Technical-Areas/RRS/mnsr.html

Report on Zero Power Test. (2016). China Institute of Atomic Energy.

Phillips, J. M., Adelfang, P., Gabrielse, G., Glaser, A., Johnson, D. W., Lemoine, P., … Yudintsev, S. V. (Eds.). (2016). *Reducing the Use of Highly Enriched Uranium in Civilian Research Reactors*. The National Academy Press. doi:10.17226/21818

Schwerer, O. (2001). Nuclear Data Services Provided by IAEA. International Atomic Energy Agency.

Snoj, L. & Trkov, A. (2015). Introduction to computer codes MCNP. Jozef Stefan Institute. Ljubljana Slovenia.

Sogbadji, R. B. M., Nyarko, B. J. B., & Akaho, E. H. K. (2011). Determination of Neutron Fluxes and Spectrum Shaping factor in Irradiation Sites of Ghana's Miniature Neutron Source Reactor (mnsr) by Activation Metho after Compensation of Loss of Excess Reactivity. *World Journal of Nuclear Science and Technology*, *1*, 50–56.

Vu, C. D., Thein, T. Q., Doanh, H. V., Quyet, P. D., Anh, T. T. T., & Dien, N. N. (2014). Characterization of Neutron Spectrum Parameters at Irradiation Channels for Neutron Activation Analysis after Full Conversion of the Dalat Nuclear Research Reactor to Low Enriched Uranium Fuel. *Nuclear Science and Technology*, *4*, 70–75.